

DESIGN OPTIMIZATION OF THIN CRYSTALLINE-SILICON SOLAR CELLS

By

DABRAJ SARKAR

A DISSERTATION PRESENTED TO THE GRADUATE SCHOOL
OF THE UNIVERSITY OF FLORIDA IN PARTIAL FULFILLMENT
OF THE REQUIREMENTS FOR THE DEGREE OF
DOCTOR OF PHILOSOPHY

UNIVERSITY OF FLORIDA

2012

© 2012 Dabraj Sarkar

To my parents

ACKNOWLEDGMENTS

I thank my advisor, Professor Jerry G. Fossum, for his guidance and my committee members, Professors Mark E. Law, Gijs Bosman, Timothy J. Anderson, and Leo Mathew, for helping me complete this work.

I thank Professor Sanjay K. Banerjee at the University of Texas at Austin for his advising and allowing me to use the device fabrication facility at the Microelectronics Research Center. I also thank Dr. Rajesh Rao and Dr. Dharmesh Jawarani of AstroWatt Inc. for experimental setup and guidance. I thank AstroWatt Inc., and DOE for funding me and this work, and I thank my colleagues in lab for discussion and friendship: Emmanuel Onyegam, Nicole Rowsey, Dan Cummings, Sayan Saha, Dewei Xu, Scott Smith, Siddharth Chowksey, Shishir Agrawal, Zhenming Zhou, Zhichao Lu, Hema Chandra Prakash, Mike Ramon, Ricardo Garcia, Moses Ainom, Ariam Gurmu and Rachel Stout.

I would like to thank Shannon Chillingworth, Edwina McKay, Stephenie Sparkman, March Lee, Cheryl Rhoden, Marcus Moore, and Teresa Stevens of Electrical and Computer Engineering department for their support during my graduate study at the University of Florida.

Finally, I would like to thank my parents (Jyotish Chandra Sarkar, Shova Sarkar, and Sheela Sarkar), and siblings (Durga, Sujoy, and Chinmoy) for their continuous support, inspiration and sacrifice.

TABLE OF CONTENTS

	<u>page</u>
ACKNOWLEDGMENTS.....	4
LIST OF TABLES.....	7
LIST OF FIGURES.....	8
ABSTRACT	10
CHAPTER	
1 INTRODUCTION	12
2 PHYSICS-BASED FLOODS SETUP FOR SOLAR CELL SIMULATION.....	17
2.1 Solar Cell Device Physics and Model Development.....	18
2.2 Model Application and Verification	23
2.3 Summary.....	26
3 LOCAL BSF INSIGHTS FOR THIN SOM SOLAR CELLS.....	31
3.1 Back-Surface Field and Simulation Setup in FLOODS	32
3.2 Thin Cells with Uniform BSF Diffusions.....	33
3.3 Local BSF: Physical Insights and Design.....	36
3.4 Performance Dependence on Thickness Variation	37
3.5 Summary.....	38
4 BACK-CONTACT SOLAR CELLS IN THIN CRYSTALLINE SILICON.....	51
4.1 Novel Thin-Silicon BC Solar Cell Process	51
4.2 2-Dimensional Numerical Simulations.....	53
4.3 BC Cell Design and Performance Projections.....	54
4.4 Further Consideration of V_{OC}	61
4.5 Summary.....	63
5 HETEROJUNCTION SOM SOLAR CELLS	73
5.1 Background.....	75
5.2 Exfoliation Process.....	79
5.3 Indium Tin Oxide Process Development	80
5.4 Overview of Remote-Plasma Chemical Vapor Deposition System	83
5.5 RPCVD Process Development and Cell Fabrication	84
5.6 RPCVD Process Optimization.....	86
5.7 Single-Side Heterojunction Cell.....	87
5.8 Double-Side Heterojunction Cell	90

5.9	Summary.....	92
6	SUMMARY AND FUTURE WORK	113
6.1	Summary.....	113
6.2	Future Work	114
6.2.1	Carrier Transport Model across HJ	115
6.2.2	Surface Recombination Velocity Characterization	115
6.2.3	Light Trapping by Surface Texturing	116
	LIST OF REFERENCES	117
	BIOGRAPHICAL SKETCH.....	122

LIST OF TABLES

<u>Table</u>	<u>page</u>
2-1	FLOODS-predicted performance of thick p ⁺ n cell versus base doping density. . 27
2-2	FLOODS-predicted performance of the p ⁺ nn ⁺ cell versus minority-hole lifetime. 27
3-1	FLOODS-predicted performance versus back metal contact width for p ⁺ nn ⁺ uniform BSF cell (Structure-A)..... 40
3-2	FLOODS-predicted performances of three thin BSF cell design architectures... 40
3-3	FLOODS-predicted performance versus back contact pitch for local BSF cell (Structure-C)..... 41
4-1	FLOODS-predicted BC cell performance in AM1 (92.5mW/cm ²) sunlight versus front-surface recombination velocity..... 65
4-2	FLOODS-predicted performance of the S _f =10cm/s BC cell in Table 4-1 versus fractional metal-contact coverage on the back n ⁺ /p ⁺ regions. 65
4-3	FLOODS-predicted performances of the near-optimal 25μm BC-cell design, with w (w _n =w _p =300μm) widened to trade-off BCSOM-process simplicity versus lifetime..... 66
4-4	FLOODS-predicted performance of the w=150μm BCSOM cell in Table 4-3 with reduced N _S =10 ¹⁹ cm ⁻³ versus the metal-contact width 66
5-1	Overview of HJ device structures and corresponding performances..... 94
5-2	Measured Suns-Voc from cells fabricated on 500μm c-Si wafers for varying sample positions and temperatures..... 94

LIST OF FIGURES

<u>Figure</u>	<u>page</u>
2-1	Effective and actual doping density profiles implemented in FLOODS for minority-carrier transport 28
2-2	Schematic cross-sections of conventional p ⁺ n and p ⁺ nn ⁺ solar cells 29
2-3	FLOODS-predicted illuminated JV and PV characteristics of thick p ⁺ n cell 30
3-1	Cross-section of pn-junction solar cell with uniform BSF. 42
3-2	FLOODS-predicted V _{OC} , and J _{SC} performance as a function of back contact pitch width for uniform BSF cell (Structure-A)..... 43
3-3	FLOODS-predicted FF, and efficiency performance as a function of back contact pitch width for uniform BSF cell (Structure-A) 44
3-4	Cross-sections of three thin BSF solar cell architectures. 45
3-5	FLOODS-predicted V _{OC} and J _{SC} performance versus S _b with back contact pitch as a parameter for local BSF cell (Structure-C) 46
3-6	FLOODS-predicted V _{OC} and J _{SC} performance versus back contact pitch with S _b as a parameter for local BSF cell (Structure-C) 47
3-7	FLOODS-predicted FF and efficiency versus back contact pitch with S _b as a parameter for local BSF cell (Structure-C)..... 48
3-8	FLOODS-predicted comparative performance analysis versus hole lifetime with device thickness as a parameter for local BSF cell (Structure-C) 49
3-9	FLOODS-predicted local BSF cell (Structure-C) efficiency versus hole lifetime for different cell thicknesses. 50
4-1	A fabricated thin (t _{Si} ~ 25μm) crystalline-silicon BCSOM solar cell..... 67
4-2	Demonstration of the flexibility of the SOM foil, which can broaden its possible applications. 68
4-3	A measured 1-sun current-voltage characteristic of the BCSOM solar cell 69
4-4	Basic cross-section of the BC solar cell structure, or the FLOODS domain assumed for the 2-D numerical simulations..... 70
4-5	FLOODS-predicted open-circuit voltage versus the back nonmetal-surface recombination velocity for varying n ⁺ /p ⁺ surface doping density. 71

4-6	FLOODS-predicted loss of short-circuit current density versus increasing p ⁺ -region width, for different w _n /w _p ratios.....	72
5-1	Cross-section of a typical double-side heterojunction cell on a n-type crystalline-silicon SOM wafer.....	95
5-2	Process flow for fabricating exfoliated single heterojunction solar cells.....	96
5-3	SIMS profile showing Hydrogen incorporation into the Si substrate during the electroplating process.....	97
5-4	Photographs of exfoliated SOM foils.	98
5-5	Variation of sheet resistance of ITO films as function of substrate temperature	99
5-6	Variation of optical transmittance characteristics of ITO films as function of substrate temperature	100
5-7	Variation of sheet resistance of ITO films as a function of deposition pressure	101
5-8	Optical transmittance spectra of ITO films as a function of Ar pressure.	102
5-9	Schematic diagram of RPCVD deposition chamber	103
5-10	Photograph of SOM foil with fabricated HJ cells, and cross-section of fabricated single-side HJ cells.	104
5-11	Raman spectra of a-Si:H(p ⁺) films deposited at different temperatures.....	105
5-12	High resolution TEM cross-section of thin HJ solar cell on SOM foil.	106
5-13	Illuminated JV and EQE characteristics of single-side HJ solar cells	107
5-14	Cross-section of the proposed single-side heterojunction (SHJ) cell on a n-type SOM wafer.....	108
5-15	EQE data indicating carrier recombination at the back due to uniform metal contacts and no surface passivation.....	109
5-16	FLOODS-predicted dependence of intrinsic V _{OC} , J _{SC} , and η versus silicon thickness for varying bulk lifetime.	110
5-17	Illuminated JV and EQE characteristics of double-side HJ solar cells	111
5-18	Comparison of dark saturation current densities vs. open circuit voltages for different cell structures.	112

Abstract of Dissertation Presented to the Graduate School
of the University of Florida in Partial Fulfillment of the
Requirements for the Degree of Doctor of Philosophy

DESIGN OPTIMIZATION OF THIN CRYSTALLINE-SILICON SOLAR CELLS

By

Dabraj Sarkar

August 2012

Chair: Jerry G. Fossum

Major: Electrical and Computer Engineering

Solar cells in thin crystalline-silicon are of much interest because of their potential high efficiencies and low cost. However, many previous attempts to attain thin silicon for photovoltaic applications have involved costly processes, such as high-energy implants and epitaxial growths, and impractical ways of handling the thin films. Hence, development of cost-effective crystalline-silicon solar cells with optimal thickness of 10-100 μm has remained an unfulfilled goal for many years. In this work, we report a novel kerfless exfoliation technology capable of producing ultra-thin 25 μm flexible monocrystalline silicon foils from thick Si wafers.

We set up an object-oriented 2-D device simulator (FLOODS), and augmented it for reliable physics-based numerical simulation of thin-Si solar cells. This tool provides flexibility for general simulations that commercial tools do not. The setup includes (i) characterization of the electron-hole generation rate, (ii) internal photon reflection, (iii) modeling of SRH and Auger carrier recombination rates, (iv) modeling of carrier mobilities, and (v) physical accounting for energy-bandgap narrowing and Fermi-Dirac statistics in heavily doped regions.

Using FLOODS simulations, we present physical insights into the various recombination mechanisms and how they affect performances of thin BSF cells. We have explored novel design techniques and engineering tradeoffs such as base doping density, local BSF, local back contacts, and contact width and pitch to reduce the recombination losses.

As the crystalline-silicon thickness is reduced to attain substantial cost reduction, excellent surface passivation on both sides is required to fabricate higher-efficiency solar cells. We fabricated back-contact solar cells and a-Si:H/c-Si heterojunction solar cells to achieve this goal. Numerical simulations with FLOODS were used to identify losses in these devices, and optimum device structures were designed, and performance predicted with numerical simulations.

A novel remote-plasma CVD (RPCVD)-based process was developed for fabrication of a-Si:H/c-Si heterojunction(HJ) photovoltaic cells. In the RPCVD system, during the deposition process there is no direct exposure of the sample to the plasma. This can reduce the plasma damage to the silicon surface and improve passivation quality. Very high open-circuit voltage measured from fabricated heterojunction cells suggests that RPCVD is a potential technology for achieving improved passivation in HJ cells.

CHAPTER 1 INTRODUCTION

Crystalline-silicon solar cells are of much interest because of their potential high efficiencies and low cost [1]. In order to reduce cost/watt of crystalline-silicon solar cells and to achieve grid electricity cost parity, it is necessary to achieve high conversion efficiency with thinner crystalline silicon wafers because the silicon accounts for a large part of the module cost [2]. However, cell manufacturers are struggling to reduce the wafer thickness below 100 μm as there are no economically viable technologies for manufacturing very thin Si wafers, and such thin Si wafers impose stringent handling requirements such as wafer breakage and yield loss that impact final module cost. Hence, development of cost-effective crystalline-silicon solar cells with optimal thickness of 10-100 μm has remained an unfulfilled goal for many years [1]. The research described herein seeks to explore modeling, simulation, and design of thin (25 μm) crystalline-Si solar cells along with experimental corroboration based on a kerf-free semiconductor-on-metal (SOM) exfoliation process [3].

Historically, manufacturers have focused their research more on other cost elements than efficiency, and efficiency improvements in commercial cells were largely stagnated until 2002 [2]. However, there is a recent resurgence in interest in improved efficiency, particularly for thinner cells. The theoretical maximum possible efficiency of a single junction silicon solar cell is about 29% [4], [5]. Actual cell efficiencies fall quite short of this ideal limit due to various extrinsic losses, e.g., reflection losses at front grid and front surface, optical absorption losses in back contact, carrier recombination losses in the bulk Si, at front/back surfaces and at front/back contacts, and resistive losses in diffusion regions, at contacts and metal grids [2]. Identification and reduction of

these losses have become very significant factors for the design and manufacturing of thinner high-efficiency solar cells. Sanyo's HIT [6] and SunPower's "generation-3" [7] laboratory solar cells have eliminated much of these extrinsic losses, and have yielded efficiencies of 23.0% and 24.2%, respectively.

As the efficiency of solar cells has become premium, numerical solutions of the carrier transport problem in the solar cells are desirable to find and analyze where and how improvements in the cell design can be achieved. Crystalline-silicon solar cells can be simulated reliably because of the vast knowledge of the silicon properties that has evolved for more than 50 years of integrated-circuit developments. These properties must be physically accounted for. For thin cells, the features of heavily doped silicon (i.e. bandgap narrowing, carrier degeneracy, or Fermi-Dirac (F-D) statistics, and Auger recombination) are most important since much of the thin cell is heavily doped. In Chapter 2, we discuss how we augment and set-up FLorida Object Oriented Device Simulator (FLOODS) [8], a TCAD tool under development at the University of Florida, for reliable physics-based numerical simulation of thin crystalline-silicon solar cells in AM1 sunlight. The reliability of the simulation tool and analyses is corroborated by comparing results for conventional cells with published results in the literature.

We note in Chapter 2, that the high recombination velocities near surfaces can limit the cell efficiency. Moreover, the unavoidable Auger recombination in the back surface-field (BSF) region limits the cell efficiency. Rear surface recombination can be reduced by reducing the back metal contact area and passivating most of the back surface with thermal oxides, and Auger recombination in the BSF region can be reduced by introducing local BSF doping and point contacts [9]. Local back doping was

employed in 280 μm -thick PERL cells [10], but there is currently little insight available in the literature on how local contact/doping works for thin cells with thickness of about 25 μm . In Chapter 3, we present new physical insights, derived from FLOODS simulations, into the benefits of local-doping/point-contact and thus reduce the effect of back surface recombination on BSF cell performance.

The back-contact (BC) solar cell has the highest possibility of increased performance close to the intrinsic performance of 29% efficiency in the near future [4]. Originally intended for concentrator systems [11], BC cells have attracted broad interests due to its several advantages over conventional cells. Front grid-reflection and -shadowing losses, and front grid-resistance losses can be eliminated in BC solar cells [4]. The back junction can be optimized for electrical performance (e.g., dark saturation current density) and the top surface can be optimized for optical performance [12]. Since metal contacts are on the back side, the trade-off between grid shading and series resistance is no longer present in BC cells [12]. Clearly, BC cells require starting material with a long minority-carrier lifetime. However, since the exfoliated SOM foils are of thickness 20-30 μm , the BCSOM cell is a potentially suitable technology for achieving high efficiency solar cells.

In Chapter 4, fabrication of preliminary BCSOM solar cells is described along with experimental data, and ultimate efficiency of BCSOM cell is projected. We identify the important device parameters for efficient cell design: the front-surface recombination velocity, the back nonmetal-surface recombination velocity, back-surface doping density, the widths of interdigitated n^+ and p^+ regions, and the widths of the respective metal-contact lines. We gain physical insights into the front surface-passivation

requirements, and tradeoff between the widths of interdigitated n^+ and p^+ regions and optimum back-contact geometry for 25 μm -thick BCSOM cells. Key recombination mechanisms in back diffusion regions limiting the ultimate BCSOM cell performance are identified and insights on optimum doping profile are revealed. The projected performance of the ultimate BCSOM is compared to that of SunPower Corporation's "generation-3" BC solar cells [7].

To reduce the noted surface recombination and to achieve better minority-carrier suppression near the surface, an a-Si:H/c-Si heterojunction (HJ) with a bandgap larger than Si is put between the metal and silicon [4], using a transparent front electrode to keep the series resistance low. The a-Si:H/c-Si heterojunction with a thin intrinsic a-Si:H buffer layer was first reported in 1977, and later developed and commercialized by Sanyo Electric Co. as HIT solar cells [13]. The effective passivation and the reduced minority-carrier concentration achieved by the a-Si:H/c-Si heterojunction enables high open-circuit voltage V_{OC} , and high efficiency. In addition, the a-Si:H/c-Si heterojunction is a low temperature process (usually $<200^\circ\text{C}$), and it reduces crystal damage and production costs [14]. Thus, thin HJ is an obvious choice with SOM wafers to manufacture low-cost solar cells.

Fabrication of single-side heterojunction (SHJ) and double-side heterojunction (DHJ) cells on SOM wafers is described in Chapter 5. Insights about HJ cell losses and design for performance improvements are presented by analyzing current-voltage (IV), quantum efficiency (QE), and Suns-Voc characteristics. In HJ solar cells, a transparent conducting oxide (TCO) layer, such as indium tin oxide (ITO), is used to reduce the lateral resistance associated with thin a-Si:H emitters. An R.F. magnetron reactive

sputtering system was used to develop an optimized process for the ITO films. A remote-plasma chemical vapor deposition (RPCVD)-based process was developed to fabricate a-Si:H/c-Si heterojunction cell. In the RPCVD system, the sample is held distant from the plasma source and the deposition chamber is in ultra-high vacuum (UHV) – both can lead to reduced surface damage to the c-Si surface. Sample-to-plasma distance, deposition temperature, and thickness of a-Si layers were characterized in order to achieve improved surface passivation. A 13.4% efficiency cell was fabricated, and V_{OC} as high as 662mV was obtained. Comprehensive study of the carrier-transport mechanisms across the junction hetero-interface is necessary for efficient heterojunction (HJ) cell design. FLOODS, upgraded by reliable engineering-based models for the carrier-transport mechanism and optical absorption across the heterojunction, can aid such a study. The local-doping and point-contact BSF scheme in the single-side HJ SOM cell, with optimal design derived from FLOODS simulations, should be incorporated.

CHAPTER 2 PHYSICS-BASED FLOODS SETUP FOR SOLAR CELL SIMULATION

Solar cells are bipolar devices with high doping levels in the emitter and BSF regions to achieve better device performance. Reliable modeling of heavy-doping (HD) effects is important to predict solar cell performance. In this chapter, FLOODS [8], an object-oriented 2-D device simulator, is augmented and set-up for reliable physics-based numerical simulation of thin crystalline-silicon solar cells in AM1 sunlight, with emphasis on the modeling of HD effects. Reliable modeling and simulation tools for solar cell design are warranted as the conversion efficiency of solar cell is at a premium today. This was neglected in the past largely due to shift in research trends to process and technology. FLOODS for solar cells provides flexibility for general simulations that commercial tools do not.

Models we have implemented in FLOODS are: (i) characterization of the electron-hole generation rate [$g(x)$ in 1-D] defined by AM1 photon absorption, with or without internal photon reflection, (ii) physical accounting for energy-bandgap narrowing and Fermi-Dirac (F-D) statistics in heavily doped regions, (iii) modeling of SRH and band-band Auger carrier recombination rates, and (iv) modeling of carrier mobilities dependent on doping densities. One- and two-dimensional simulations can be done in FLOODS.

The chapter begins with modeling and implementation of the above mentioned device physics in FLOODS. Later, the reliability of implemented models and FLOODS simulations were verified by deriving physical insights into the back-surface field (BSF). BSF consists of a high-low (HL) junction at the back of the device and it is an important design technique to reduce recombination at the back of the solar cell, and improve

device performance. BSF becomes very effective if the base of the solar cell is transparent to the minority-carrier flow (i.e. minority-carrier diffusion length longer than cell thickness). The built-in electric field induced by the HL junction opposes the motion of minority carriers to the back surface where the recombination velocity is very high. Moreover, the increase in integrated doping density in the base reduces minority-carrier injection into the base. Thus BSF improves both the short-circuit current density (J_{SC}) and open-circuit voltage (V_{OC}).

2.1 Solar Cell Device Physics and Model Development

For thinner cells, the features of heavily doped silicon [i.e., bandgap narrowing (ΔE_g), carrier degeneracy, or F-D statistics, and Auger recombination] are most important since much of the silicon solar structure must be heavily doped. In FLOODS, we physically account for ΔE_g and F-D statistics by using an effective doping density (e.g., $N_{D(\text{eff})}$ for n^+ Si) to model the minority-carrier (hole) transport [16]:

$$N_{D(\text{eff})} = N_D \left(\frac{n_i^2}{n_{ie}^2} \right) \quad (2-1)$$

where N_D is the actual doping density and n_{ie} is an effective intrinsic carrier density that depends on ΔE_g and the F-D integral of order 1/2:

$$n_{ie}^2 = n_i^2 \exp\left(\frac{\Delta E_g}{k_B T}\right) \left[\frac{F_{1/2}(\eta_c)}{\exp(\eta_c)} \right] \quad (2-2)$$

with $\eta_c \equiv (E_F - E_C)/k_B T$ being the relative position of the Fermi level. Both the ΔE_g and the $F_{1/2}$ terms in Eq. 2-2 depend on the majority-electron density, or N_D . We note that the former term increases with N_D , while the latter term decreases, implying that $N_{D(\text{eff})}$

in (2-1), which is generally less than N_D , does not vary with the doping density in a simple way [16]. Further, we note that the modeling of $N_{D(\text{eff})}$ vs. N_D (~linear for typical high N_D [17]) differs from that of $N_{A(\text{eff})}$ vs. N_A for p^+ Si (~constant for typical high N_A [16]). Fig. 2-1 shows effective donor and acceptor doping densities for an analytical Gaussian doping profile ($N_D = N_{SD} \exp(-\frac{x^2}{2\sigma^2})$). We note that $N_{D(\text{eff})}$ is itself a Gaussian profile with modified surface doping concentration ($N_{SD(\text{eff})} < N_{SD}$) and standard deviation (straggle σ_{eff}), i.e., $N_{D(\text{eff})} = N_{SD(\text{eff})} \exp(-\frac{x^2}{2\sigma_{\text{eff}}^2})$.

To physically account for heavy-doping effects and predict minority-carrier transport, we use the effective net doping density ($N_{D(\text{eff})} - N_{A(\text{eff})}$) in Poisson equation,

$$\frac{\partial^2 \psi}{\partial x^2} + \frac{\partial^2 \psi}{\partial y^2} = -\frac{q}{\epsilon_{\text{si}}} [N_{D(\text{eff})} - N_{A(\text{eff})} + p - n] \quad (2-3)$$

which is solved in FLOODS with the carrier continuity equation. However, SRH and Auger band-band carrier recombination rates are dependent on the actual doping densities (e.g., $N_D(x)$, $N_A(x)$). SRH carrier recombination is given by [18]

$$U_{\text{SRH}} \cong \frac{(np - n_i^2)}{\tau_{p(\text{SRH})}(n + n_i) + \tau_{n(\text{SRH})}(p + n_i)} \quad (2-4)$$

where $\tau_{p(\text{SRH})}$, $\tau_{n(\text{SRH})}$ are doping-dependent lifetime parameters [19]:

$$\tau_{p(\text{SRH})} = \frac{\tau_{p0}}{1 + \frac{N_A(x) + N_D(x)}{N_{\text{REF}}}} \quad (2-5)$$

$$\tau_{n(\text{SRH})} = \frac{\tau_{n0}}{1 + \frac{N_A(x) + N_D(x)}{N_{\text{REF}}}} \quad (2-6)$$

with $N_{\text{REF}} = 7.1 \times 10^{15} \text{ cm}^{-3}$, and τ_{n0} and τ_{p0} chosen based on the material quality. Auger band-band carrier lifetime fundamentally varies with the square of the majority-carrier density or doping density. Auger band-band recombination is modeled in terms of actual carrier density as

$$U_{\text{BBA}} = C_n n(np - n_i^2) + C_p p(np - n_i^2) \quad (2-7)$$

$$\approx C_n N_D (N_D p - n_i^2) + C_p N_A (n N_A - n_i^2) \quad (2-8)$$

$$\approx C_n N_D^2 \left(p - \frac{n_i^2}{N_D} \right) + C_p N_A^2 \left(n - \frac{n_i^2}{N_A} \right) \quad (2-9)$$

$$\approx \frac{\Delta p}{\tau_{\text{Ap}}} + \frac{\Delta n}{\tau_{\text{An}}} \quad (2-10)$$

where $C_n \approx 2.2 \times 10^{-31} \text{ cm}^6/\text{s}$ and $C_p \approx 1.0 \times 10^{-31} \text{ cm}^6/\text{s}$, and Auger hole, electron lifetimes

are $\tau_{\text{Ap}} \equiv \frac{1}{C_n N_D^2}$, $\tau_{\text{An}} \equiv \frac{1}{C_p N_A^2}$ respectively [18], [20]. Effective hole and electron

lifetimes (τ_p, τ_n) are given by

$$\frac{1}{\tau_p} = \frac{1}{\tau_{p(\text{SRH})}} + \frac{1}{\tau_{\text{Ap}}} \quad (2-11)$$

$$\frac{1}{\tau_n} = \frac{1}{\tau_{n(\text{SRH})}} + \frac{1}{\tau_{\text{An}}} \quad (2-12)$$

Electron and hole mobilities are also based on actual doping densities [21] – [22], and modeled as

$$\mu = \mu_{(\text{min})} + \frac{\mu_{(\text{max})} - \mu_{(\text{min})}}{1 + \frac{N_A(x) + N_D(x)}{N_{\mu(\text{REF})}}} \quad (2-13)$$

where $\mu_{(\min)}=68.5\text{cm}^2/\text{V.s}$, $\mu_{(\max)}=1414\text{cm}^2/\text{V.s}$ for electron, and $\mu_{(\min)}=44.9\text{cm}^2/\text{V.s}$, $\mu_{(\max)}=470\text{cm}^2/\text{V.s}$ for hole.

For FLOODS simulations, physical characterizations of surfaces are done via surface recombination velocities (SRV). For 1-D simulations, a quasi-ohmic boundary condition is defined to enable specification of recombination velocities at the surfaces through which current must flow by

$$J_p = q \cdot \Delta p \cdot S \quad (2-14)$$

where S is the surface recombination velocity (SRV). The charge neutrality at the surface

$$N_{D(\text{eff})} - N_{A(\text{eff})} + p - n = 0 \quad (2-15)$$

completes the set of surface boundary conditions. For 2-D simulations, at surfaces through which no current can flow (e.g., oxide or nitride passivated surfaces), the surface recombination velocity (SRV) is specified by

$$U_{S(\text{SRH})} \equiv \frac{np - n_i^2}{\frac{1}{S_n}(p + n_i) + \frac{1}{S_p}(n + n_i)} \quad (2-16)$$

where S_n and S_p are the electron and hole SRVs respectively. For $S_n=S_p=S$

$$U_{S(\text{SRH})} \equiv S \frac{np - n_i^2}{(p + n_i) + (n + n_i)} \quad (2-17)$$

Electron-hole generation rate $g(x)$ induced by photon is defined in FLOODS based on an AM1 photon spectrum with an incident power level of $92.5\text{mW}/\text{cm}^2$ [23]. However, the current standard testing condition for terrestrial measurements is AM1.5 (global) which was adopted in 2008 as IEC 60904-3 Ed. 2 (also equivalent to ASTM G173) with an input power level of $100\text{mW}/\text{cm}^2$ [24]. Thus, AM1 performance of solar cell predicted

by FLOODS can easily be normalized to global AM1.5 standard testing conditions by multiplying J_{SC} by 1.08, and increasing V_{OC} by 2mV with FF unaltered.

Under normal solar illumination, the photon flux falls off exponentially into the semiconductor, i.e.,

$$N_{ph}(E_{ph}, x) = N_{ph}(E_{ph}, 0) \exp(-\alpha_{Si}(E_{ph})x) \quad (2-18)$$

defined by the photon absorption. So, the electron-hole pairs created, per unit volume in the energy range E_{ph} to $(E_{ph} + dE_{ph})$ at x , is

$$\begin{aligned} d[g(x)] &= -\frac{\partial}{\partial x} [N_{ph}(E_{ph}, x) dE_{ph}] \\ \Rightarrow d[g(x)] &= N_{ph}(E_{ph}, 0) \alpha_{Si}(E_{ph}) \exp[-\alpha_{Si}(E_{ph})x] dE_{ph}. \end{aligned} \quad (2-19)$$

The total generation rate at x is just the integral of the above expression over the entire energy spectrum [19]:

$$g(x) = \int_0^{\infty} N_{ph}(E_{ph}, 0) \alpha_{Si}(E_{ph}) \exp[-\alpha_{Si}(E_{ph})x] dE_{ph}. \quad (2-20)$$

The generation rate distribution in silicon under one-sum, air-mass-one (AM1) illumination at 300K, for zero reflection at the exposed surface, has been obtained by numerically evaluating the integral in (2-20) for values of x ranging from zero upward.

For 1-pass internal photon reflection the total electron-hole generation rate is assumed to be

$$g_{1-R}(x) = g(x) + g(2t_{Si} - x). \quad (2-21)$$

For multiple internal reflections, the total generation rate is similarly given by

$$g_{2-R}(x) = g(x) + g(2t_{Si} - x) + g(2t_{Si} + x) \quad (2-pass) \quad (2-22)$$

$$g_{3-R}(x) = g(x) + g(2t_{Si} - x) + g(2t_{Si} + x) + g(4t_{Si} - x) \quad (3\text{-pass}) \quad (2-23)$$

⋮
⋮
⋮

Note complete light trapping is modeled by $g_{n-R}(x)$ for a large n such that

$$\int_x^{x+\Delta x} g_{n-R}(x) dx \approx 0. \quad (2-24)$$

2.2 Model Application and Verification

We used our FLOODS setup to simulate simple 1-D version of the p^+n and p^+nn^+ solar cells shown in Fig. 2-2 to verify it, based on published results in the literature. The top p^+n junction forms the emitter of the device and the bottom nn^+ high-low (HL) diffused junction is used as a back-surface field (BSF). The front and bottom interfaces are passivated by thermally grown oxide, nitride, or by PECVD/RPCVD intrinsic amorphous silicon (a-Si:H). The BSF can bring significant improvement in the cell performance, if the minority-hole lifetime is long enough to ensure that the diffusion length (L_p) is much longer than the base thickness (W_b) [25]. Typical thickness of commercially available Si solar cells is about $200\mu\text{m}$ - $350\mu\text{m}$ [2], [25]–[29]. If $L_p \gg W_b$, the dark current can be reduced (and V_{OC} improved) by the incorporation of a back HL junction. Also the HL junction improves J_{SC} as the built-in electric field in the nn^+ diffusion region forces the minority holes away from the high- S_b back contact.

We initially assume a $250\mu\text{m}$ -thick ($t_{Si} = 250\mu\text{m}$) p^+n solar cell with no BSF and optimize the base donor doping density (N_B), with respect to minority-hole lifetime (τ_p) according to Eq. (2-5), (2-10), and (2-11). The top surface acceptor doping density (N_S)

is assumed to be 10^{19}cm^{-3} , with front surface recombination velocity $S_f=10^3\text{cm/s}$ which is achievable with good thermal oxide passivation [17]. Though minority-carrier lifetime as high as 1ms is attainable [7], [35], we assume $\tau_{p0} = \tau_{n0} = 400\mu\text{s}$ in Eq. (2-5) and (2-6). Simulation is done under AM1 photon spectrum with input incident power of 92.5mW/cm^2 [23]. FLOODS-predicted current-voltage (JV) and power-voltage characteristics are shown in Fig 2-3. The intrinsic efficiency (η_{int}) of solar cell is calculated as

$$\eta_{\text{int}} \equiv \frac{V_{\text{OC}}J_{\text{SC}}\text{FF}}{P_{\text{int}}} \quad (2-25)$$

where V_{OC} , J_{SC} and FF are intrinsic open-circuit voltage, short-circuit current density and fill factor respectively, and $P_{\text{int}}=92.5\text{mW/cm}^2$ at AM1 [23] incident optical power.

There are extrinsic losses that can be minimized by process optimization. These losses are shadowing (and reflecting) losses ($\sim 2.2\%$) at the front metal contact grid and front surface, resistive losses ($\sim 0.7\%$) associated with the base, emitter, BSF regions, and contacts, metal grids, and photon absorption losses ($\sim 1.4\%$) at back metal contact [2]. The near optimal intrinsic FF predicted by 1-D FLOODS simulations is also dependent on the base resistivity and on 2-D carrier flow through the device. FLOODS-predicted intrinsic performance (η_{int}) and the estimated extrinsic cell efficiency (η) taking into account the extrinsic losses are shown in Table 2-1.

We note in Table 2-1 that for p⁺n cells (without BSF), the cell performance is limited by the degree of back surface carrier recombination which is dependent on the base doping density. With base doping density $N_B=10^{15}\text{cm}^{-3}$, the hole diffusion length $L_p = \sqrt{D_p\tau_p} \approx 635\mu\text{m} \gg t_{\text{Si}}$, the base is transparent to the minority holes. Thus the dark

current is high due to higher recombination of holes at the high- S_b back surface. As the base doping density is increased, increased bulk recombination makes the base less transparent to the minority carriers. That is the effect of back surface minority-carrier recombination on V_{OC} is reduced with shorter diffusion length (L_p) as the base doping density is increased. The increase in V_{OC} with increased N_B is due to reduction in hole injection level ($\Delta p \propto 1 / \int_0^{W_b} N_D dx$) in the base and reduction in back surface recombination due to non-transparent base (where W_b is base thickness and N_D is base doping profile). However, photo-generated carrier collection efficiency (i.e., J_{SC}) decreases with increased N_B due to increased bulk recombination in addition to the back surface recombination. Decrease in FF at lower N_B is due to increase in high injection component of dark current (larger ideality factor, n). There is a trade-off between base transparency and back surface recombination and 10^{16}cm^{-3} is found to be near optimum base doping density.

The BSF is incorporated into the device by adding an nn^+ HL-junction near the back with $N_S = 3 \times 10^{20} \text{cm}^{-3}$ for the optimized $N_B = 10^{16} \text{cm}^{-3}$ cell. V_{OC} is improved by about 20mV (dark current density J_0 halved) and the loss in J_{SC} is recovered as shown in Table 2-1. The improvement in V_{OC} results from reduced carrier injection into the base

by increased integrated base doping density ($\int_0^{W_b} N_D dx$) and less carrier recombination

near back surface due to suppression of minority carriers. Minority-carrier suppression

near the back surface and built-in electric field ($E \propto \frac{dN_D}{dx}$) induced by BSF doping

profile effectively reflects the carriers away from the back surface resulting in improved

J_{sc} . V_{oc} in this p^+nn^+ device is limited by the Auger recombination in the heavily-doped BSF region which can be ameliorated by utilizing the trade-off between Auger recombination and back surface recombination. We also note that if $L_p \ll t_{Si}$ due to short τ_p , the BSF is less effective as shown in Table 2-2. The results predicted by FLOODS are consistent with those published in the literature [25]–[27], [35].

2.3 Summary

We have overviewed the heavy-doping effects and the device physics for thin silicon solar cells, and implemented it in FLOODS for 1-D and 2-D simulations. We have used our physics-based 1-D FLOODS setup to verify physical operation of the conventional back-surface field solar cells under AM1 sunlight (92.5mW/cm² input power). We believe our physical modeling for the heavily doped regions is quite reliable for bipolar devices like solar cells and is in agreement with those published in the literature.

Table 2-1. FLOODS-predicted performance of thick p⁺n cell versus base doping density. Device thickness $t_{si} = 250\mu m$, top surface doping density $10^{19}cm^{-3}$, minority-hole lifetime $\tau_{p0} = 400\mu s$. Performance enhancement via BSF (p⁺nn⁺) for the base doping density, $N_B=10^{16}cm^{-3}$ cell is shown as well. A back HL nn⁺ junction with $N_S=3 \times 10^{20}cm^{-3}$ is used as BSF with back surface recombination velocity $S_b=3 \times 10^4$ cm/s. η_{int} is intrinsic efficiency and η is estimated extrinsic efficiency.

Device Type	N_B (cm^{-3})	L_p (μm)	V_{oc} (mV)	J_{sc} (mA/cm^2)	FF (%)	η_{int} (%)	η (%)
NO BSF	10^{15}	635	561	35.2	80.9	17.3	15.7
NO BSF	10^{16}	423	617	34.9	82.9	19.3	17.1
NO BSF	10^{17}	143	664	32.0	83.6	19.2	16.8
BSF	10^{16}	423	637	36.2	83.1	20.7	18.2

Table 2-2. FLOODS-predicted performance of the p⁺nn⁺ cell versus minority-hole lifetime. Substrate thickness $t_{si} = 250\mu m$, base doping density $N_B=10^{17}cm^{-3}$, top surface doping density $10^{19}cm^{-3}$, back $N_S=3 \times 10^{20}cm^{-3}$, and back surface recombination velocity $S_b=3 \times 10^4$ cm/s.

τ_p (μs)	V_{oc} (mV)	J_{sc} (mA/cm^2)	FF (%)	η_{int} (%)	η (%)
160	637	36.2	83.1	20.7	18.2
16	604	34.5	82.6	18.6	16.5

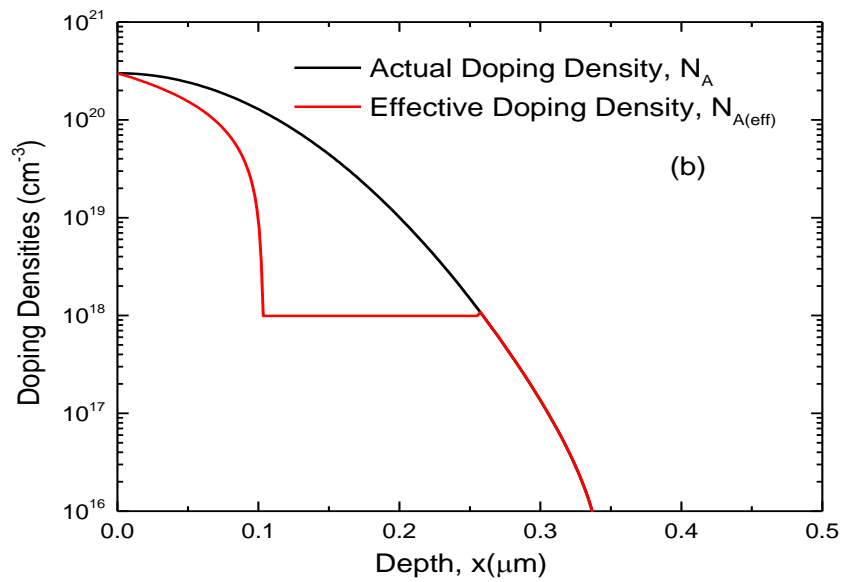
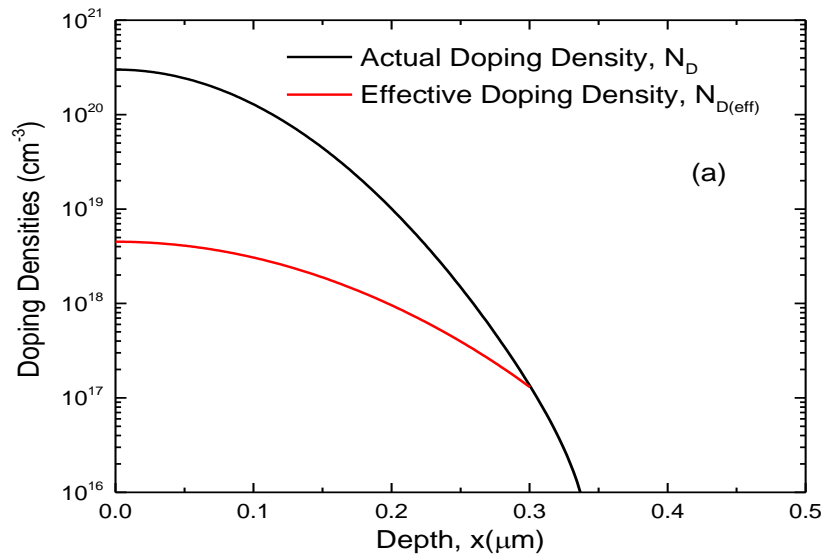


Figure 2-1. Effective and actual doping density profiles implemented in FLOODS for minority-carrier transport. Actual doping is a Gaussian doping profile with $N_S=3 \times 10^{20} \text{ cm}^{-3}$.

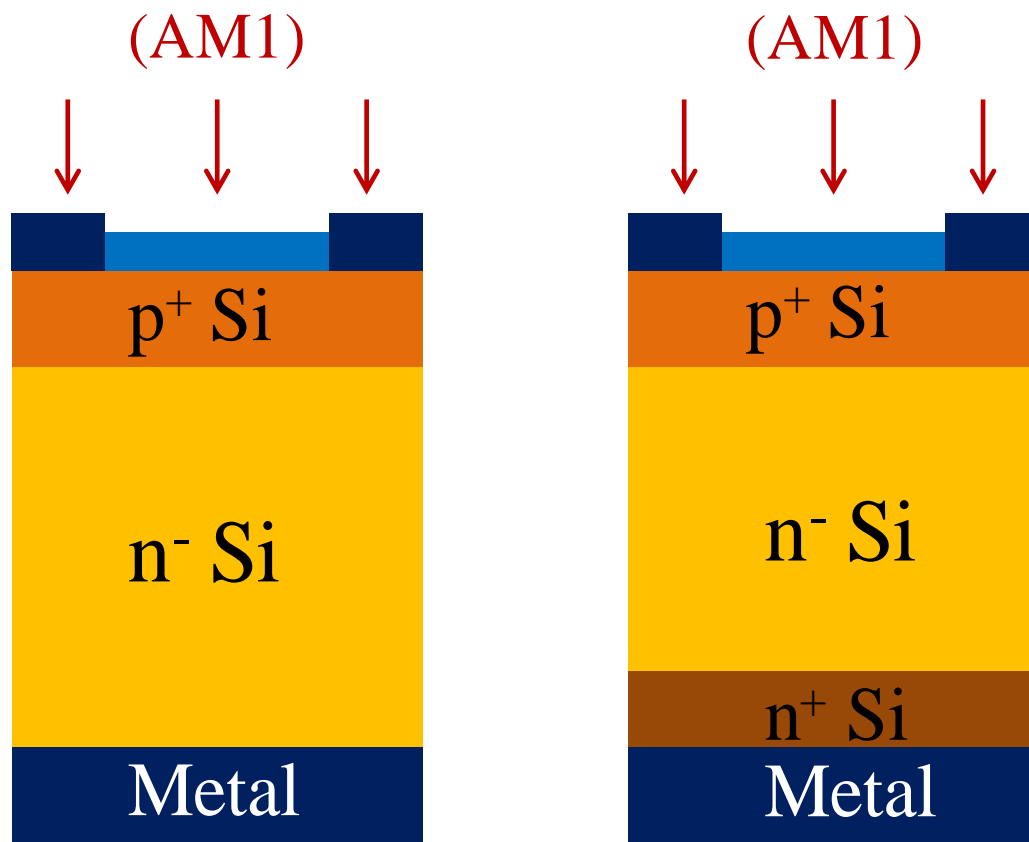


Figure 2-2. Schematic cross-sections of conventional p+n and p+nn+ solar cells. The high-low (HL) nn+ junction acts as a back-surface field (BSF).

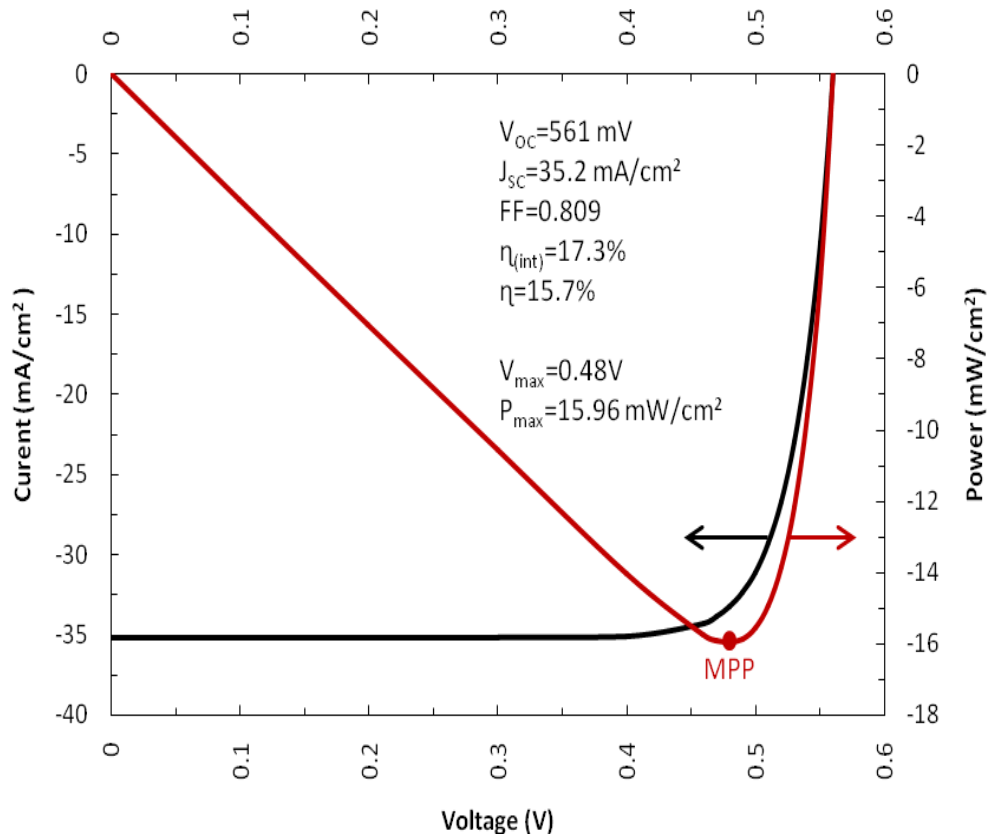


Figure 2-3. FLOODS-predicted illuminated JV and PV characteristics of thick p⁺n cell. Cell thickness $t_{Si} = 250 \mu m$, with no BSF at AM1 (92.5 mW/cm^2) sunlight. Base donor doping density $N_B = 10^{15} \text{ cm}^{-3}$, emitter $N_S = 10^{19} \text{ cm}^{-3}$, back surface is unpassivated ($S_b = 10^6 \text{ cm/s}$), and front surface recombination velocity $S_f = 1000 \text{ cm/s}$.

CHAPTER 3 LOCAL BSF INSIGHTS FOR THIN SOM SOLAR CELLS

As described in Chapter 2, the minority-carrier recombination in the base of the device can be reduced by introducing a back-surface field (BSF) if the minority-carrier diffusion length is longer than the cell thickness. However, with thinner devices ($t_{Si} < 100\mu\text{m}$), BSF can be effective even if the minority-carrier lifetime in the base is moderately short, i.e., even for cheaper silicon. But, the BSF must be optimized for high efficiency. There is an unavoidable Auger recombination in the BSF region that can limit the cell efficiency, and this must be traded-off against the back-surface recombination. Device engineering to effect this tradeoff is warranted [9]. Back-surface recombination can be reduced by reducing the back metal contact area and passivating most of the back surface with thermal oxide, and Auger recombination in the BSF region can be reduced by introducing local BSF. In this chapter, we present a more comprehensive analysis of BSF engineering with FLOODS [8].

The chapter begins with a quick background of BSF. Various design parameters to reduce the carrier recombination at the back side of the solar cell are: back contact width (w_m), contact pitch (w), surface recombination velocity of Si-SiO₂ interface (S_b), width of the BSF diffusion region (uniform or local), minority-carrier lifetime (τ) in the base, and device thickness (t_{Si}). These design parameters are varied systematically to gain physical insights on the recombination mechanisms in the solar cell, and to design optimum device structures. For thinner cells, design optimization of the BSF region and back contacts is very important. In order to isolate the carrier recombination at the front surface, front-surface recombination velocity was assumed low ($S_f = 1\text{cm/s}$).

3.1 Back-Surface Field and Simulation Setup in FLOODS

The back-surface field (BSF) can bring significant improvement in the cell performance, if the minority-carrier diffusion length ($L = \sqrt{D\tau}$) is longer than the base thickness W_b [25]. For a pn-junction diode in Fig. 3-1, the minority-hole current density (J_p) injected into the base from a p^+ emitter is can be modeled as

$$J_p = \frac{qn_i^2 \overline{D}_p}{\int_0^{w_b} n dx} \exp\left(\frac{qV_{EB}}{k_B T}\right) \quad (3-1)$$

$$\approx \frac{qn_i^2 \overline{D}_p}{\int_0^{w_b} N_D dx} \exp\left(\frac{qV_{EB}}{k_B T}\right) \quad (3-2)$$

where \overline{D}_p is the average hole diffusivity in the base and $\int_0^{w_b} N_D dx$ is the base Gummel number (N_G), V_{EB} is emitter-base forward bias, k_B Boltzmann constant, and T is absolute temperature. We see that dark current can be reduced (and V_{OC} improved) if a high-low (HL) nn^+ diffusion layer is introduced in the base to increase N_G . The BSF doping effectively reduces the minority-carrier concentration near the back surfaces, thus reducing the recombination. Also the HL junction improves the short-circuit current density J_{SC} , as the built-in electric field in the nn^+ diffusion region forces the minority holes away from the high- S_p back contact.

To get physical insights about local BSF and back contact design we set up FLOODS [8] for reliable physics-based numerical simulation in AM1 (92.5mW/cm²) sunlight. Modeling of optical carrier generation rate $g(x)$, recombination rates (SRH,

band-to-band Auger), mobility, energy-bandgap narrowing (ΔE_g) and F-D statistics in heavily doped regions was done as discussed in Chapter 2. An n-type base ($N_B \cong 10^{16} \text{cm}^{-3}$) was used in our simulation; similar results for p⁺ starting wafers can be projected from the simulations discussed here. A shallow p⁺n diffused junction on top was assumed, as we are interested in recombination at BSF diffusion region, back contact, and back non-metal surface (i.e. Si-SiO₂ interface). Front surface acceptor doping density $N_S \cong 10^{19} \text{cm}^{-3}$ with a junction depth of $x_j \cong 0.16 \mu\text{m}$ was assumed to minimize recombination losses in front p⁺ region. To eliminate front surface carrier recombination and effect of front contacts, and thus to focus on the back losses, a uniform quasi-ohmic top contact with low surface recombination velocity ($S_f = 1 \text{cm/s}$) was assumed.

3.2 Thin Cells with Uniform BSF Diffusions

The cross-section of a pn-junction solar cell with uniform BSF, and the basic 2-D FLOODS domain are illustrated in Fig. 3-1. The surface recombination velocity (SRV) at the back metal contact was assumed infinite ($S=10^6 \text{cm/s}$), and SRV at the Si-SiO₂ interface (i.e. non-metal back surface) S_b , which depends on the surface doping density, was taken as a variable design parameter. The value of S_b was determined from an empirical formula ($S \sim N_S \times 10^{-16} \text{cm}^{-3}$) [17]. Initially, we assumed minority-hole lifetime in the n-type base, $\tau_p = 1 \text{ms}$. At this long lifetime, minority-carrier (hole) diffusion length $L_p \cong 1000 \mu\text{m}$, which is much longer than silicon thickness $t_{\text{si}} = 25 \mu\text{m}$. Thus carrier recombination in the BSF region, and at the non-metal back surface and back contacts determines V_{OC} . Later in the chapter, we also present the physical insights on shorter

minority-carrier lifetime on device performance. We initially assumed a uniform n^+ diffusion at the back of the cell (Gaussian profile, $N_s = 10^{19} \text{cm}^{-3}$, junction depth $x_j \sim 0.3 \mu\text{m}$) to understand dependence of dark current density on Auger recombination in back n^+ region and on minority-carrier recombination at back metal contacts to the n^+ region.

We show in Table 3-1 the FLOODS-predicted performance of the uniform BSF p^+n^+ cell as described in Fig. 3-1 under AM1 optical illumination. The back contact widths (w_m) were varied as a design parameter for fixed $S_b=10^3 \text{cm/s}$, and pitch $w=300 \mu\text{m}$. We see V_{OC} increases by 23mV (and dark current density J_0 is reduced by a factor of about 2.5) when back contact width (w_m) is reduced from $10 \mu\text{m}$ to $2 \mu\text{m}$. This is largely due to the decrease in minority-carrier recombination at the back metal contact. Note that the minimum contact width is limited by process technology which is mostly done with a shadow mask, and narrower contact increases series resistance that can decrease FF. However, V_{OC} (as well as J_{SC}) is relatively unaffected by back non-metal surface recombination velocity as the uniform BSF suppresses minority-carrier density at back. Long diffusion length L_p makes J_{SC} insensitive to the variation of back contact width. We call this uniform BSF cell Structure-A.

Next, we varied the back contact pitch width (w) as a design parameter for the uniform BSF cell (Structure-A). The solar cell performance under AM1 illumination is shown in Fig. 3-2 and Fig 3-3. As the pitch width (w) is increased, recombination at the back metal contact decreases as reflected by improved V_{OC} with wider pitches. Improvement in V_{OC} , however, tends to saturate at wider pitches ($w>1 \text{mm}$) due to increased Auger recombination in the n^+ BSF and recombination at non-metal back

surface which tend to offset reduction in the back contact recombination. J_{SC} improves slightly with wider pitch (w), due to reduction carrier recombination at the back contact, and J_{SC} improves when w_m/w ratio is minimized. Fill factor (FF) is limited by pitch; as wider pitch means higher lateral ohmic drops which decreases FF. So there is a design tradeoff between V_{OC} and FF when designing pitch width. The optimum pitch width is $w \approx 600\mu m$ for $2\mu m$ -wide back contact opening and base minority-carrier lifetime of 1ms.

At this point, V_{OC} of the uniform BSF cell (Structure-A) is limited by the Auger recombination in the n^+ BSF region, and recombination at the back metal contact. Recombination at the back metal contact can be minimized further by incorporating a shallow heavy n^{++} doping profile around the back contact as shown in Fig. 3-4 (Structure-B). Minority-hole concentration (Δp) is inversely proportional to the doping density, and there is a built-in electric field induced by the gradient of doping profile ($E \propto \frac{dN_D}{dx}$). Thus, introduction of a shallow heavy doping profile ($N_S=3 \times 10^{20} \text{cm}^{-3}$, $x_j \sim 0.16\mu m$) around the back contact suppresses the minority-carrier concentration, and thereby it reduces carrier recombination at the back metal contact. We call this design Structure-B. As we see from FLOODS simulation in Table 3-2, V_{OC} increases to 702mV if a shallow heavy doping profile is introduced around the back contact regions. J_{SC} and FF remain unaffected with this optimization. However, a complex process is required to fabricate Structure-B design. Open-circuit voltage is still limited by the Auger recombination in the n^+ diffusion region. Auger band-band recombination can be eliminated by removing the uniform n^+ BSF region leaving only the shallow heavy

doping profile near the back contact as shown in Fig. 3-4. The shallow heavy doping profile around the back metal contact acts as a local BSF, and we call this design Structure-C.

3.3 Local BSF: Physical Insights and Design

We now extend our insights learned so far to design local BSF cells by completely removing the uniform BSF with only local doping around the back contact as illustrated in Fig. 3-4. This design (Structure-C) eliminates Auger recombination near the back of cell and thus improves V_{OC} , and since minority-carrier diffusion length $L_p \gg t_{Si}$, carrier collection efficiency (J_{SC}) is also good as we will see later. However, the absence of a uniform BSF turns the non-metal back surface (Si-SiO₂ interface) very critical – the interface could act as a recombination sink to the minority holes if the Si-SiO₂ interface is not well-passivated. Since local BSF width is small compared to the device width, a heavy doping profile is required to achieve sufficient built-in electric field. We initially assume a local BSF with $N_S=3 \times 10^{20} \text{cm}^{-3}$ and junction depth $x_j=0.3 \mu\text{m}$. For lower surface doping density $N_S=10^{19} \text{cm}^{-3}$, deeper junction depth ($x_j \approx 1$ to $1.5 \mu\text{m}$) is required to achieve similar performance. For our FLOODS simulation, we assumed infinite SRV at the back contact ($S=10^6 \text{cm/s}$), base doping density $N_B=10^{16} \text{cm}^{-3}$, minority-hole lifetime of $\tau_p = 1 \text{ms}$, and contact width $w_m=2 \mu\text{m}$. The SRV (S_b) of the non-metal back surface (Si-SiO₂ interface), and pitch width (w) were varied as a design parameter for the local BSF cell (Structure-C).

We note that V_{OC} and J_{SC} are strongly dependent on S_b , as shown in Fig. 3-5. V_{oc} decreases sharply for $S_b \geq 30 \text{cm/s}$ due to heavy recombination at the non-metal back surface; similar decrease in J_{SC} is also noticeable for $S_b \geq 100 \text{cm/s}$. For our subsequent

studies we assumed $S_b = 10\text{cm/s}$ which is achievable with thermal oxide passivation. Fig. 3-6 and Fig. 3-7 show the performance dependence of local BSF cells on pitch width with Si-SiO₂ interface recombination velocity (S_b) as a parameter. Table 3-3 shows the predicted performance of local BSF cells for different contact pitch widths with Si-SiO₂ interface SRV $S_b=10\text{cm/s}$. We see increased V_{OC} due to elimination of Auger recombination from the back of the device (but poor non-metal back surface passivations $S_b \geq 100\text{cm/s}$, offsets this dark current reduction with pitch) and relatively smaller FF due to increased lateral ohmic drops as conductivity decreases when uniform BSF is removed. As we have seen earlier for uniform BSF cases, V_{OC} (and J_{SC} slightly) increases and FF decreases with wider pitch giving optimum efficiency at pitch width $w=600\mu\text{m}$ in local BSF cells. Optimum pitch width decreases if non-metal back surface is not passivated ($S_b \geq 100\text{cm/s}$). For thicker cells ($t_{Si} \geq 80\mu\text{m}$) however, J_{SC} remains almost independent of pitch variations. In Table 3-2, we show a comparative performance analysis for the uniform BSF cell (Structure-A), uniform BSF cell with shallow doping around metal (Structure-B), and local BSF cells (Structure-C) for contact width $w=2\mu\text{m}$, pitch width $w_m=300\mu\text{m}$, and minority-carrier lifetime of 1ms.

3.4 Performance Dependence on Thickness Variation

We now try to understand effects of varying silicon thickness (t_{Si}) on the local BSF device performance, which is influenced by the minority-carrier lifetime, non-metal back surface passivation, pitch (w), and contact width (w_m). For this analysis we assume, pitch $w=600\mu\text{m}$, contact width $w_m=2\mu\text{m}$ that give optimal performance for silicon thicknesses of $t_{Si}=80\mu\text{m}$ and $150\mu\text{m}$ at back surface recombination velocity, $S_b=10\text{cm/s}$ and base doping density, $N_B=10^{16}\text{cm}^{-3}$. We show in Fig. 3-8, the device performance

parameters for 25 μm , 80 μm , and 150 μm thick cells with and without 1-pass internal photon reflection for different minority-carrier lifetimes. V_{OC} (and dark current density) depends strongly on non-metal back surface passivation and bulk SRH lifetime (and hence device thickness), on the other hand, J_{SC} is weakly dependent on bulk lifetime as long as minority-carrier diffusion length is sufficiently longer than the device thickness and non-metal back surface is passivated ($S_b \sim 10\text{cm/s}$) or opaque by uniform BSF.

We note in Fig. 3-8, V_{OC} decreases with increase in device thickness due to increase bulk SRH recombination, however, optically generated electron-hole collection (or J_{SC}) is good as long as $L_p \gg t_{si}$. For longer hole lifetimes ($\sim 1\text{ms}$) in the base, the thicker (150 μm) cells performs better than the thinner cells (25 μm and 80 μm), see Fig. 3-9. This is due to higher J_{SC} in thicker devices (150 μm) where $L_p \gg t_{si}$, and due to comparatively less fractional decrease in V_{OC} for thicker device arising from bulk SRH recombination. For shorter lifetimes ($\sim 16\mu\text{s}$), the thinner cells perform better, probably because of higher V_{OC} and comparable J_{SC} with or without 1-pass internal reflection. Here we argue that for low-cost silicon starting materials (i.e. minority-carrier lifetime short), V_{OC} can be improved by increasing base doping density ($N_B > 10^{16}\text{cm}^{-3}$) which decreases dark current density by reducing minority-carrier injection in the base without affecting J_{SC} much as long as $L_p \gg t_{si}$. Thus we argue that 25 μm is a near optimum thickness for low grade starting silicon materials with local BSF designs.

3.5 Summary

We have gained physical insights about recombination mechanism in a thin c-Si solar cell and how a BSF doping profile can improve cell performance by reducing minority-carrier concentration near back of the surface. We have systematically

analyzed different BSF and back contact design structures. Effectiveness of the BSF can be significant if local doping and local contact designs are adopted. This is particularly important for thin ($t_{Si}=20-30\mu\text{m}$) c-Si solar cells. We have also shown dependence of device performance on back local contact width and pitch, and on device thickness with or without internal photon reflection.

Table 3-1. FLOODS-predicted performance versus back metal contact width for p⁺nn⁺ uniform BSF cell (Structure-A). Back contact pitch $w = 300\mu m$, $t_{Si} = 25\mu m$, back $N_s = 10^{19} cm^{-3}$, $S_b = 10^3 cm/s$, base $N_B = 10^{16} cm^{-3}$, lifetime $\tau_p = 1ms$, $S_f = 1cm/s$. Note, S_f is assumed low to minimize front surface recombination.

$w_m(\mu m)$	J_{SC} (mA/cm ²)	V_{OC} (mV)	FF (%)	η_{int} (%)
10	32.47	666	84.0	19.54
2	32.51	689	83.0	20.17

Table 3-2. FLOODS-predicted performances of three thin BSF cell design architectures. Performances of uniform BSF cell (Structure-A), uniform BSF with a shallow local doping (Structure-B), and local BSF cell (Structure-C) are shown. Assumed parameters are $w_m = 2\mu m$, $w = 300\mu m$, $t_{Si} = 25\mu m$, uniform BSF $N_s = 10^{19} cm^{-3}$, shallow doping $N_{S(local)} = 3 \times 10^{20} cm^{-3}$, $S_b = 10^3 cm/s$, base $N_B = 10^{16} cm^{-3}$, lifetime $\tau_p = 1ms$.

Structure	Shallow doping around back contact	Uniform BSF	$w_m(\mu m)$	J_{SC} (mA/cm ²)	V_{OC} (mV)	FF (%)	η_{int} (%)
A	NO	YES	2	32.51	689	83.0	20.17
B	YES	YES	2	32.52	702	83.0	20.48
C	YES	NO	2	32.53	726	82.4	21.03

Table 3-3. FLOODS-predicted performance versus back contact pitch for local BSF cell (Structure-C). Assumed parameters are: lifetime $\tau_p = 1\text{ms}$, Si-SiO₂ interface SRV $S_b=10\text{cm/s}$, SRV at back contact $S=10^6\text{cm/s}$, contact width $w_m=2\mu\text{m}$, uniform BSF $N_S=1\times 10^{19}\text{cm}^{-3}$, shallow doping $N_{S(\text{local})}=3\times 10^{20}\text{cm}^{-3}$

Device Structure	Pitch w (μm)	J_{SC} (mA/cm^2)	V_{OC} (mV)	FF (%)	η_{int} (%)
Local BSF	1000	32.53	736	81.0	20.97
Local BSF	600	32.53	733	81.7	21.06
Local BSF	300	32.53	726	82.4	21.03

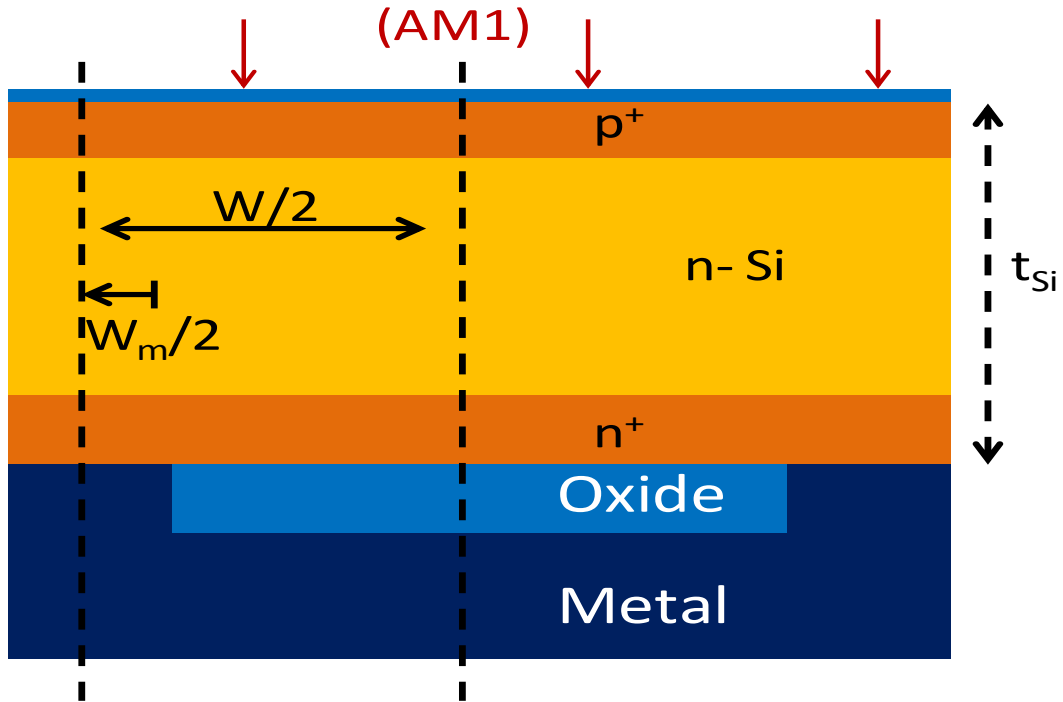


Figure 3-1. Cross-section of pn-junction solar cell with uniform BSF. The basic FLOODS domain for 2-D numerical simulations is also shown. The front emitter is an n^+ layer with $x_j=0.16\mu\text{m}$. A low front surface recombination velocity ($S_f=1\text{cm/s}$) is assumed to minimize front surface recombination, and to focus on carrier recombination at the back of the device.

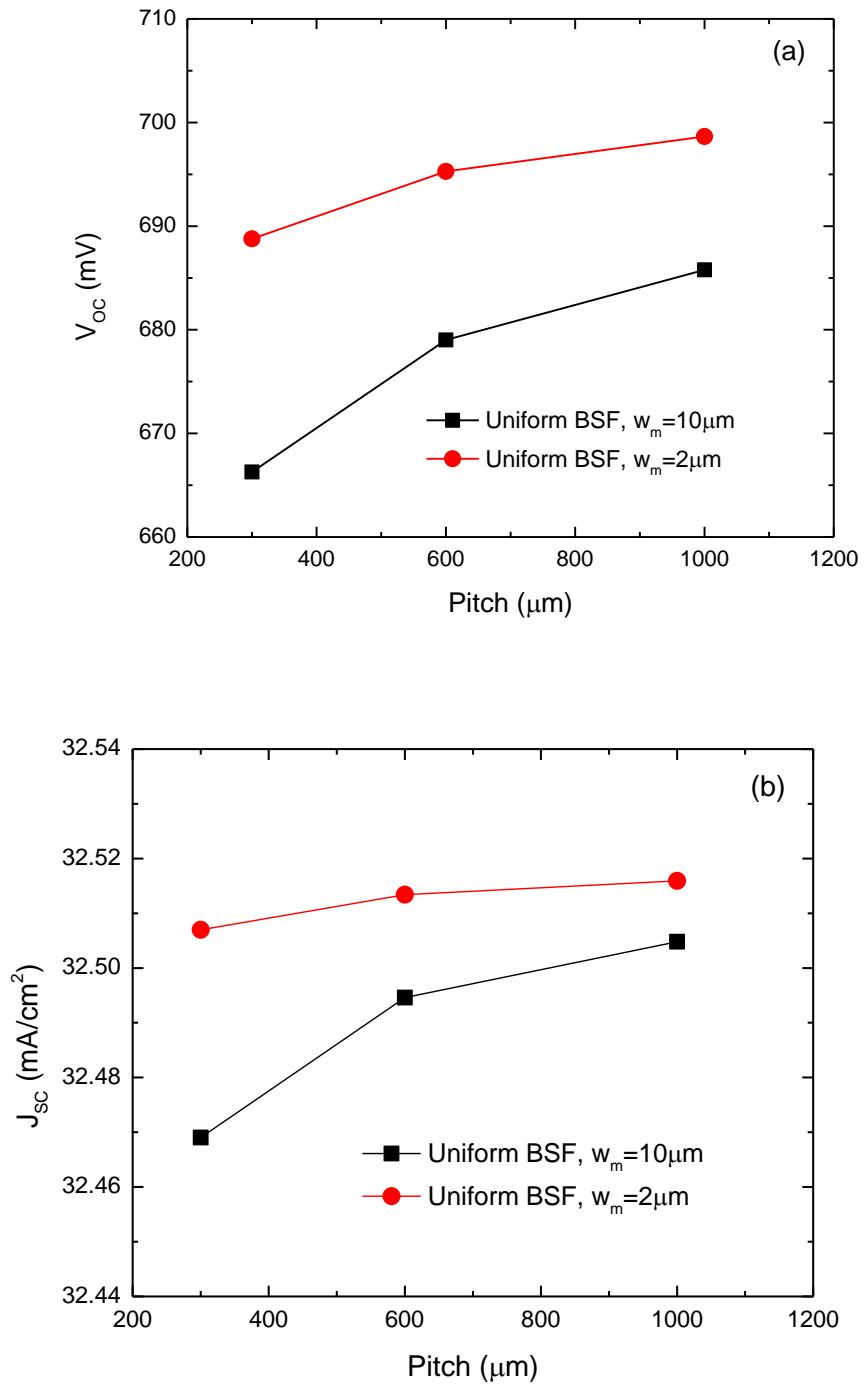


Figure 3-2. FLOODS-predicted V_{OC} , and J_{SC} performance as a function of back contact pitch width for uniform BSF cell (Structure-A). Performances of both the 10 μm - and 2 μm -wide (pitch) back contact cells are shown; with $t_{Si} = 25\mu\text{m}$, $\tau_p = 1\text{ms}$.

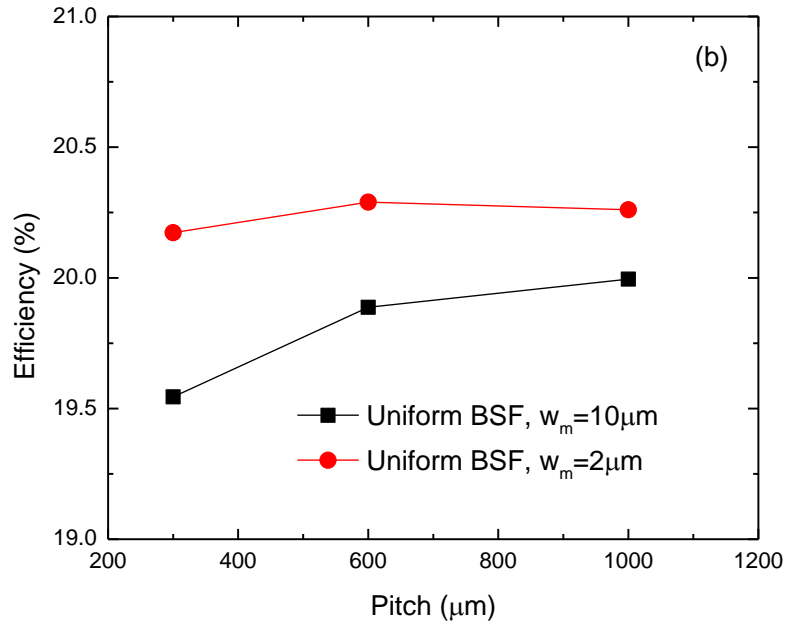
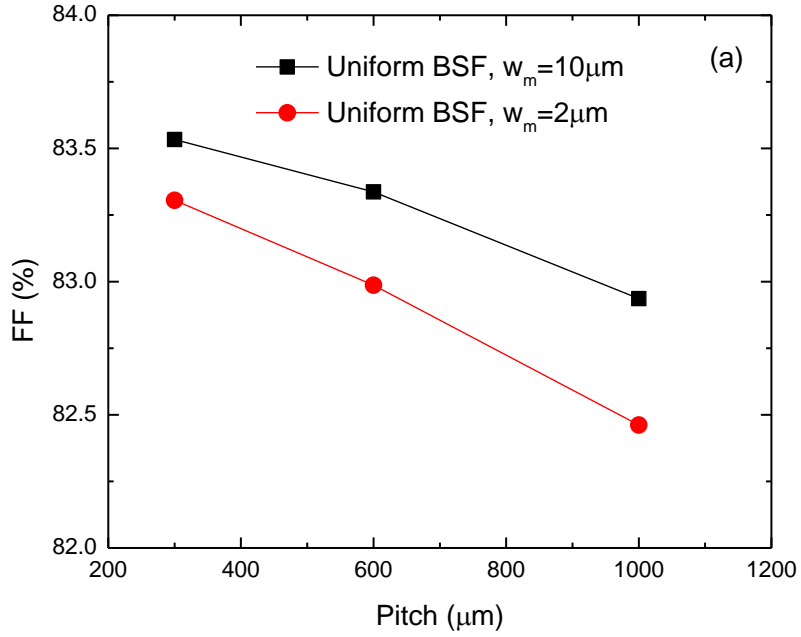


Figure 3-3. FLOODS-predicted FF, and efficiency performance as a function of back contact pitch width for uniform BSF cell (Structure-A). Performances of both the 10 μm - and 2 μm -wide (pitch) back contact cells are shown; with $t_{\text{Si}} = 25\mu\text{m}$, $\tau_p = 1\text{ms}$.

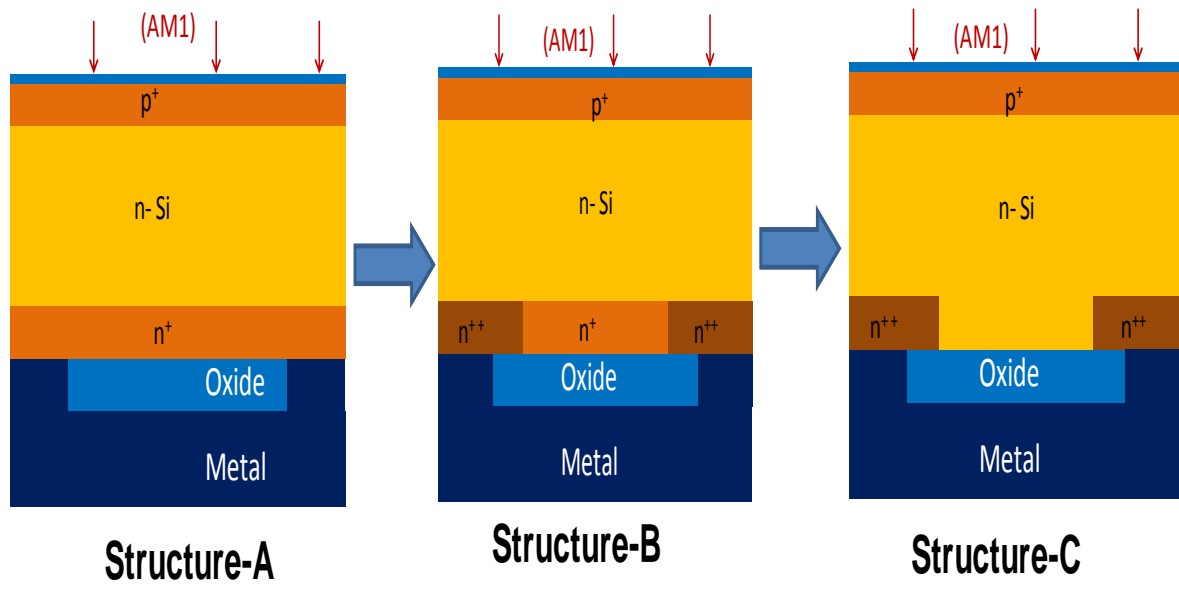


Figure 3-4. Cross-sections of three thin BSF solar cell architectures. Structure-A: uniform BSF cell, Structure-B: uniform BSF with a shallow heavy doping around back metal contacts, and Structure-C: local BSF cell. Top p⁺n junction depth 0.16 μ m with top surface recombination velocity $S_f=1$ cm/s.

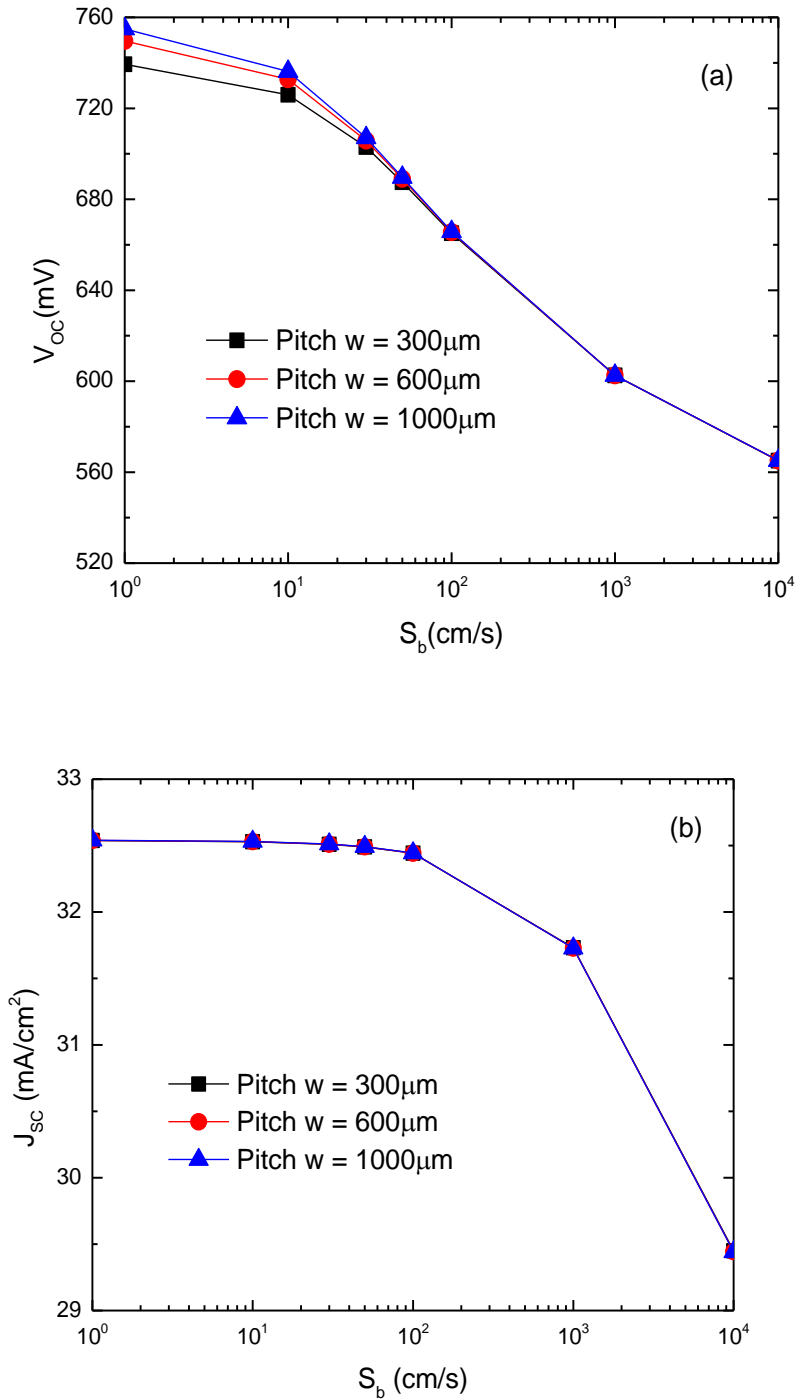


Figure 3-5. FLOODS-predicted V_{OC} and J_{SC} performance versus S_b with back contact pitch as a parameter for local BSF cell (Structure-C). S_b is SRV at Si-SiO₂ interface, hole lifetime $\tau_p = 1\text{ms}$, $w_m = 2\mu\text{m}$, $N_S = 3 \times 10^{20}\text{cm}^{-3}$, $N_B = 10^{16}\text{cm}^{-3}$ under AM1 (92.5mW/cm²) sunlight.

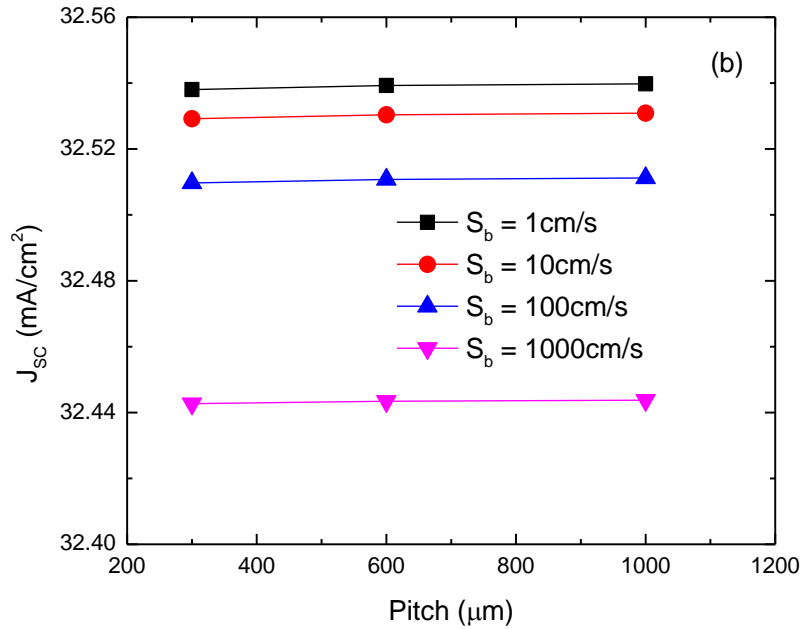
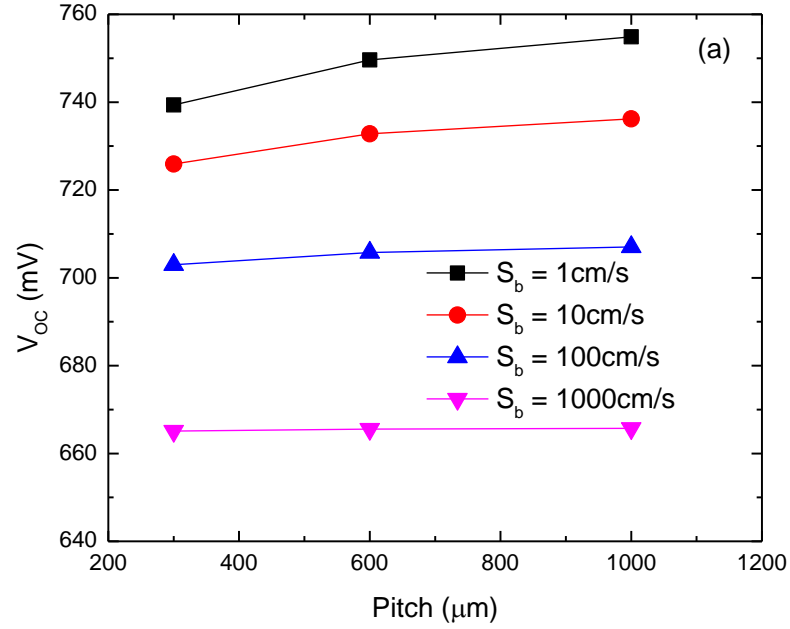


Figure 3-6. FLOODS-predicted V_{OC} and J_{SC} performance versus back contact pitch with S_b as a parameter for local BSF cell (Structure-C). S_b is SRV at the Si-SiO₂ interface, hole lifetime $\tau_p = 1\text{ms}$, $t_{Si} = 25\mu\text{m}$, back $N_S = 3 \times 10^{20}\text{cm}^{-3}$, contact width $w_m = 2\mu\text{m}$, under AM1 (92.5 mW/cm^2) sunlight.

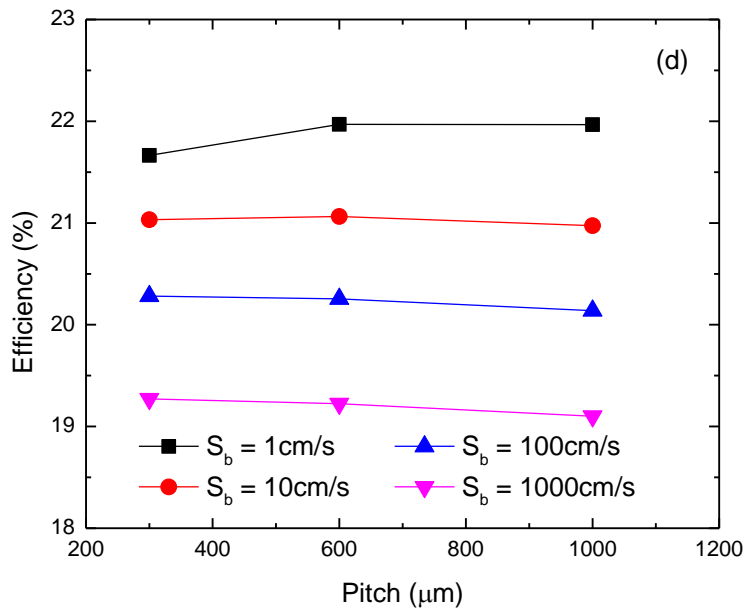
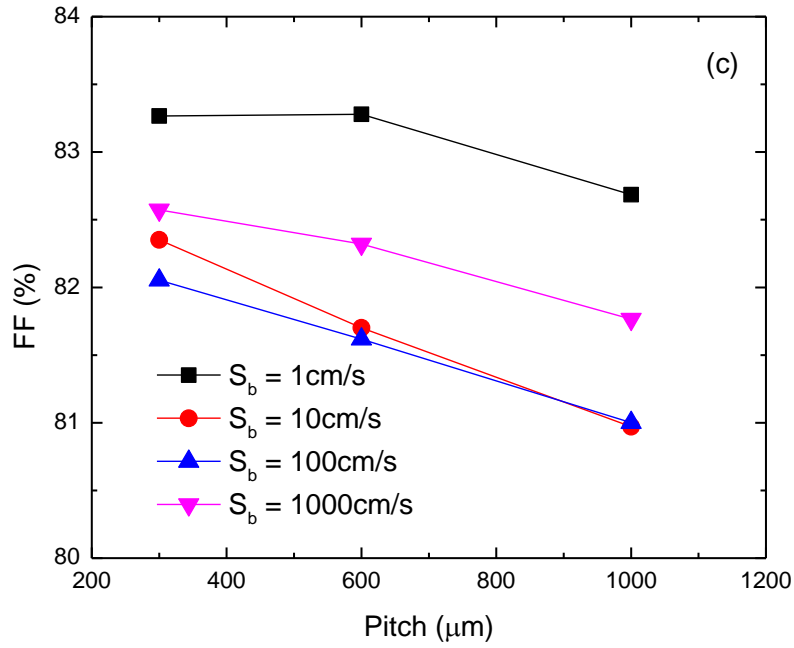


Figure 3-7. FLOODS-predicted FF and efficiency versus back contact pitch with S_b as a parameter for local BSF cell (Structure-C). S_b is SRV at the Si-SiO₂ interface, hole lifetime $\tau_p = 1 \text{ ms}$, $t_{Si} = 25 \mu\text{m}$, back $N_S = 3 \times 10^{20} \text{ cm}^{-3}$, contact width $w_m = 2 \mu\text{m}$, under AM1 (92.5 mW/cm^2) sunlight.

t_{si} (μm)	W/ Internal Reflection											
	1ms				160us				16us			
	Jsc (mA/ cm^2)	Voc (mV)	FF	η_{int} (%)	Jsc (mA/ cm^2)	Voc (mV)	FF	η_{int} (%)	Jsc (mA/ cm^2)	Voc (mV)	FF	η_{int} (%)
25	34.3	735	0.817	22.25	34.3	717	0.813	21.63	34.2	687	0.784	19.89
80	36.5	725	0.819	23.42	36.4	690	0.820	22.24	35.6	635	0.811	19.84
150	37.4	715	0.821	23.74	37.2	671	0.824	22.25	35.6	616	0.818	19.40
t_{si} (μm)	W/O Internal Reflection											
	1ms				160us				16us			
	Jsc (mA/ cm^2)	Voc (mV)	FF	η_{int} (%)	Jsc (mA/ cm^2)	Voc (mV)	FF	η_{int} (%)	Jsc (mA/c m^2)	Voc (mV)	FF	η_{int} (%)
25	32.53	733	0.817	21.06	32.5	715	0.814	20.48	32.4	684	0.786	18.84
80	35.19	724	0.819	22.57	35.1	688	0.820	21.45	34.5	634	0.811	19.18
150	36.31	714	0.821	23.01	36.1	670	0.824	21.58	34.8	616	0.819	18.95

Figure 3-8. FLOODS-predicted comparative performance analysis versus hole lifetime with device thickness as a parameter for local BSF cell (Structure-C). Effect of internal photon reflection is also shown. Assumed parameters are: pitch $w = 600\mu\text{m}$, contact width $w_m = 2\mu\text{m}$, $S_b = 10\text{cm/s}$, local BSF $N_S = 3 \times 10^{20}\text{cm}^{-3}$, $N_B = 1 \times 10^{16}\text{cm}^{-3}$.

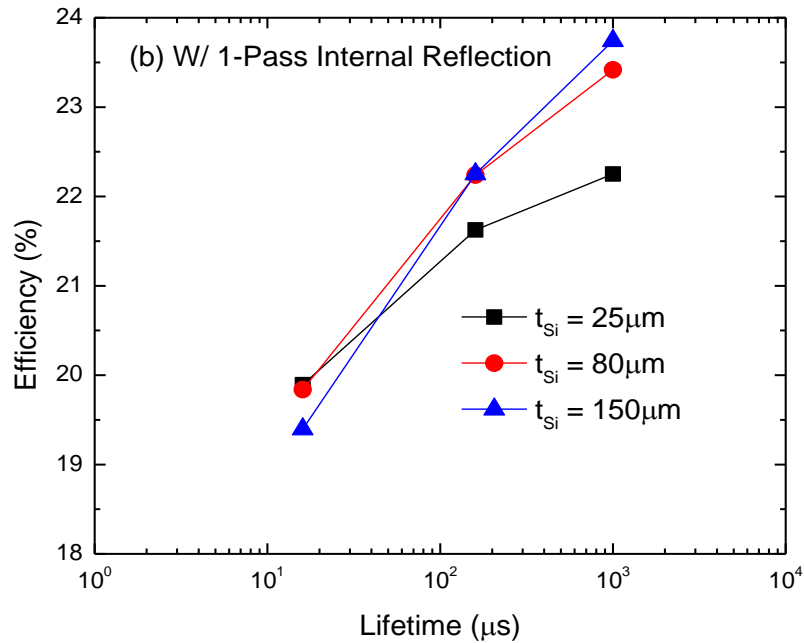
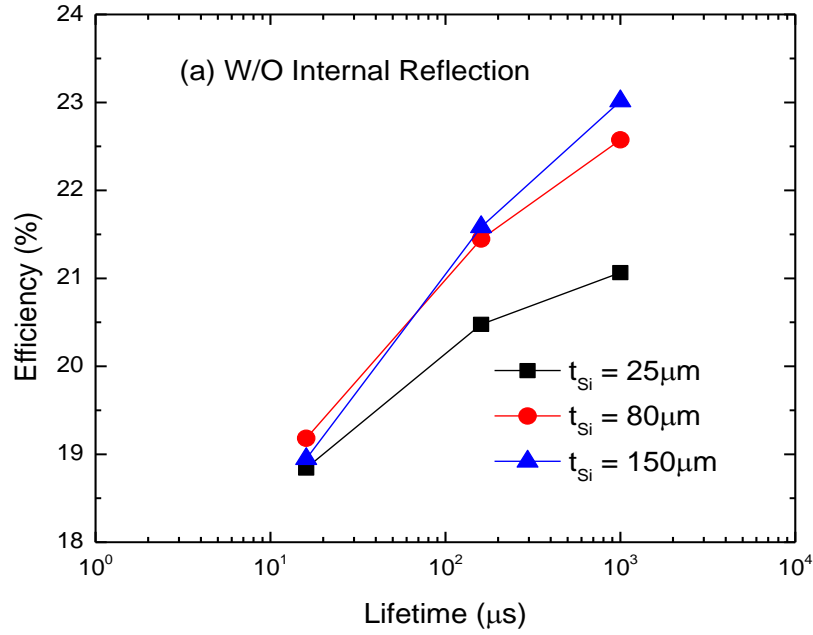


Figure 3-9. FLOODS-predicted local BSF cell (Structure-C) efficiency versus hole lifetime for different cell thicknesses. Assumed parameters: $w=600\mu\text{m}$, $w_m=2\mu\text{m}$, $S_b=10\text{cm/s}$, $N_s=3\times 10^{20}\text{cm}^{-3}$, $N_b=10^{16}\text{cm}^{-3}$ under AM1(92.5mW/cm^2) sunlight. (a) W/O internal photon reflection, (b) W/ 1-pass internal reflection.

CHAPTER 4 BACK-CONTACT SOLAR CELLS IN THIN CRYSTALLINE SILICON

Back-contact (BC) solar cells are of much interest because of their potential high efficiencies. The main features of back-contact solar cells are that the front grid-reflection and –shadowing losses and front grid-resistance losses are eliminated. Hence, the optical performance optimization of top surface, and the electrical performance optimization of back junctions and contacts are isolated and independent from each other. However, BC cells require starting material with longer minority-carrier lifetimes and most of these cells are fabricated on thicker substrates ($\sim 150\mu\text{m}$) with relatively costly process technologies [7]. Hence, development of BC solar cells on thinner substrates is necessary to offset the higher cost associated with device fabrication. The work reported in this chapter is based on a novel kerf-free process [3] for achieving crystalline silicon with $t_{\text{Si}} \cong 25\mu\text{m}$ on metal (SOM), which does not involve expensive steps like ion implantation and epitaxy, and on fabrication of back-contact (BC) solar cells in the thin silicon wafers, which has never been done before. The “BCSOM” process is described, preliminary experimental results are reported, and 2-D numerical simulations are used to define the optimal BCSOM cell design and to project the ultimate one-sun performance.

4.1 Novel Thin-Silicon BC Solar Cell Process

The first-ever BCSOM cell, unrefined but fully processed, is pictured in Fig. 4-1. Prior to the SOM exfoliation, interdigitated phosphorous-doped n^+ and boron-doped p^+ regions were diffused into a 3.5-inch p^- silicon wafer using POCl_3 and solid-source boron, respectively. The surface was then passivated with a thin thermal SiO_2 layer, and LPCVD nitride was deposited over the oxide. The metal-contact regions were defined

lithographically (although we plan to ultimately use a novel simplified back-contact process). A thin ($t_{\text{Si}} \cong 25\mu\text{m}$) silicon layer was then separated from the mother wafer using a novel exfoliation process [3]; the exposed surface shows some texturing. The SOM foil, flexible as shown in Fig. 4-2, was further processed through a nitride-layer deposition for the ARC and formation of the metal contacts to the diffused regions. The BCSOM cell shown in Figs. 4-1 and 4-2 does not include three planned major refinements: front-surface passivation, via a diffused FSF [30] and/or amorphous-Si PECVD [31], [32], optimally minimized back metal-contact areas (as described below, and which will be done in the mentioned simplified BC process), and optimized front- and back-surface texturing for enhanced photon absorption and internal reflection.

Measured current-voltage characteristics of the $25\mu\text{m}$ BCSOM solar cell, albeit unrefined, imply the viability of our novel process. We show in Fig. 4-3 a characteristic obtained with a conventional solar simulator (which is not yet modified for BC cells), for back-side one-sun illumination ($\cong 100\text{mW}/\text{cm}^2$), with the current normalized to the unshaded area. We get $J_{\text{SC}} \cong 33\text{mA}/\text{cm}^2$, which implies good collection efficiency; based on this result and our simulations (see below), good collection efficiency can be inferred for front-side illumination as well. The measured characteristic reveals significant shunt conductance in our unrefined cell, likely at the periphery of the wafer. When it is eliminated, we infer the actual $V_{\text{OC}} \cong 620\text{mV}$, which is less than what we anticipate (based on our simulations) mainly because the front-surface passivation has not yet been integrated in the process. In fact, these data, when put in perspective based on our simulations (e.g., see Tables 4-1 and 4-2), imply a photovoltaic performance that is well in line with our projections.

Whereas efficient BC cells with today's common Si-wafer thicknesses greater than 150 μm necessitate "extraordinarily" long ($>1\text{ms}$) carrier lifetime [30], and hence high-quality silicon, we believe, as argued herein, that our thin crystalline silicon can be used to better exploit the BC architecture even with shorter lifetimes. Our ultimate, simplified 25 μm BCSOM-cell process will feature effective surface passivations, surface texturing, optimal back-side diffusions and metallization, internal photon reflection, and good yield. We project, based on numerical device simulations and optimal cell-design criteria implied by them, and on the preliminary experimental results exemplified in Fig. 4-3, an ultimate efficiency, without internal photon reflection, near 20%.

4.2 2-Dimensional Numerical Simulations

To project thin- t_{Si} BC cell efficiencies and to aid their optimal design, we have used 2-D object-oriented numerical device simulator FLOODS [8]. As described in Chapter 2, FLOODS was first augmented for reliable physics-based numerical simulation of thin-Si solar cells in AM1 (92.5mW/cm²) sunlight. This tool provides flexibility for general simulations that commercial tools do not. The setup includes (i) characterization of the electron-hole generation rate defined by the AM1 photon absorption, with or without internal photon reflection, (ii) modeling of SRH and (band-band) Auger carrier recombination rates with lifetimes dependent on doping densities, (iii) modeling of carrier mobilities (and diffusion lengths) dependent on doping densities, and (iv) physical accounting for energy-bandgap narrowing and Fermi-Dirac statistics in heavily doped regions.

For thin cells, the features of heavily doped silicon [i.e., Auger recombination, bandgap narrowing (ΔE_g), and carrier degeneracy, or Fermi-Dirac (F-D) statistics] are

most important since much of the Si-cell structure must be heavily doped. In FLOODS, we physically account for ΔE_g and F-D statistics by using an effective doping density to model the minority-carrier transport. The Auger minority-carrier lifetime fundamentally varies inversely with the square of the majority-carrier, or doping density. We believe our physical modeling for the heavily doped regions is quite reliable for bipolar devices like solar cells. It is in good agreement with the physically well-interpreted experimental results reported in [17] for heavily doped regions.

4.3 BC Cell Design and Performance Projections

The basic BC solar cell structure (i.e., the 2-D FLOODS domain) that we assume is illustrated in Fig. 4-4. The front p^+ (or n^+) region, or FSF, which is essential in thick BC cells [30], is a BCSOM option, albeit with some process complexity. However, it can likely be avoided in optimal design as we show. The SOM process [3] yields silicon thickness $t_{Si} \cong 25\mu m$, which we assume as nominal, with about $\pm 5\mu m$ variations. Whereas an n-type base will ultimately be used because of the “photon-induced degradation” that occurs in a p-type base [33], our preliminary BCSOM fabrication has been done with unintentionally doped p^- starting wafers. We thus assume here that the cell base is p^- with $N_B \cong 10^{16} \text{ cm}^{-3}$, which implies a best-case (after-process) minority-electron lifetime (τ_n) possibly longer than 1ms [17], [30], [34]. (One-sun operation of the cell with this doping density produces low injection, which renders τ_n the relevant lifetime.) Lower doping at $\sim 10^{15} \text{ cm}^{-3}$ could yield longer lifetime directly [34], and indirectly because of high injection. However, our simulations show that the degradation of the fill factor (FF) due to the high injection is predominant, implying that

$N_B \sim 10^{16} \text{cm}^{-3}$ is optimal. For this doping density, we initially assume $\tau_n = 1 \text{ms}$, but later show good thin- t_{Si} BC cell performance for shorter lifetimes. Other important device parameters are the front-surface recombination velocity (S_f), the back, nonmetal-surface recombination velocity (S_b), which depends on the heavy surface doping density (N_s) [17], the widths of the back interdigitated n^+ and p^+ regions (w_n and w_p), and the widths of the respective metal-contact lines (w_{mn} and w_{mp}). Later we discuss the possible benefit of spaced contact windows in the z direction as noted in Fig. 4-4. Analogous results for an n^- base can be inferred from the simulations discussed here.

We initially assume moderate n^+ and p^+ diffusions at the back of the cell (i.e., gaussian profiles with $N_s = 10^{20} \text{cm}^{-3}$ and junction depth of about $0.3 \mu\text{m}$), which trade-off the bulk-Auger and surface recombinations for high open-circuit voltage (V_{OC}) [16], [17], [34], although not optimally. Later we derive optimal, lighter doping densities, and discuss the ultimate V_{OC} attainable. Such design optimization is possible with BC cells since the metal shadowing is not an issue, although w_{mn} and w_{mp} must be restricted to avoid excessive carrier recombination at the metal contacts as we discuss later.

For thin t_{Si} , the only τ_n requirement is that it be long enough to render the minority-electron diffusion length ($L_n \cong 1700 \mu\text{m}$ as defined by the assumed τ_n and the electron diffusivity) in the base much longer than w_p . Then, surface recombination losses must be suppressed for maximum efficiency. The front surface of the cell, which is the surface exposed after the thin-silicon exfoliation [3], can be subsequently passivated at low temperature via an amorphous-Si PECVD process [31], [32], prior to the ARC deposition. Without an FSF, effective surface passivation is crucial for high

efficiency (see below). The nonmetal back surface can be well passivated, before the thin-silicon formation, via a thermal oxide [17], [35]. We find that $S_b \sim 10^4 \text{ cm/s}$, which is commensurate with the assumed N_s [17], is adequate, but lower S_b can yield some improvement to the BC cell performance; higher S_b degrades the short-circuit current density (J_{SC}) as well as V_{OC} significantly (see Fig.4-5).

To stress the importance of S_f , we give in Table 4-1 thin- t_{Si} BC-cell AM1 performances predicted via FLOODS 2-D simulations for varying S_f and no FSF, with $S_b = 10^4 \text{ cm/s}$, $w_n = w_p = 150 \mu\text{m}$, and, initially, $w_{mn} = w_{mp} = 19.6 \mu\text{m}$ (about 13% metal contact coverage of the n^+/p^+ regions). The assumed domain width of only $150 \mu\text{m}$ is seemingly quite narrow, given the noted long L_n . However, we make this assumption initially to isolate the effects of S_f and later as a basis for checking performances for wider w_n and w_p , with possible asymmetry. In Table 4-1 we give the predicted intrinsic efficiency (η_{int}) and the actual efficiency (η), derived using estimated ARC-associated losses of 5% and assuming negligible I^2R losses in the metal (as implied by allowed liberal back-metal coverage). We do not account for any internal photon reflection here, although preliminary data suggest that our BCSOM process yields some. We see that $S_f \sim 10 \text{ cm/s}$, which is seemingly doable [31], [32], is needed for near-maximum efficiency. The predicted performance is substantially improved by the low S_f due to reduced recombination losses at the top surface that impact V_{OC} as well as J_{SC} , as shown experimentally in [32]. For $S_f = 10 \text{ cm/s}$, the predicted current in Table 4-1 reflects a 97% internal collection efficiency.

We checked the benefit of the p⁺ (and n⁺) FSF as well. For $S_f = 10^4 \text{ cm/s}$, which is commensurate with the FSF surface doping density [17], the predicted performance is a bit inferior to that for $S_f = 10 \text{ cm/s}$ in Table 4-1, due mainly to reduced J_{sc} and some V_{oc} lowering. These losses can be mitigated some by using very high surface doping density and shallow junction depth for the FSF, but the optimal passivation appears to be the noted (intrinsic) a-Si process [31], [32] without the FSF, if, indeed, $S_f \sim 10 \text{ cm/s}$ can be achieved.

For the $S_f = 10 \text{ cm/s}$ cell in Table 4-1, the predicted performance ($\eta_{int} = 18.5\%$ and $\eta \cong 17.6\%$) is limited by the noted collection efficiency, and by $V_{oc} = 649 \text{ mV}$, or the dark current, which comprises largely minority-carrier recombination at the back metal contacts to the n⁺/p⁺ regions. In fact, we find that J_{sc} as well as V_{oc} is limited by recombination sensitive to the metal-contact width. The predicted cell performances in Table 4-2 for decreasing fractional metal-contact width (w_m/w where $w_m \equiv w_{mi} = w_{mp} = 150 \mu\text{m}$) reflect this insight, and suggest that w_m/w should be only $\sim 1\%$ to ensure near-optimal performance.

For $w_m/w = 1.1\%$ in Table 4-2, $J_{sc} = 32.1 \text{ mA/cm}^2$ is near-maximum (99% collection efficiency) for the $25 \mu\text{m}$ cell with no internal photon reflection, and $V_{oc} = 662 \text{ mV}$ is now limited by dark current defined by nonmetal-surface recombination and Auger recombination in the n⁺/p⁺ regions. To gain insight on this limitation, we plot in Fig. 4-5 predicted V_{oc} versus S_b for varying N_s . We note that $S_b \sim 10^4 \text{ cm/s}$ for the assumed values of N_s , perhaps with x1/2 and x2 variations corresponding to the same variations

in N_s [17]. So, the implication of Fig. 4-5 is that S_b cannot be reduced enough, for a specific N_s , to yield a significant increase in V_{OC} , and that varying N_s to reduce the Auger recombination, via a tradeoff between the Auger lifetime and the carrier injection level [16], cannot yield much benefit either. Thus, the $w_m/w = 1.1\%$ (which is tantamount to 1-2%) cell in Table 4-2 seems to be near-optimal, at least for $w = w_n = w_p = 150\mu m$. We note also that predicted sensitivity to the expected t_{si} variations around $25\mu m$, due mainly to integrated- $g(x)$ variations, is not strong; J_{SC} varies between 31.4 and 32.6mA/cm^2 .

We now check effects of wider w_p and w_n , which may be needed in our simplified BC process. Actually w_p is the more critical parameter here, but we initially still assume $w_n = w_p$ as a basis for later checking n^+/p^+ region-width asymmetry in the ultimate BCSOM-cell design. The planned back-diffusion/metallization processing of our thin-Si BC cell is novel, and is much simpler than that used for thick BC cells in [30], provided w_p and w_n are sufficiently wide. The optimal BCSOM cell design, regarding processing as well as performance, thus will maximize w_p and w_n . The former is subject to the achievable L_n and, as we have found, parameters associated with the p^+ region; the latter is subject to the lateral majority-hole transport and ohmic losses in the p^- base. FLOODS simulations of the $w_m/w = 1.1\%$ cell in Table 4-2 for increasing w show that J_{SC} continually decreases. We plot in Fig.4-6 the decrease, normalized to the maximum possible AM1 J_{SC} for a $25\mu m$ cell without internal photon reflection, versus w_p ($= w_n =$

w). The dependence is nearly linear, clearly revealing the predominant loss, in the p^+ region, of minority electrons generated above the p^+ region.

The J_{SC} loss for increasing $w_p = w_n$ in Fig. 4-6 can be mitigated by using an asymmetric BC design with $w_n > w_p$, since virtually 100% of the electrons generated above the n^+ region are collected. Such mitigation is also indicated in Fig. 4-6 where we show, versus w_p , how the J_{SC} loss is reduced as w_n is increased relative to w_p . These simulation results depend, of course, on our FLOODS modeling of the heavy-doping effects in the p^+ region (with $N_s = 10^{20} \text{ cm}^{-3}$), which we believe is representative. So, the optimal BCSOM-cell design could be based on a tradeoff in Fig. 4-6 between a wider w_p needed for the BC process and the associated J_{SC} loss, and a wider w_n that must be limited because of fill-factor (FF) reduction due to lateral series resistance mainly in the p^- base, and possibly V_{OC} reduction due to added recombination in the wider n^+ region.

We believe that our simple BC process can be done with $w_p = 150 \mu\text{m}$. If so, then $w_n = w_p$ (with $w_m = 2-3 \mu\text{m}$) is viable, without significant loss of J_{SC} as indicated by the $w_m/w = 1.1\%$ cell in Table 4-2. However, a wider w_p may be needed to ensure the integrity of the process, possibly calling for $w_n > w_p$. For example, if $w_p = 300 \mu\text{m}$ is needed to be used (with $w_m = 3-6 \mu\text{m}$, which could yield less contact resistance), Fig. 4-6 suggests that using $w_n / w_p = 2-3$ would ameliorate the J_{SC} loss significantly. However, our simulations for such wider w_n also show FF reductions that offset the higher J_{SC} . (The corresponding V_{OC} reductions are not significant.) Thus, the asymmetric design is

not beneficial, and $w_n = w_p = 300\mu m$ would give the best BC process-performance tradeoff in this case. The FLOODS prediction of the overall performance of this wider cell is given in Table 4-3. Its efficiency ($\eta_{int} = 18.3\%$, $\eta = 17.4\%$) is a bit less than that of the near-optimal $w_p = w_n = 150\mu m$ cell in Table 4-2 (and also given in Table 4-3 for comparison) due to the reduced J_{SC} ($31.2\text{mA}/\text{cm}^2$) and some FF (0.821) reduction as well.

Further, we stress that the optimal BCSOM cell design yields good performance even for electron lifetimes much shorter than 1ms. We include in Table 4-3 the FLOODS predicted performance of the $w_n = w_p = 300\mu m$ cell with $\tau_n = 160\mu s$ ($L_n \cong 700\mu m$), which could be a more pragmatic lifetime dependent on N_B [33]. The efficiency ($\eta_{int} = 18.0\%$, $\eta = 17.1\%$) is comparable to that of the cell with long τ_n ! We also include in Table 4-3 the predicted τ_n -dependent performances for the near-minimum $w_p = w_n = 150\mu m$ allowed by the BCSOM process. For the narrower cells, the low- τ_n efficiency ($\eta_{int} = 18.9\%$, $\eta = 18.0\%$) is close to that for long τ_n ($\eta_{int} = 19.1\%$, $\eta = 18.1\%$) as well.

Our design optimization has led to narrow (2-3 μm) metal-contact line widths, which are doable in our simple BC process. We nonetheless note that wider w_m could be allowed (for example, to minimize contact resistance which we have neglected) and nearly the same cell performance could be achieved, provided the contact lines are replaced by strings of contact windows, optimally spaced in the z direction in Fig. 4-4 to keep the total contact area fixed (i.e., 1-2% of the n^+/p^+ -region area). The performance losses noted in Table 4-2 for wider w_m would be effectively offset by use of the contact

windows, but there could be a slight reduction of FF due to added ohmic drops in the n^+ / p^+ regions along the z direction.

4.4 Further Consideration of V_{OC}

The projected BCSOM cell performances in Table 4-3 are near-optimal, being limited significantly only by V_{OC} , or the pre-exponential current density [$J_0 = J_{SC} \exp(-qV_{OC}/k_B T)$] of the dark current-voltage characteristic; J_{SC} (without internal photon reflection) and FF are virtually maximum. Indeed, substantively higher V_{OC} was recently reported [7] by SunPower Corporation for their “generation-3” BC solar cell with thick $t_{Si} \cong 150\mu m$. A measured $V_{OC} = 721mV$ at AM1.5 ($100mW/cm^2$), corresponding to $J_{SC} = 40.5mA/cm^2$, was achieved. Normalizing this result back to AM1 ($92.5mW/cm^2$), which we have assumed, and factoring in the reduction of J_{SC} for thinner $t_{Si} \cong 25\mu m$ as implied by $g(x)$, we get $V_{OC} = 715mV$ for comparison with our predictions in Table 4-3. Comparing with the $V_{OC} = 662mV$ for the cell with $w = 150\mu m$ and $\tau_n = 1ms$ (which we will refer to as the “DUT”), we infer that our predicted J_0 is almost 8x higher than that of the SunPower cell. In this section we do more FLOODS simulations to identify the source(s) of the excess recombination in our optimal BCSOM cell, and thus, perhaps, to further optimize the design.

We first note, based on our previous simulations, that J_0 (or V_{OC}) in our DUT is not significantly affected by τ_n (see Table 4-3), S_b (see Fig. 4-5), w_m (see Table 4-2), nor S_f (see Table 4-1). We infer then that the Auger recombination in the n^+/p^+ regions is the predominant component in J_0 . Reducing w_p and w_n , and introducing a gap between the n^+ and p^+ regions, albeit via more complex BC processing, yields some

incremental V_{OC} increase due to less Auger recombination. However, J_{SC} then becomes quite sensitive to the back-surface recombination velocity in the gap and FF degrades due to lateral ohmic drops in the p^- base. Such a BC design is not a good tradeoff.

The key design parameter has to be the n^+/p^+ surface doping density N_s . Reducing N_s will increase the Auger carrier lifetime, tending to decrease J_0 , but will also increase the carrier injection level and render S_b more critical, tending to offset the J_0 reduction. The design tradeoff is best effected, as noted in [7], by using low N_s ($<10^{18} \text{cm}^{-3}$) in the nonmetal, surface-passivated areas (for minimal Auger recombination) and moderate N_s ($>10^{19} \text{cm}^{-3}$) in the metal areas (for minimal recombination at the very high-S ohmic contacts). Of course, this renders the processing more complex. We check a simpler process with a uniform, but lower, more optimal $N_s = 10^{19} \text{cm}^{-3}$ than we previously assumed. With $S_b = 1000 \text{cm/s}$ reduced accordingly [17], we now predict $V_{OC} = 677 \text{mV}$ for the DUT, still with $J_{SC} = 32.1 \text{mA/cm}^2$ as given in Table 4-4 ($w_m = 1.6 \mu\text{m}$). We have reduced J_0 by only a factor of $\cong 2$ by decreasing N_s by an order of magnitude, which suggests, in accord with [7], that recombination at the metal contacts is now important due to the transparency of the n^+/p^+ regions. We therefore thin w_m , and predict the V_{OC} increase given in Table 4-4, along with the modified DUT performance. For $w_m = 0.1 \mu\text{m}$ (only 0.07% metal-contact coverage), V_{OC} is increased to 694mV, reflecting another 2x reduction in J_0 . Further, $J_{SC} = 32.3 \text{mA/cm}^2$ is increased a bit, due to reduced loss in the p^+ region (related to Fig.

4-6). We note that the thin w_m in the modified DUT, with predicted $\eta_{int} = 20.1\%$ (versus 19.1% in Table 4-3) could be effected by point contacts in the z direction, as discussed previously.

At this point, J_0 in the DUT is $\cong 2.5x$ higher than that in the SunPower cell. We surmise, based on the insight we have given, that the main component now is recombination at the oxidized surfaces the n^+/p^+ regions, defined by S_b . Indeed, simulations confirm this; with S_b lowered to 10cm/s, we predict $V_{oc} = 713mV$, implying that J_0 is comparable to that of the SunPower cell. However, such a low S_b is seemingly not possible with $N_s = 10^{19}cm^{-3}$ [17], and so the ultimate V_{oc} , and cell efficiency, achieved by SunPower can be attributed to the noted optimization of the n^+/p^+ surface doping densities [7]. With simpler processing, our projected thin-Si BCSOM cell performance (in Table 4-4) is very good, but less than that of SunPower's cell due to lower J_{sc} (without internal photon reflection) as well as lower V_{oc} . Further, we stress that the optimal cell in Table 4-4 is not strongly dependent on τ_n , as we discussed with reference to Table 4-3.

4.5 Summary

We have overviewed a novel kerf-free SOM process [3] for making thin crystalline silicon wafers with thickness $\cong 25\mu m$, and have described a process for fabricating BC solar cells in the thin Si wafers (which we plan to simplify via a novel BC technique). We have set up FLOODS [8] for reliable physics-based 2-D numerical simulation of the BCSOM cells, and have used it to define the optimal design of the cells and to project their performance in AM1 sunlight. We predicted, without internal photon reflection, an

efficiency near 20%. With significant light trapping, which we intend to incorporate, we thus can project an ultimate efficiency near 24% as has been achieved with thick-Si BC cells [7]. These projections, augmented by preliminary experimental data that we presented, lead us to believe that our thin-Si BCSOM process can potentially yield a truly low-cost/watt, reliable silicon solar cell.

Table 4-1. FLOODS-predicted BC cell performance in AM1 (92.5mW/cm²) sunlight versus front-surface recombination velocity. Device thickness $t_{Si} = 25\mu m$, no FSF, $S_b = 10^4$ cm/s, $w_n = w_p = 150\mu m$, $w_{nn} = w_{mp} = 19.6\mu m$, no internal photon reflection. η was estimated from the predicted η_{int} by assuming a 5% ARC-associated loss.

S_f (cm/s)	J_{sc} (mA/cm ²)	V_{oc} (mV)	η_{int} (%)	η (%)
1	31.7	651	18.6	17.7
10	31.6	649	18.5	17.6
100	31.0	637	17.7	16.8
1000	26.3	595	13.9	13.2

Table 4-2. FLOODS-predicted performance of the $S_f=10$ cm/s BC cell in Table 4-1 versus fractional metal-contact coverage on the back n^+/p^+ regions. The results for $w_m/w = 1-2\%$, are near-optimal.

w_m/w (%)	J_{sc} (mA/cm ²)	V_{oc} (mV)	η_{int} (%)	η (%)
13.1	31.6	649	18.5	17.6
5.1	31.9	657	18.9	18.0
1.1	32.1	662	19.1	18.1
0.2	32.1	663	19.2	18.2

Table 4-3. FLOODS-predicted performances of the near-optimal 25 μm BC-cell design, with w ($w_n=w_p=300\mu\text{m}$) widened to trade-off BCSOM-process simplicity versus lifetime. With $w_m = 3.0\mu\text{m}$, $S_f = 10\text{cm/s}$, $S_b = 10^4\text{cm/s}$, $N_s = 10^{20}\text{cm}^{-3}$. The predicted performances for the near-minimum w ($= w_n = w_p = 150\mu\text{m}$), with $w_m = 1.6\mu\text{m}$ allowed by the BCSOM process are given as well.

w (μm)	τ_n (μs)	FF	J_{sc} (mA/cm^2)	V_{oc} (mV)	η_{int} (%)	η (%)
300	1000	0.821	31.2	661	18.3	17.4
300	160	0.817	31.0	658	18.0	17.1
150	1000	0.832	32.1	662	19.1	18.1
150	160	0.830	31.9	659	18.9	18.0

Table 4-4. FLOODS-predicted performance of the $w=150\mu\text{m}$ BCSOM cell in Table 4-3 with reduced $N_s=10^{19}\text{cm}^{-3}$ versus the metal-contact width. $\tau_n = 1\text{ms}$, $S_f = 10\text{cm/s}$, $S_b = 10^3\text{cm/s}$.

w_m (μm)	J_{sc} (mA/cm^2)	V_{oc} (mV)	FF	η_{int} (%)
1.60	32.1	677	0.832	19.6
0.38	32.2	686	0.831	19.9
0.18	32.3	691	0.831	20.0
0.10	32.3	694	0.830	20.1

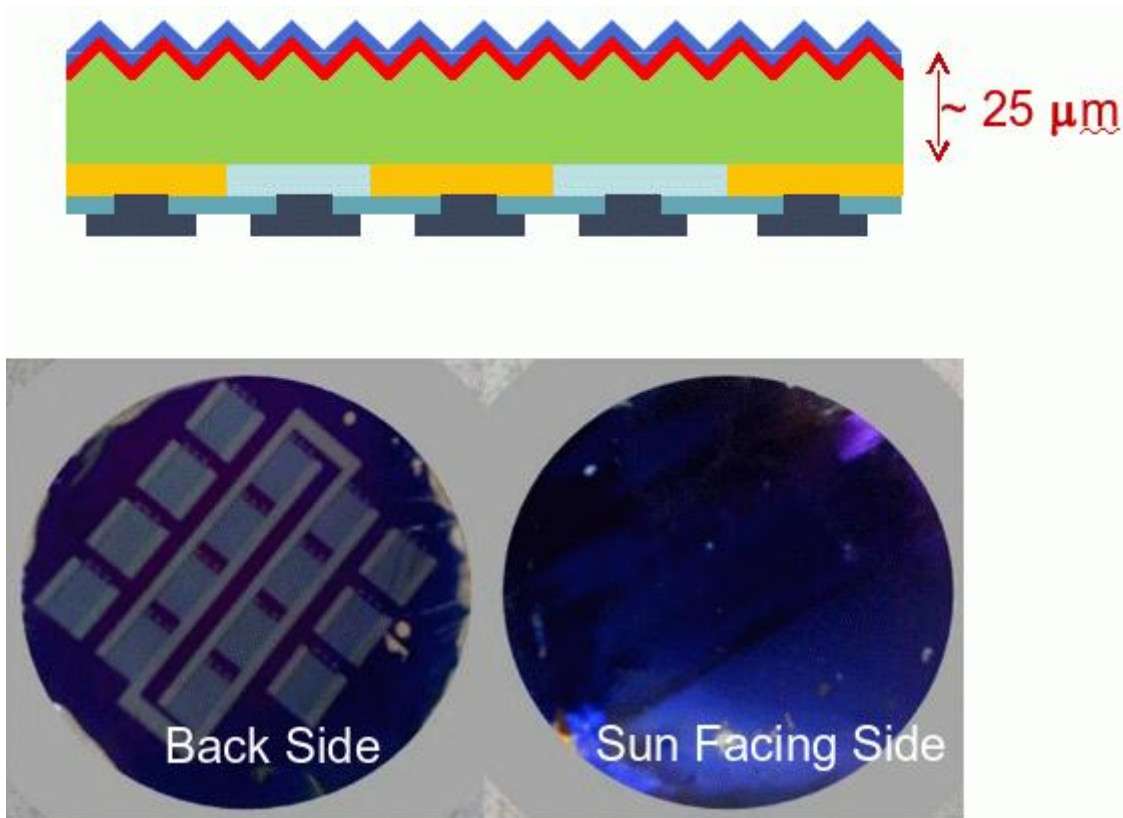


Figure 4-1. A fabricated thin ($t_{Si} \sim 25\mu\text{m}$) crystalline-silicon BCSOM solar cell. The cell was processed with backside n^+/p^+ diffusions, surface passivation, and metal, and front-side SOM defined texturing and ARC but without passivation (and no FSF). The back and front sides of the 3.5-inch flexible wafer are pictured, along with a schematic profile of the cell. Photo courtesy of Leo Mathew, AstroWatt Inc.

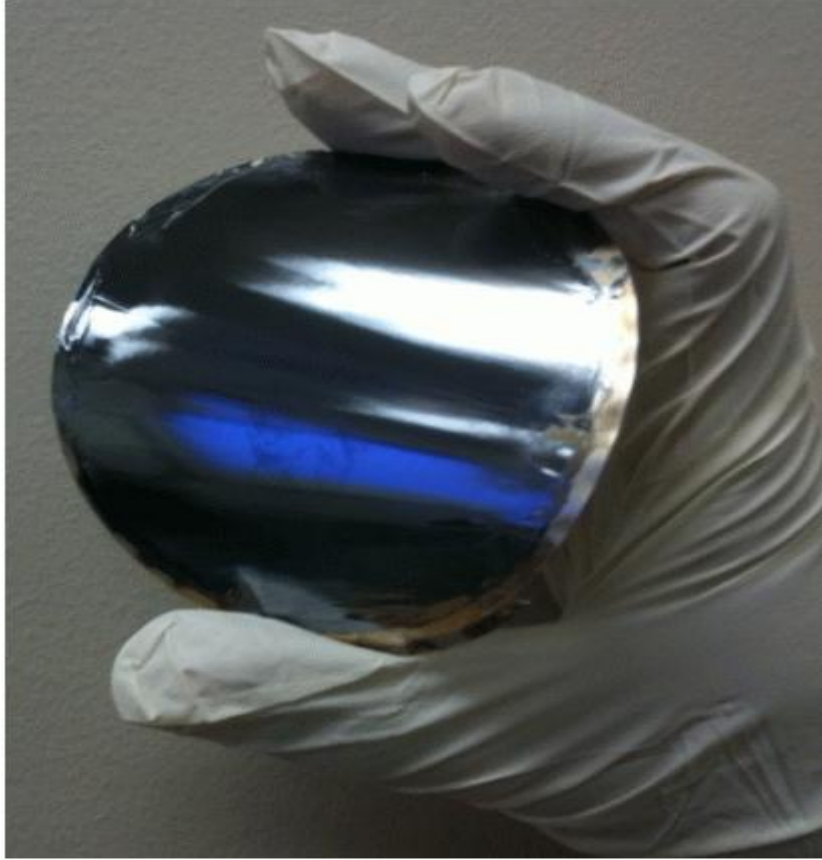


Figure 4-2. Demonstration of the flexibility of the SOM foil, which can broaden its possible applications. Photo courtesy of Leo Mathew, AstroWatt Inc.

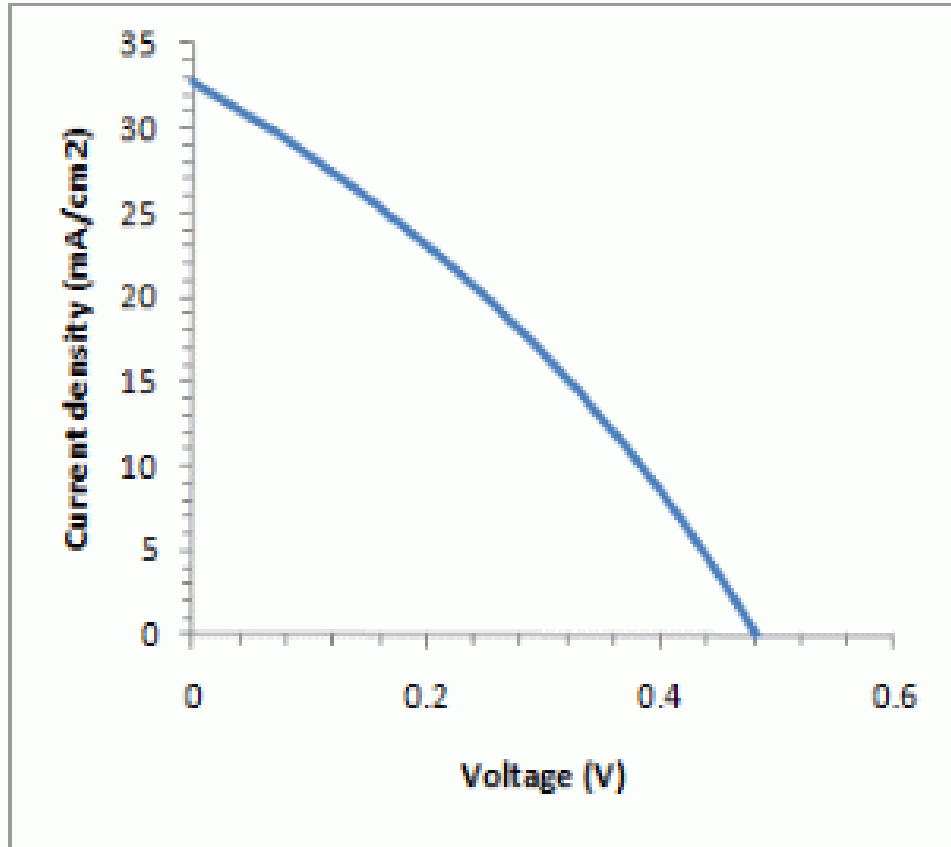


Figure 4-3. A measured 1-sun current-voltage characteristic of the BCSOM solar cell. Illumination level AM1.5G ($100\text{mW}/\text{cm}^2$), measured with back (metal)-side illumination and the current normalized to the unshaded area. The characteristic shows significant shunt conductance that yields an apparent V_{OC} less than the actual value of 620mV .

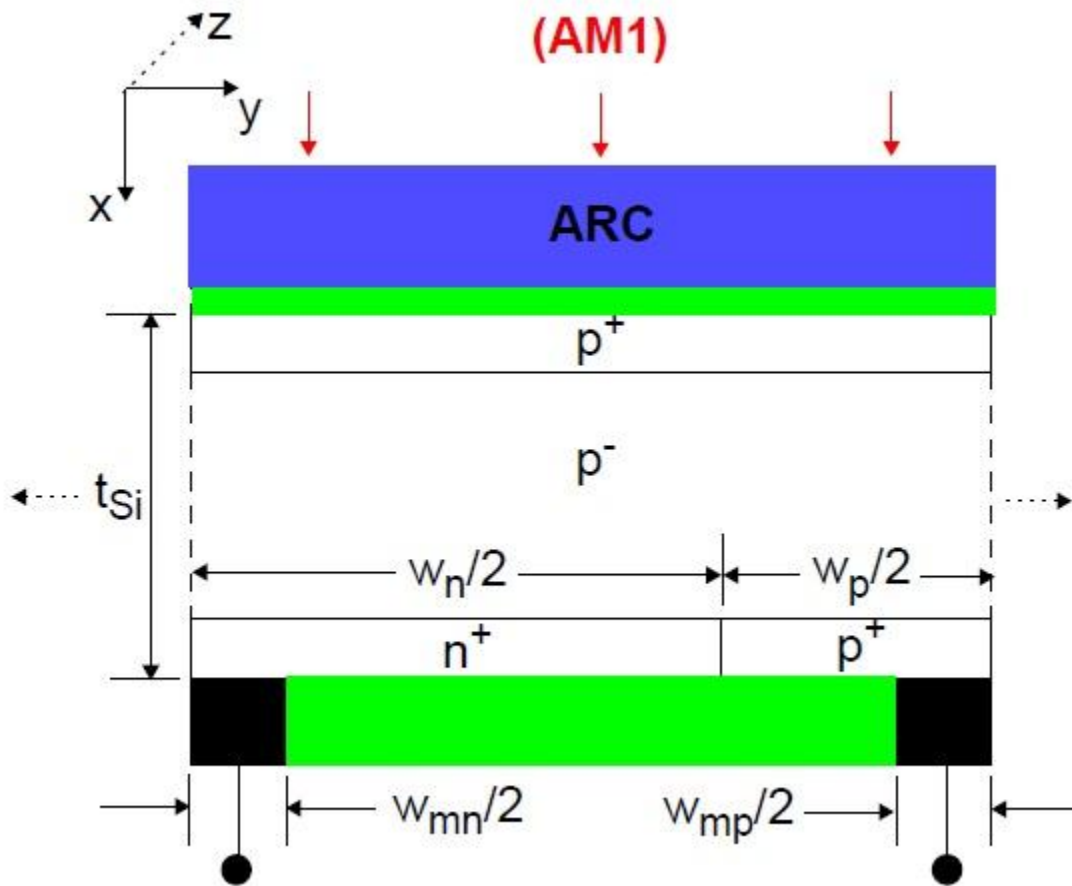


Figure 4-4. Basic cross-section of the BC solar cell structure, or the FLOODS domain assumed for the 2-D numerical simulations. The front p^+ (or n^+) region (FSF) is likely not needed in our thin-Si BC cells. The actual cell, with assumed interdigitated back n^+/p^+ regions and metal-contact lines (in z , possibly over spaced contact windows), would comprise repetitions (in y) of this basic structure, as indicated. Note that the metal lines, which can be much wider than the contact lines, are not part of the domain.

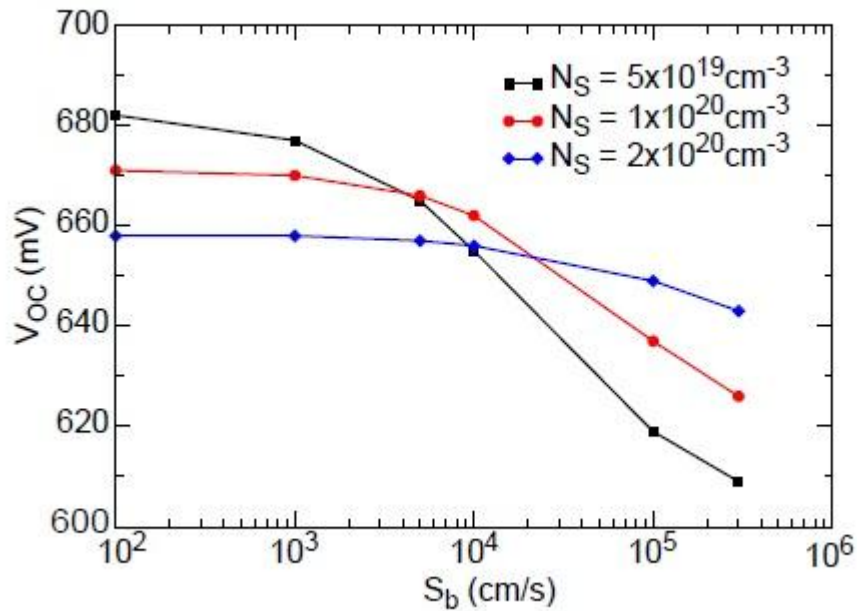


Figure 4-5. FLOODS-predicted open-circuit voltage versus the back nonmetal-surface recombination velocity for varying n^+/p^+ surface doping density. BC solar cell thickness is $25\mu\text{m}$ with near-optimal back metal-contact coverage ($w_m/w = 1.1\%$ with $w = w_n = w_p = 150\mu\text{m}$ with).

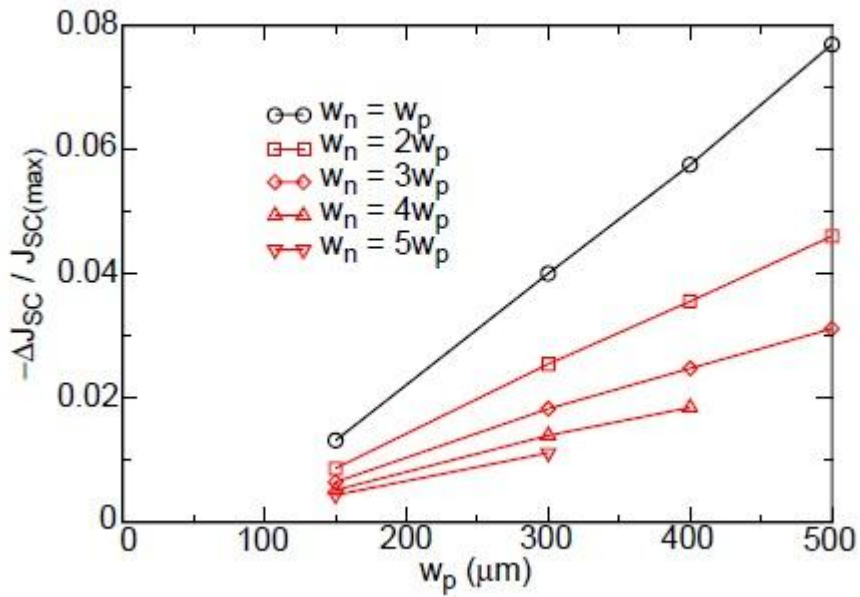


Figure 4-6. FLOODS-predicted loss of short-circuit current density versus increasing p⁺-region width, for different w_n/w_p ratios. Short-circuit current loss is normalized to the 25μm AM1 maximum ($J_{sc(max)} = 32.5\text{mA/cm}^2$).

CHAPTER 5 HETEROJUNCTION SOM SOLAR CELLS

As we have noted in previous chapters, increasing minority-carrier lifetime, minimizing the surface recombination velocity, and improving minority-carrier suppression at the front and back surfaces are essential in achieving better performance of solar cells. The latter two criteria are most important for thinner cells. These can be achieved by using doped hydrogenated amorphous silicon (a-Si:H) to form both the emitter and the back-surface field (BSF) of crystalline-Si solar cell. The resulting device structure is called silicon heterojunction (HJ) solar cell. Hydrogenated a-Si can achieve substantial surface passivation (SRV $\sim 10\text{cm/s}$) of c-Si interface and improve the minority-carrier suppression in the emitter and BSF regions significantly. Insertion of an intrinsic a-Si layer between the doped a-Si:H and c-Si interface further enhances the surface passivation quality of the heterojunction solar cell (Heterojunction with Intrinsic Thin layer or HIT [13], [39], [40]). Moreover, a-Si:H deposition is a simple, low-temperature, and inexpensive process technology. Hence, the minority-carrier lifetime degradation during fabrication steps is minimized. Sanyo has reported an efficiency of 23.0% on their champion HIT cells [37]. Thus, a-Si:H/c-Si heterojunction solar cells fabricated on thin semiconductor-on-metal (SOM) foils, have the potential of achieving very high-efficiency solar cells and reducing cost [39], [40].

The main challenges in achieving such efficient HJ solar cells on thin SOM substrates are to improve the passivation capability of a-Si:H/c-Si interface, to clean SOM substrates prior to a-Si:H deposition to remove contaminants from the surface, to reduce the resistive and optical absorption losses in a-Si:H and transparent conducting oxide (TCO), to control thicknesses of intrinsic and doped a-Si:H layers, to suppress of

epitaxial growth at the hetero-interface, to incorporate surface texture, and to design optimum front grids.

For the first time, a remote-plasma chemical vapor deposition (RPCVD)-based crystalline-silicon heterojunction solar cell process was developed on a novel thin semiconductor-on-metal (SOM) substrate. Thin crystalline silicon (c-Si) is required to attain substantial cost reduction and fabricate higher efficiency cells. Hydrogenated amorphous silicon (a-Si:H) films are best suited to form low-temperature heterojunctions on thin crystalline-silicon materials. As the silicon thickness decreases, the surface passivation quality dictates the performance of these cells. In RPCVD systems, deposition temperature, deposition rate, and the distance of the sample from the plasma source can be varied to minimize the surface damage from ion bombardment, and enhance passivation quality.

Heterojunction cells without intrinsic a-Si:H layers were fabricated to stress the potential of achieving reduced plasma damage to the c-Si surface and improved passivation with RPCVD. Two device architectures were fabricated on 25 μm c-Si SOM foils: 1) a single-side heterojunction (SHJ) cell, and 2) a double-side heterojunction (DHJ) cell. An efficiency of 13.4% with highest open-circuit voltage of 662mV was measured on a device. Losses in these devices were identified, and the optimum SHJ cell device structure was designed and performance predicted with numerical simulations. These results suggest that RPCVD is a potential alternative technology to achieve high-efficiency heterojunction solar cells.

The chapter begins with a brief background and physical insights on minority-carrier suppression in doped a-Si:H emitter. The SOM exfoliation process flow to

produce thin ($\sim 25\mu\text{m}$) crystalline-Si is described. Transparent conducting oxide (TCO) is a critical layer deposited on top of doped a-Si:H film to enhance the lateral conduction of minority-carriers. Indium tin oxide (ITO) is an excellent TCO for silicon HJ solar cells and the ITO process development is described. Subsequently, a-Si:H process development using RPCVD system is described and the systematic optimization of the process parameters, e.g. sample-to-plasma distance, deposition temperature, and deposition time (i.e. a-Si:H film thickness) is described. Raman spectroscopy, TEM cross-sections, and Suns-Voc measurements were performed to characterize the deposited a-Si:H films. Fabrication of single- and double-side HJ cell is described. Dark and light JV and external quantum efficiency (EQE) characteristics of the fabricated HJ solar cells were measured and key losses in the devices were understood. Finally, optimum efficiency of HJ cells fabricated on thin SOM substrates, based on FLOODS simulations, is projected.

5.1 Background

Recombination of minority carriers at the cell surfaces and metal contacts, and in the emitter region can be minimized by reducing the minority-carrier concentration. This can be achieved by replacing the diffused emitter with a thin, doped wide bandgap material such as hydrogenated a-Si:H ($E_g \sim 1.67\text{eV}$). The a-Si:H/c-Si heterojunction solar cell was first demonstrated in 1977 and later developed and commercialized by Sanyo Electric Co. as HIT (Heterojunction with Intrinsic Thin layer) solar cells [37]. In addition, the thin intrinsic amorphous silicon layer (i-layer) deposited at low-temperature enhances the surface passivation by terminating the dangling bonds at the crystalline-Si interface. The conversion efficiency of the HIT solar cell has been increased to 23.0% at a research level [37]. Fig. 5-1 shows the schematic cross-section of a typical double-

side HJ (DHJ) solar cell with both the emitter and BSF regions formed by doped a-Si:H layers. A cross-section of HIT structure is also shown in the same figure.

For a pn-homojunction diode, the suppression of minority carriers (electrons) in the p⁺ emitter depends on the doping densities of the emitter and base. In dark, the electron current injected into the p⁺ c-Si emitter from the n-type base at maximum power-point forward bias (V_{MPP}) can be modeled as mentioned in Chapter 3:

$$J_n = \frac{qn_{ie}^2 \bar{D}_n}{N_{G(p^+)}} \exp\left(\frac{qV_{MPP}}{k_B T}\right) \quad (5-1)$$

where n_{ie}^2 is an effective intrinsic carrier density defined in Chapter 2, \bar{D}_n is the average electron diffusivity in the emitter and $N_{G(p^+)}$ is the Gummel number of front emitter, and V_{MPP} is the maximum power-point forward voltage. From Chapter 2, n_{ie}^2 is defined as:

$$n_{ie}^2 = n_i^2 \exp\left(\frac{\Delta E_g}{k_B T}\right) \left[\frac{F_{1/2}(\eta_c)}{\exp(\eta_c)} \right] \quad (5-2)$$

where n_i is the intrinsic carrier concentration in c-Si, ΔE_g is the bandgap narrowing in c-Si, and $F_{1/2}(\eta_c)$ is the F-D integral of order 1/2 with $\eta_c \equiv (E_F - E_C)/k_B T$. The intrinsic carrier concentration, n_i , is given by [36]:

$$n_i = \sqrt{N_c N_v} \exp\left(\frac{-E_g}{2k_B T}\right) \quad (5-3)$$

where N_c and N_v are the effective densities of states in the conduction and valence bands, respectively, and E_g is the c-Si bandgap. From Eq. (5-2) and (5-3),

$$n_{ie}^2 = N_c N_v \exp\left(\frac{-E_g + \Delta E_g}{k_B T}\right) \exp\left(\frac{F_{1/2}(\eta_c)}{\exp(\eta_c)}\right). \quad (5-4)$$

The electron current injected into the p⁺ c-Si emitter can hence be written as

$$J_n \propto \frac{\overline{D}_n}{N_{G(p^+)}} \cdot \exp\left(\frac{-E_g + \Delta E_g}{k_B T}\right) \cdot \exp\left(\frac{F_{1/2}(\eta_c)}{\exp(\eta_c)}\right). \quad (5-5)$$

For simplicity, we assume negligible bandgap narrowing and the p^+ doping level is such that the hole Fermi-level is few $k_B T/q$ away from the valence band edge so that we can ignore majority-carrier degeneracy. Thus dark electron current density in p^+ emitter can be written as

$$J_n \propto \frac{\overline{D}_n}{N_{G(p^+)}} \cdot \exp\left(\frac{-E_g}{k_B T}\right) \cdot \exp\left(\frac{qV_{MPP}}{k_B T}\right). \quad (5-6)$$

Similarly for an a-Si:H(p^+)/c-Si(n) heterojunction diode, the dark electron current density due to the injection of minority electrons into the p^+ a-Si:H emitter from n-type crystalline-Si base (assuming proper tunneling of electrons through the hetero-interface, and neglecting heavy doping effects of p^+ a-Si:H layer) at maximum power-point forward bias can be assumed as

$$J_{n(a-Si)} \propto \frac{\overline{D}_n}{N_{G(p^+)}} \cdot \exp\left(\frac{-E_{g(a-Si)}}{k_B T}\right) \cdot \exp\left(\frac{qV_{MPP}}{k_B T}\right) \quad (5-7)$$

where $E_{g(a-Si)}$ is the bandgap of the a-Si(p^+) emitter. At 300K the bandgap of a-Si:H (doped) is about 1.67 eV [14] and the bandgap of crystalline Si is about 1.12eV.

Similarly, minority-hole current density into the c-Si(n) base due to the hole injection from a-Si:H(p^+) emitter can be written as

$$J_{p(c-Si)} \propto \frac{\overline{D}_p}{N_{G(p^+)}} \cdot \exp\left(\frac{-E_{g(c-Si)}}{k_B T}\right) \cdot \exp\left(\frac{qV_{MPP}}{k_B T}\right). \quad (5-8)$$

Hence, the ratio of emitter current to the base current can be written as

$$\frac{J_{n(a-Si)}}{J_{p(c-Si)}} \sim \frac{\overline{D}_n \cdot N_{G(p^+)}}{\overline{D}_p \cdot N_{G(n^+)}} \cdot \exp\left(\frac{-(E_{g(a-Si)} - E_{g(c-Si)})}{k_B T}\right). \quad (5-9)$$

So, in an a-Si:H(p⁺)/c-Si(n) heterojunction diode, suppression of minority-carrier concentration in the a-Si:H emitter depends not only on the emitter doping density ($N_{G(p^+)}$) but also on the bandgap difference of amorphous-Si and crystalline-Si. Both of these two parameters (heavier emitter doping density and wider bandgap of a-Si:H) enhances passivation quality of emitter by suppressing minority-carrier concentration. In case of a homojunction pn diode, the suppression of minority-carrier concentration depends only on the ratio of the emitter to base doping densities. However, extremely low lifetime of minority-carrier in a-Si emitter, absorption of photons in a-Si emitter and minority-carrier transport (tunneling) across the hetero-interface dictates the a-Si:H thickness and hence, the HJ solar cell performance. Introduction of an intrinsic a-Si:H layer further improves surface passivation of c-Si interface and improves the tunneling of holes across the HJ.

For simplicity and first-order analysis, carrier mobility differences in the emitter and base can be neglected, and total integrated emitter and base doping densities can be assumed equal. For this simple case, the ratio of emitter current to the base current can be written as

$$\frac{J_{n(a-Si)}}{J_{p(c-Si)}} \sim \exp\left(\frac{-(1.67 - 1.12)}{0.026}\right) \approx 10^{-10}. \quad (5-10)$$

We see the electron injection level into the a-Si (p⁺) emitter is almost 10 orders of magnitude lower than that into the c-Si(n) base for same doping densities. However, the

hole current density ($J_{p(c-Si)}$) injected in to the base is high, as defined by the recombination profile in the base, BSF region, and at the back contact and surface. Thus understanding the recombination mechanism in the base, BSF and back-surface is very critical and should be reduced by clever designs such as local BSF/local contacts that we have discussed in detail in Chapter 2 and Chapter 3. The a-Si:H/c-Si HJ solar cells on thin SOM substrates have potential of higher V_{OC} due to minority-carrier suppression in the a-Si:H emitter compared to a conventional c-Si based solar cell with emitter fabricated by thermal diffusion.

5.2 Exfoliation Process

A kerf-free Semiconductor on Metal (SOM) exfoliation process [3], [15] was developed to produce $\sim 25\mu\text{m}$ thin crystalline silicon foils from a parent wafer. The process flow for exfoliation and fabrication of heterojunction cells is shown in Fig. 5-2. As shown in the figure, an exfoliated Si cell fabrication process begins by pre-forming n^+/n high-low junction by POCl_3 or spin-on-diffusion on the starting wafer followed by silicon nitride (Si_3N_4) passivation, and seed metal film stack deposition. A metal film is then deposited over the seed layer using an electrochemical deposition process. During this process hydrogen is incorporated from the electroplating bath into the underlying substrate as shown in the SIMS data in Fig. 5-3, which is then diffused into the substrate using an optimized heat treatment. Coefficients of thermal expansion (CTE) are different between Si and metal film. During the heat treatment or annealing process, internal stresses are created due to the thermal expansion mismatch stresses between the deposited metal film and the underlying Si substrate. The thermal expansion mismatch stresses results in exfoliation of a thin crystalline-Si layer from the parent wafer. The exfoliation is aided and controlled to the required depth using a proprietary

Si exfoliation tool. A mechanical wedge is used which creates a fracture along a sub-surface plane of the substrate. The thickness of the exfoliated layer is controlled by varying the electroplated metal thickness, the annealing, and the mechanical wedge parameters.

With this technology, we have recently engineered the deposited metal and the thermal treatment to obtain 25-30 μm thin exfoliated foils from an 8-inch diameter 775 μm thick monocrystalline wafer, as shown in Fig. 5-4. Scaling the exfoliation process to 8-inch diameter wafers enables industry standard 125mm x 125mm pseudo-square cells to be fabricated from the exfoliated foils. As seen in the figure, the exfoliated foil has a curl associated with it due to the thermal expansion mismatch between the metal and the Si. However, the exfoliated foil is flexible due to the low thickness of Si used and is rugged and easy-to-handle due to the metal backing. Therefore, the foil can be mounted flat by mechanical clamps or vacuum during processing.

5.3 Indium Tin Oxide Process Development

In silicon heterojunction solar cells, low-resistance lateral conduction through the a-Si:H emitter is not possible. Hence, a transparent conducting oxide (TCO) layer is required to transport carriers laterally to the metallic front contact grid. Indium tin oxide (ITO) film is a degenerately doped n-type semiconductor and has a high optical transmittance and a low electrical resistivity. Therefore, ITO is used as a transparent conducting oxide in a-Si:H/c-Si heterojunction solar cells. In this study, ITO films were deposited by an R.F. magnetron sputtering process. We investigated the effects of substrate temperature and Ar pressure on electrical and optical properties of ITO films. At first, the ITO process was developed on glass substrates and then the optimized process was used for HJ device fabrication.

The ITO films were deposited on Corning glass slides by Kurt J. Lesker R.F. magnetron sputtering tool using a 3-inch diameter ITO target with a purity of 99.99% and with weight percentage of 90 to 10 for In_2O_3 and SnO_2 , respectively. The target was bonded to a copper backing plate for cooling and protecting from fractures. The target-to-substrate distance was kept at the same optimum value for each deposition. High purity Ar gas was introduced as sputtering gas and deposition pressure was controlled as a process parameter. The films were deposited without any oxygen gas into the deposition chamber due to the limitation of the sputtering system. The substrate holder was heated by halogen lamps and the temperature was monitored as a process control parameter. 13.56MHz R.F. power (100W) was introduced through an automatic matching network to minimize the reflected power.

The base pressure of the sputtering chamber was in the low 10^{-7} Torr. Prior to transferring into load lock chamber, the glass substrates were degreased in acetone/IPA solution in an ultrasonic bath, 5-cycle rinsed in DI water, and then blow-dried in N_2 gas. Prior to each deposition, a pre-sputter etching of the target was carried out with shutter closed for 30 minutes. Deposited ITO film thicknesses were $\sim 70\text{nm}$ and $\sim 80\text{nm}$. The thicknesses of the films were measured by surface profilometry. The sheet resistance and optical transmittance of the films were measured by four-point probe and Thermo Scientific UV-Visible spectrophotometer, respectively. At first, we optimized our process for low substrate temperature ($\sim 200^\circ\text{C}$), and then we carried out deposition pressure optimization to obtain low sheet resistance and high optical transmittance for our ITO films.

The measured sheet resistances of the deposited ITO films (~70nm- and ~80nm-thick) for different substrate temperatures (20°C - 230°C) are shown in Fig. 5-5. The films were deposited at an Ar pressure of 10mTorr and R.F. power of 100W. It is observed that as the substrate temperature is increased, sheet resistance decreases. The decrease in sheet resistance is probably due to the increase in oxygen vacancies with increase in substrate temperature [49]. For ITO film deposited at 20°C, the optical transmittance is low in short- and long- wavelength ranges as seen from Fig. 5-6. For purposes of comparison, the transmittance of the glass substrate without an ITO coating is also shown in Fig. 5-6. The optical transmittances are almost identical for films deposited at 200°C and 230°C for longer wavelength with a slight increase in transmittance in shorter wavelengths (UV - Visual) for 230°C-deposited film. It is important to note, that as the thickness of the film is increased, the sheet resistance decreases but on the other hand, optical transmittance decreases for a particular deposition temperature and Ar pressure. In this study, we optimized our ITO process for a film thickness of 70nm and substrate temperature of 200°C. A low-temperature ($\leq 200^\circ\text{C}$) ITO process development was essential for our HJ solar cell fabrication process, as we discuss it later in this chapter.

We then studied the effect of deposition pressure (i.e. Ar pressure) on sheet resistance and optical transmittance of the ITO films. The deposition pressure was varied from 10mTorr to 5mTorr, and Fig. 5-7 shows the dependence of sheet resistance on deposition pressure. The substrate temperature was kept at constant 200°C and ITO thickness was ~70nm for this experiment. It is observed that sheet resistance of the films decreases with decreased deposition pressure and at 5mTorr Ar pressure, the

sheet resistance of the film is $\sim 56\Omega/\text{sq}$. Lower sheet resistance of the film deposited at lower pressure indicates increased carrier mobility in films deposited at lower Ar pressure [51], since the electron concentrations remains almost the same at different deposition pressures.

The optical transmittance characteristics are shown in Fig. 5-8. For purposes of comparison, the transmittance of the glass substrate without an ITO coating is also plotted in the same figure. The variation of the optical transmittance in the longer wavelength regions (near-IR region) indicates the variation of the electron concentration in the ITO films [49] – [51]. The optical transmittances in the longer wavelength region for ITO films deposited at different Ar pressures do not show much difference. This reflects that the electron concentrations in the films deposited at different Ar pressures are almost the same. The variation in optical transmittances in shorter wavelengths (UV-Visual) indicates variations in optical bandgap of ITO film. The increase in short-wavelength optical transmittance of ITO films deposited at lower Ar pressure suggests widening of optical bandgap of ITO [49], [51]. The ITO film deposited at 200°C and 5mTorr Ar pressure has an average optical transmittance of $\sim 84\%$ and sheet resistance of $\sim 56\Omega/\text{sq}$ for a thickness of $\sim 70\text{nm}$. This process is used for subsequent TCO layer deposition during a-Si:H/c-Si HJ solar cell fabrication.

5.4 Overview of Remote-Plasma Chemical Vapor Deposition System

RPCVD is a promising low-temperature ($\sim 200^\circ\text{C}$) technology for a-Si film deposition with lower plasma damage than conventional Plasma-Enhanced Chemical Vapor Deposition (PECVD). In RPCVD system, during the deposition process there is no direct exposure of the sample to the plasma as the sample is not immersed in the plasma. Instead, the sample is held downstream from the glow discharge. This can

reduce the damage to the silicon surface from energetic particles in the plasma and improve passivation quality. The RPCVD system uses ultra-high vacuum (UHV) and the plasma is remote from the sample. Both of these features can contribute to improved passivation; hence, in this study a majority of the cells have been fabricated without the intrinsic amorphous Si:H (i-layer) passivation as used in typical heterojunction cells. Single-side and double-side silicon heterojunction cells were fabricated. Potential of improving surface passivation using intrinsic a-Si:H is shown.

The optimal distance of the wafers from the plasma source and the temperature can be varied to obtain best passivation of c-Si surface. This process with optimum sample-to-plasma distance and temperature can be transferred to SOM foils to form heterojunction for solar cells. A schematic of the deposition chamber for the RPCVD system [38] is shown in Fig. 5-9.

5.5 RPCVD Process Development and Cell Fabrication

After the exfoliation process was carried out, RPCVD technology was used to fabricate the cells on these SOM foils. The RPCVD tool was first used to develop the highest possible Suns-Voc on silicon substrates that were 500 μ m thick. The optimal distance of the wafers from the plasma source and the temperature were evaluated. These conditions were then used to deposit a stack of p⁺ a-Si:H films on the SOM foils.

We fabricated solar cells with front heterojunction and back-surface field (BSF) using the 25 μ m c-Si foils that were exfoliated from (100) monocrystalline CZ 10-20 ohm-cm n-type Si wafers. As shown in Fig. 5-2, the single-side heterojunction (SHJ) cell fabrication process begins with forming a uniform diffused n⁺ c-Si junction as BSF on the starting wafer using POCl₃ diffusion. Subsequently, a nitride passivation layer was formed over the wafer surface, and it was patterned non-lithographically [15] to open

contact holes to the n^+ diffusion. A metal film was then deposited electrochemically over the wafer and the exfoliation process was carried out. This metal film serves some key roles in our process: (a) it provides the mismatch stresses needed for exfoliation, (b) it serves as a backside contact to the cell and (c) it provides mechanical support to enable handling of the exfoliated Si during subsequent processing. After exfoliation cell fabrication is completed by deposition of a heterojunction stack and Transparent Conducting Oxide (TCO) film followed by silver screen printing. For the study of optimal distance of the samples from the plasma source and the temperature, the cells were completed without nitride passivation on the back surface and thermal evaporation of aluminum was used to form back metal electrodes.

Prior to RPCVD a-Si deposition, the exfoliated Si SOM foils were degreased in an ultrasonic bath of acetone and isopropyl alcohol, followed by 5-cycle DI water rinse, piranha, and 5-cycle DI water rinse to remove the residual organic contaminants. Samples were then immersed in a dilute HF solution to remove the native oxide and to leave the surface hydrogen terminated. Finally, samples were blow-dried with nitrogen and immediately transferred into the RPCVD system. Argon plasma was inductively excited with ~7W of RF power (13.56 MHz). For a typical p^+ a-Si:H layer deposition process, the base pressure was in the low 10^{-9} Torr range, 200°C temperature, and 30mTorr deposition pressure, and pure SiH_4 and 100ppm $\text{B}_2\text{H}_6/\text{H}_2$ mixture were introduced as source gases. Intrinsic a-Si:H layer was deposited at 150°C. Amorphous Si films were deposited on 136nm-thick thermally grown oxide on Si control wafers to measure a-Si:H film thickness by spectroscopic ellipsometry and to carry out Raman spectroscopy. Solar cells were completed by deposition of ~ 80nm-thick indium tin oxide

(ITO) as an anti-reflection coating (ARC) and transparent front conductive layer in an RF magnetron sputtering system at 200°C, followed by screen-printed silver grid lines to complete the front electrodes. Fig. 5-10(a) shows a photograph of completed 1.1cm² area heterojunction cells fabricated on a 25µm-thick flexible SOM foil.

We also fabricated dual-side heterojunction cells using the thin exfoliated foils. For a dual-side heterojunction cell process, steps (b) and (c) in Fig. 5-2 were replaced with deposition of a heterojunction a-Si film stack (intrinsic and doped layers) on a starting wafer followed by deposition of an ITO film. Formation of back intrinsic/n⁺ a-Si:H stack in double-side heterojunction cells was carried out in an industrial PECVD system, while formation of front p⁺ a-Si:H stack for front emitter was carried out in RPCVD system. The rest of the processes including exfoliation and front side heterojunction deposition were identical in both process flows. Thus, all processing after exfoliation was carried out at temperatures below 200°C. Cells were fabricated both with and without the intrinsic amorphous Si layer in the heterojunction stack. Table 5-1 shows the overview of device structures studied in this work with corresponding device performances. As seen from the table that the performance of a HJ cell depends on thickness of doped a-Si:H layer, type of BSF (diffused for single-side HJ cell or doped a-Si:H for double-side HJ cell), and incorporation of intrinsic a-Si:H layer.

5.6 RPCVD Process Optimization

First, a-Si:H(p⁺)/c-Si(n) heterojunction cells without intrinsic a-Si:H layer were formed on 500µm-thick wafers to characterize the effective passivation quality of a-Si:H film and to optimize the emitter for the front of the single-heterojunction cell (Fig. 5-10(b)) in terms of Suns-Voc. Table 5-2 shows the optimal conditions depend on sample temperature and distance of samples from plasma source. In order to understand the

variation of the RPCVD layer across the wafer, four different cells were formed on 2-square-inch samples. These 2-square-inch samples were diced from larger wafers and from larger SOM foils due to limits of the RPCVD chamber size (Fig. 5-10(a)). The data across these four cells suggest that an optimal distance from the plasma source exists. When the wafers were farther away or closer than this optimal distance, the V_{OC} of the cells were degraded or varied substantially for an optimal temperature.

In addition, Raman spectroscopy of the p-doped a-Si:H layers at different deposition temperatures was used to characterize the crystallinity of the films (Fig. 5-11). The characteristic amorphous Si Gaussian peak ($\sim 480\text{cm}^{-1}$) shifts to the right with increasing temperature, making the film more microcrystalline. Therefore, p-doped a-Si:H was deposited at 200°C . Effect of introducing hydrogen was analyzed and preliminary studies showed that with the introduction of hydrogen, the films become more microcrystalline at a particular temperature. Based on this analysis and the Suns-Voc results shown in Table 5-2, sample N2-4 showed the least variation, best surface passivation as evident from the highest Suns-Voc numbers [39]–[41], and thus its process was used to fabricate cells on the thin crystalline SOM foils.

Fig. 5-12 shows a high resolution TEM cross section of a completed cell. As can be seen, the exfoliated Si is completely monocrystalline. Further, the interface between the deposited amorphous Si layers and the exfoliated Si is clean and sharp, showing no epitaxial growth of the deposited layers.

5.7 Single-Side Heterojunction Cell

Fig. 5-13 shows the JV characteristics and external quantum efficiencies (EQE) of a-Si:H(p^+)/c-Si(n) single-side heterojunction cells (SHJ) fabricated on thin exfoliated SOM foil as measured under AM1.5G illumination. These cells have no intrinsic a-Si:H-

layer passivation, with a uniform n^+ diffusion (surface doping concentration, $N_S=1 \times 10^{20} \text{cm}^{-3}$ and junction depth $x_j=0.5 \mu\text{m}$) as back-surface field (BSF) and non-optimized local back contact (Fig. 5-10(b)). The cell 41-04-1 had $V_{OC}=605 \text{mV}$, $J_{SC}=29.6 \text{mA/cm}^2$, $FF=62.8$, $\eta=11.2\%$. The cell area was 1.1cm^2 and shadowing from front metal grid was measured $\sim 11.5\%$. Since mid-and-long wavelength EQE of both devices are almost identical, the improvement in J_{SC} by 0.8mA/cm^2 in sample 41-05-1 from sample 41-04-1 is due to less optical absorption in thinner a-Si:H(p^+) layer [40], [41]. Thicker p^+ -layer seems to improve V_{OC} by improving surface passivation, but the cell performance is offset by decrease in J_{SC} with increasing a-Si:H(p^+) layer thickness.

FLOODS [8], [42] simulation was used to determine the performance limiting factors in these single-side heterojunction cells (SHJ). V_{OC} in sample 41-04-1 is limited by excessive band-to-band Auger carrier recombination in the heavily doped back n^+ diffusion region. The overlap of EQE and relatively lower quantum efficiency in the long wavelength region for both samples suggest that excessive recombination of photo-generated carriers is taking place in the heavily doped n^+ diffusion region. Thus both V_{OC} and J_{SC} can be improved by incorporating an optimum doping density for the n^+ BSF region. For bulk Si resistivity of $1-10 \Omega\text{-cm}$, the optimal n^+ diffusion is found to be a profile with $N_S=10^{19} \text{cm}^{-3}$ and $x_j=0.3-0.5 \mu\text{m}$. For thinner cells, the minority-carrier diffusion length is usually longer than cell thickness ($\sim 25 \mu\text{m}$) and hence, design optimization of the BSF and back metal contact is important. At this optimum doping density for n^+ diffusion, recombination at the back metal contact and back surface is now important due to the transparency of the n^+ region [16], [34], [35], [43]. Hence, we propose a device architecture based on local back doping and local back contact with

better surface passivation for thinner (sub-30 μm) SOM based single-side heterojunction cell similar to the PERL cell architecture [43], [44] as shown in Fig. 5-14. Moreover, V_{OC} and J_{SC} can be improved further by incorporating an intrinsic a-Si:H-layer [39].

Two thin single heterojunction SOM solar cells with different back side contact schemes were studied. Sample 07-B had uniform n^+ diffusion as BSF, uniform back metal coverage and no nitride passivation at back, and Sample 36-10 had uniform n^+ diffusion as BSF, local back contact (non-optimized) and nitride passivation at back. The a-Si:H(p^+)/c-Si stack was identical for both cells as evident from the overlap of EQE at shorter wavelengths as seen in Fig. 5-15. Relatively lower quantum efficiency at mid-to-longer wavelength range in sample 07-B is due to additional recombination in at the back metal contact. Local back contact and back passivation significantly improve device performance at longer wavelengths (as seen from higher J_{SC} in 36-10) and reduce recombination at back contact (as seen from higher V_{OC} in 36-10).

We performed numerical simulation in FLOODS to project performance of single-side heterojunction cell with local back doping and local back contact scheme. We assumed ohmic back contact (with recombination velocity $S=10^6\text{cm/s}$ at the back contacts), base donor doping density $N_B=10^{16}\text{cm}^{-3}$, and local n^+ diffusion in contact areas was a Gaussian doping profile with $N_S=3\times 10^{20}\text{cm}^{-3}$, $x_j=0.3\mu\text{m}$, and back metal coverage of 1% with 600 μm contact spacing (pitch). Back contact areas were assumed to be heavily doped to reduce recombination at these contact areas by suppressing minority-carrier concentration in these areas [16], [24], [25]. Surface recombination velocities at the non-metal front and back surfaces are assumed to be 10cm/s, which we think is achievable [17] by thermal oxide passivation at the back surface and

improved a-Si:H passivation by RPCVD at the front surface [13], [40]. Device thickness was varied with minority-carrier lifetime in the bulk as a parameter to project the cell performance. Fig. 5-16 shows the simulated intrinsic device performance of the suggested device under AM1.5G solar spectrum. For thin cells ($t_{Si} \leq 40 \mu\text{m}$), J_{SC} has negligible sensitivity to the minority-carrier lifetime which relaxes the requirement for the more expensive high lifetime substrates. V_{OC} increases with decreasing substrate thickness due to a decrease in the bulk recombination. For realistic 7% loss due to front electrode shading and front surface reflectance [2], [40], [45], simulation predicts 18.6% and 17.4% cell efficiencies for 160 μs and 16 μs , respectively, without any internal light trapping. With 1-pass internal photon reflection, 20% efficiency cell is projected for a bulk lifetime of 160 μs . Enhanced light trapping can be achieved by front surface texturing and incorporating back surface reflectors [46].

5.8 Double-Side Heterojunction Cell

Double-side heterojunction (DHJ) cells on SOM were also fabricated via RPCVD. JV characteristics under AM1.5G illumination from DHJ cells are shown in Fig. 5-17. We obtained a relatively high conversion efficiency of 13.4% ($V_{OC}=645\text{mV}$, $FF=66.2\%$, and $J_{SC}=31.35 \text{ mA/cm}^2$) on sample M-1-1 without incorporating surface texture and front i-layer. More importantly, we found good relationships between the solar cell characteristics and thickness of a-Si:H(p^+). It is seen from the light JV data that sample M-1-2 with 6nm-thick a-Si(p^+) has higher J_{SC} and lower V_{OC} , while sample M-1-1 with 12nm-thick a-Si(p^+) has lower J_{SC} and higher V_{OC} . The V_{OC} data indicates the effectiveness of thickness of a-Si:H (p^+) in passivating the Si surface. J_{SC} decreases with increasing p-layer thickness as the optical transmission through the p-layer decreases exponentially with its thickness [41]. It is evident that there is an optimum a-

Si:H(p⁺) thickness to achieve highest device performance. The FF of these devices is limited by the series resistance associated with screen-printed front contact.

Heterojunction with intrinsic a-Si:H layer (i-layer) can improve the passivation of c-Si interface and improve open-circuit voltage [13], [40]. Hence we fabricated sample M-4-2 with an intrinsic 6.8nm-thick a-Si:H layer followed by 12nm-thick a-Si:H(p⁺) layer in front. The light JV data for samples M-1-1 and M-4-2 indicates that the i-layer improves the surface passivation, as evident from the increase in V_{OC} of about 17mV and nearly unchanged J_{SC}. Slightly lower short-wavelength external quantum efficiency in J_{SC} is due to increased optical losses in the non-optimized intrinsic a-Si:H and a-Si:H(p⁺) layers. Relatively lower FF is due to non-optimized a-Si:H(p⁺) and i-layer thicknesses [14], [47], in addition to series resistance associated with screen-printed front contacts.

Fig. 5-18 shows dark saturation current density, J₀ vs. V_{OC} obtained from the samples (07-B, 41-04-1, M-1-1, M-4-2) with same a-Si:H(p⁺) layer thicknesses. The dark saturation current density was estimated from the following equation:

$$J_0 = J_{SC} \cdot \exp\left(\frac{-qV_{OC}}{k_B T}\right) \quad (5-11).$$

As expected, the J₀ values are in agreement with that measured from Suns-Voc, and there is a strong correlation between J₀ and device structure. In case of n⁺ BSF, by reducing the back contact percentage and incorporating nitride passivation, J₀ reduces by a factor of ~3.5 (samples 07-B and 41-04-1). J₀ in sample M-1-1 decreases by a factor of 4.5 from that of sample 41-04-1 by incorporation of a-Si:H(i)/a-Si:H(n⁺) on the back of the c-Si SOM substrate instead of a heavily doped n⁺ BSF. Incorporation of a-Si:H(i)/a-Si:H(n⁺) layer is quite beneficial in reducing the minority-carrier recombination at the back of c-Si SOM substrate. In sample M-4-2, J₀ decreases by a factor of ~2 from

that of sample M-1-1 by incorporating intrinsic a-Si:H layer at the front, which suggests, in accord with [13], [40], that intrinsic a-Si:H layer improves surface passivation.

Efficiency of the cells fabricated with RPCVD can be improved further by using optimum thicknesses of a-Si:H(p⁺) and i-layer which will lead to increased open-circuit voltage and FF. The distance of the sample from plasma during i-layer deposition can be studied further to reduce plasma damage for achieving better c-Si surface passivation. Moreover, the degradation of FF and J_{SC} in our fabricated cells can be minimized by using optimum front contact and transparent conductive oxide (TCO) to reduce external series resistance and optical losses. The Suns-Voc measurements highlight the projected efficiency of our cells if external series resistance is minimized. Pseudo-FFs of samples 41-04-1, M-1-1 and M-4-2 were measured to be 82.4%, 82.0%, and 76.1%, respectively, as shown in Table 5-1. This Suns-Voc data indicate effectiveness of RPCVD in achieving high-efficiency solar cells. Moreover, internal light trapping by front and back surface texturing and improved back reflection will lead to efficiency comparable to conventional thick-Si high-efficiency heterojunction solar cells.

5.9 Summary

We obtained physical insights into the minority-carrier injection into the c-Si base from the a-Si:H emitter and minority-carrier suppression inside a-Si:H emitter in a silicon heterojunction cell. An R.F. magnetron sputtering system-based process was developed to deposit ITO as a transparent conducting layer. We developed for the first time a low-temperature RPCVD process to form a-Si:H(p⁺)/c-Si heterojunction on thin crystalline-silicon (SOM) foils that are only ~25 microns thick. We studied the dependence of sample-to-plasma distance and deposition temperature on plasma damage and passivation quality of thin crystalline cells. Two device architectures were fabricated with

the RPCVD process. A 13.4% efficiency heterojunction solar cell with the highest V_{OC} of 662mV on these SOM foils without any high-efficiency features such as light trapping was demonstrated. Effect of p-doped a-Si:H thickness and incorporation of intrinsic a-Si:H were studied. This work suggests that RPCVD is a potential technology to deliver lower plasma damage and improved passivation for thin crystalline-Si heterojunction solar cells.

Table 5-1. Overview of HJ device structures and corresponding performances

Sample	i-layer thickness (nm)	p-layer thickness (nm)	Structure	V _{OC} (mV)	J _{SC} (mA/cm ²)	FF (%)	η (%)	ρFF (%)
41-04-1	-	12nm	SHJ	605	29.6	62.8	11.2	82.4
41-05-1	-	6nm	SHJ	524	30.4	63.5	10.1	78.6
M-1-1	-	12nm	DHJ	645	31.4	66.2	13.4	82.0
M-1-2	-	6nm	DHJ	535	32.8	73.9	12.9	80.2
M-4-2	6.8nm	12nm	DHJ	662	31.6	52.6	11.0	76.1

Table 5-2. Measured Suns-Voc from cells fabricated on 500μm c-Si wafers for varying sample positions and temperatures. Smaller position number indicates sample distance closer to the plasma source

Sample	Position	Temp (°C)	Suns-Voc across dies (mV)					Range (mV)	Gas flow rate		
									SiH ₄ (%)	B ₂ H ₆ (%)	Ar (%)
N1-2	3"48	250	571	535	531	508	63	5	50	80	
N1-1	3"32	250	580	558	576	545	35	5	50	80	
N1-3	3"23	250	577	536	614	592	78	5	50	80	
N1-4	3"32	200	585	588	587	579	9	5	50	80	
N2-1	3"23	200	557	572	557	565	15	5	50	80	
N2-2	3"23	225	610	609	611	611	2	5	50	80	
N2-4	3"23	200	629	634	632	631	5	5	100	80	
N2-3	3"16	225	603	615	613	614	12	5	80	80	

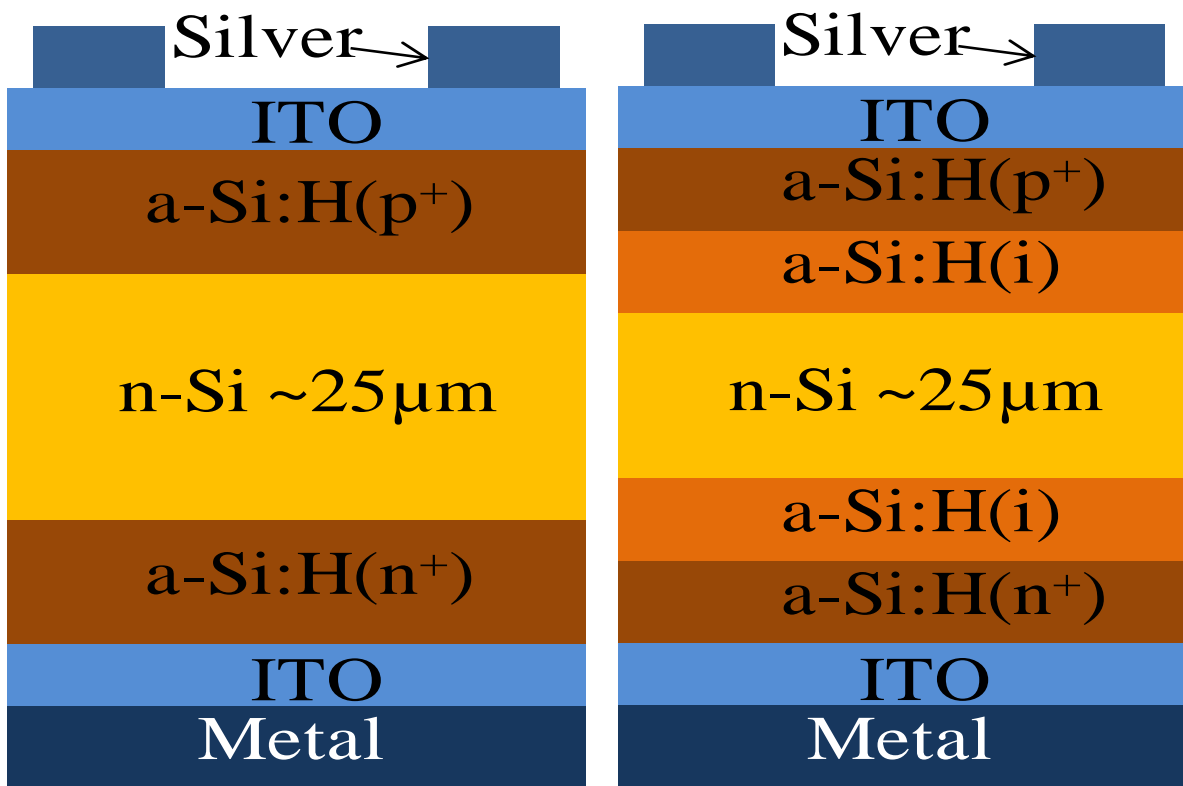


Figure 5-1. Cross-section of a typical double-side heterojunction cell on a n-type crystalline-silicon SOM wafer. The doped a-Si:H layers forms both the emitter and the BSF regions, and improve the surface passivation. The indium tin oxide (ITO) film acts as a transparent conductive layer for the charge carriers, and helps reducing the lateral resistance. The cross-section of the HIT device structure is also shown.

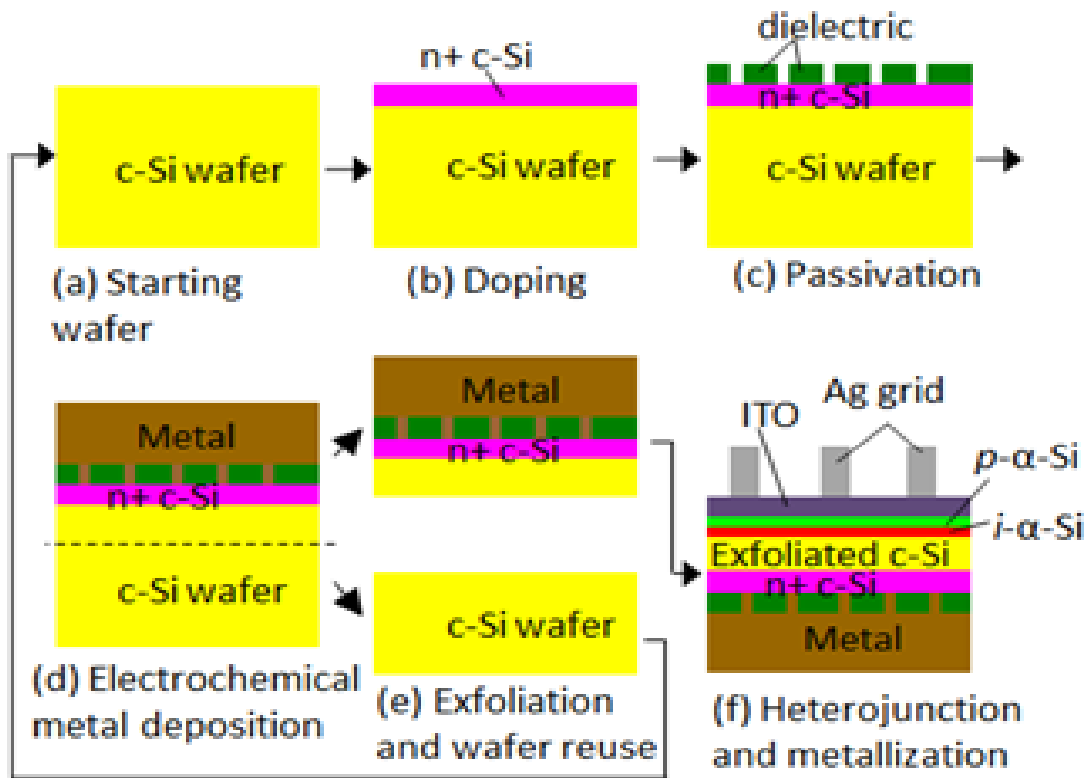


Figure 5-2. Process flow for fabricating exfoliated single heterojunction solar cells.

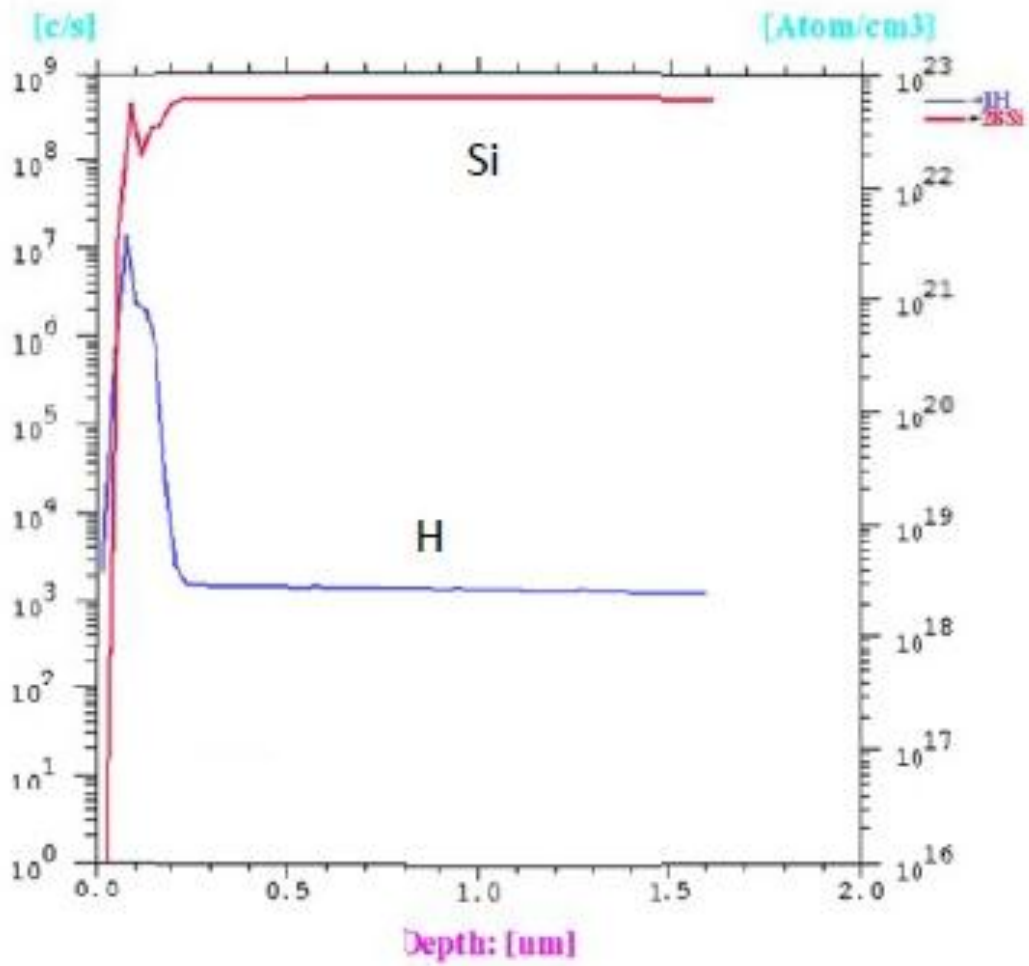


Figure 5-3. SIMS profile showing Hydrogen incorporation into the Si substrate during the electroplating process.

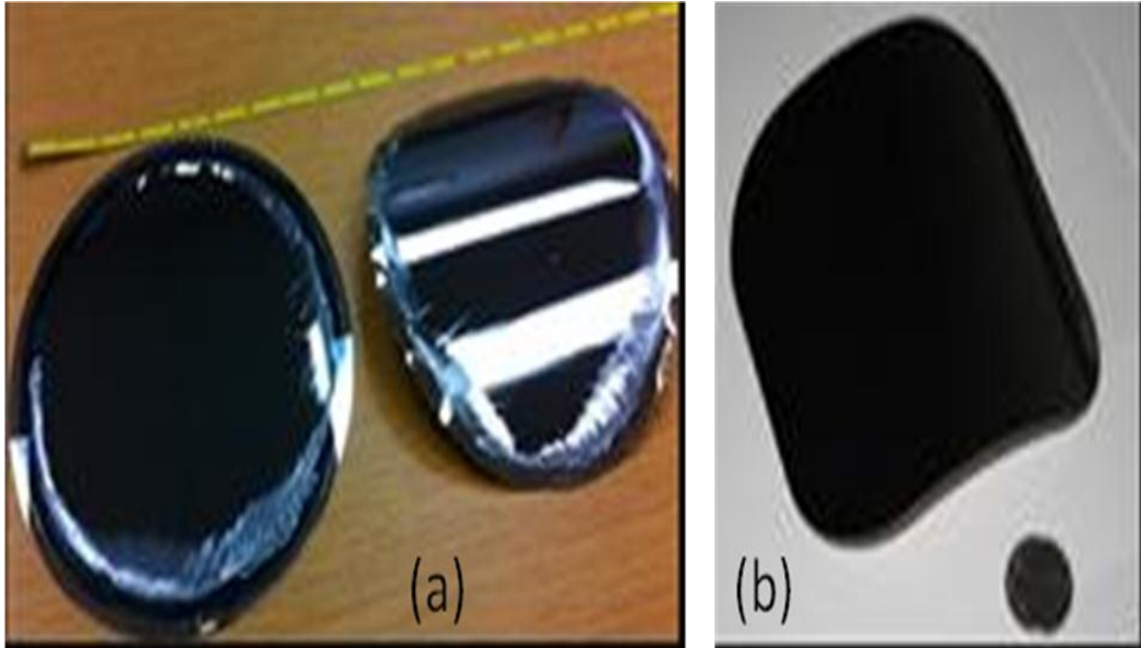


Figure 5-4. Photographs of exfoliated SOM foils. (a) Picture of exfoliation from an 8-inch diameter wafer showing 25 μ m thin Si foil along with the residual wafer after exfoliation, and (b) 125mm x 125mm pseudosquare cut out from the foil. Photo courtesy of Leo Mathew, AstroWatt Inc., and Dabraj Sarkar.

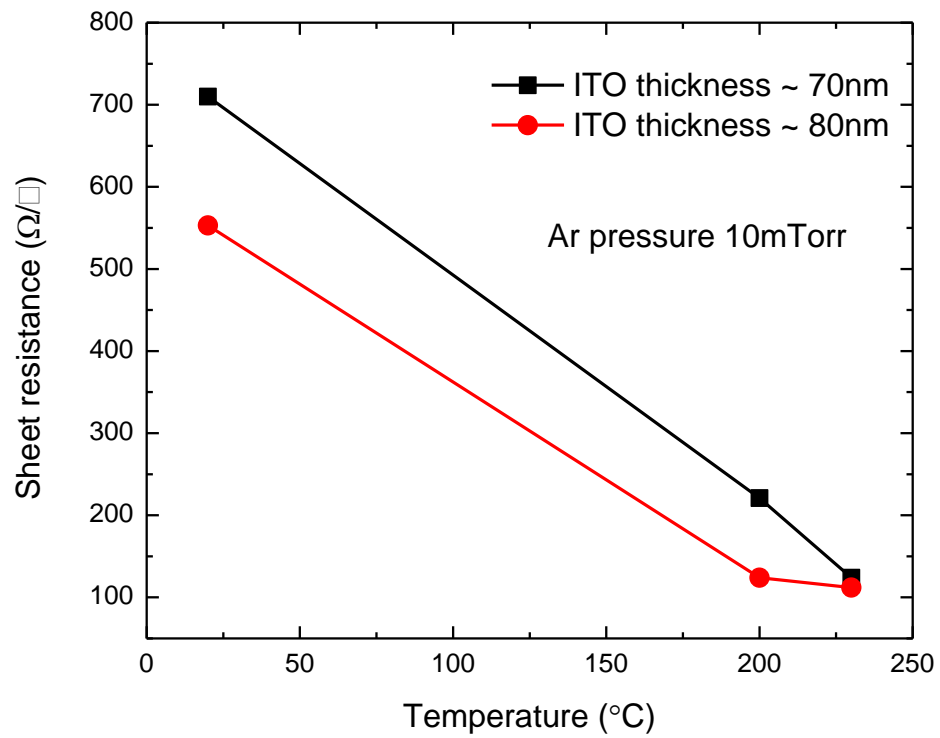


Figure 5-5. Variation of sheet resistance of ITO films as function of substrate temperature. Ar pressure was 10mTorr and two different film thicknesses were analyzed for this experiment.

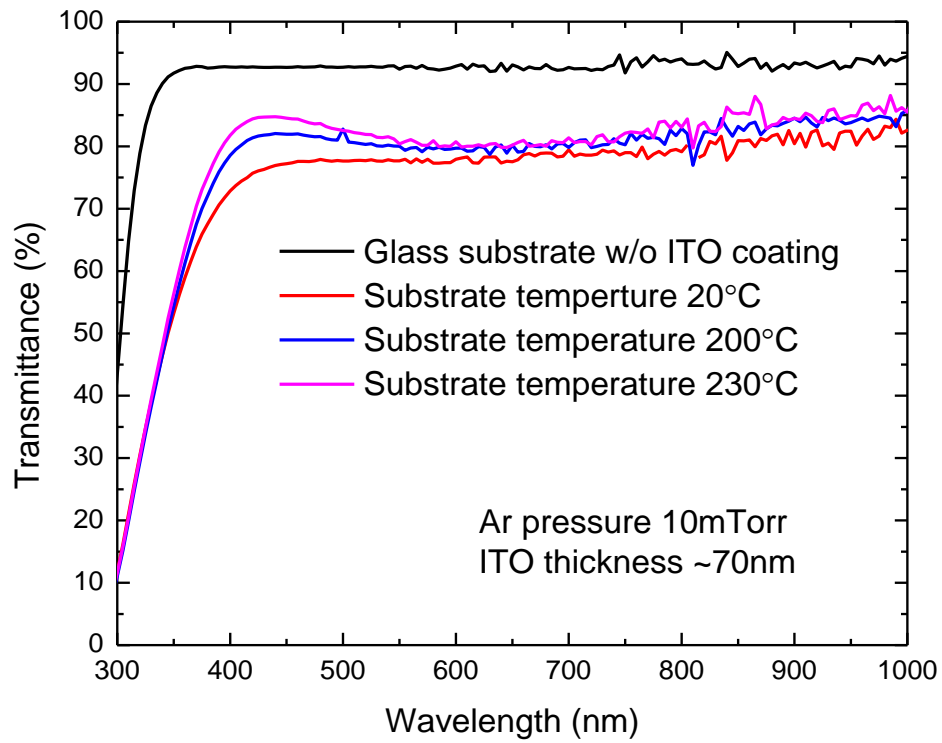


Figure 5-6. Variation of optical transmittance characteristics of ITO films as function of substrate temperature. Film thicknesses were ~ 70nm and the Ar pressure was 10mTorr.

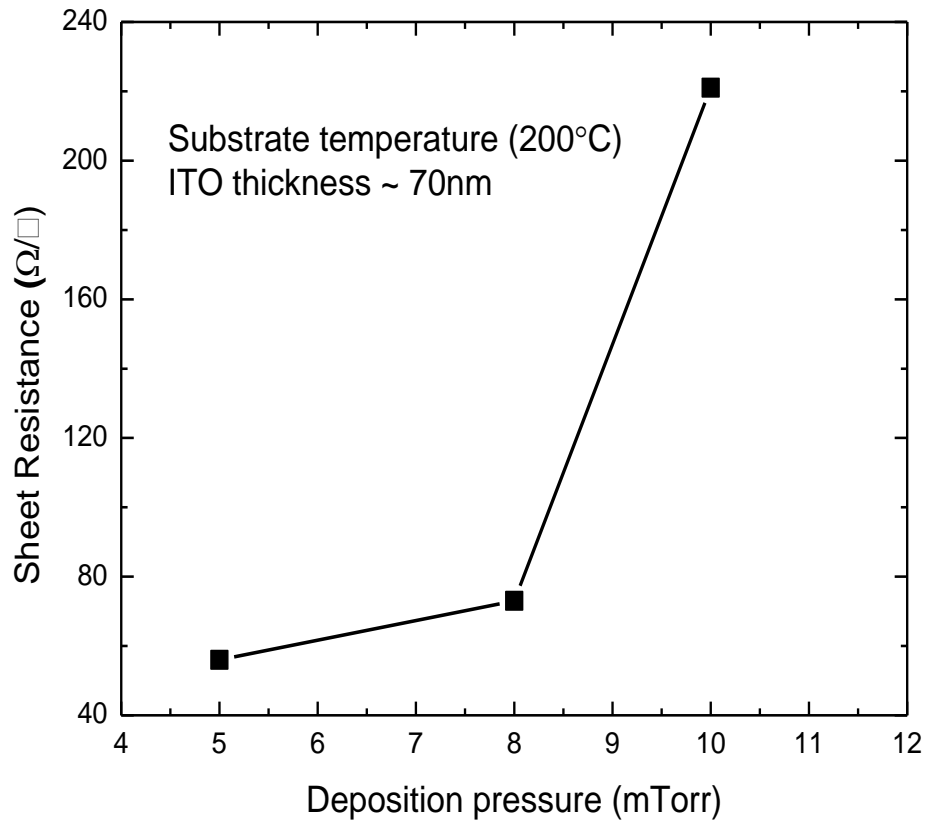


Figure 5-7. Variation of sheet resistance of ITO films as a function of deposition pressure. Substrate temperature was 200°C and film thicknesses were ~70nm.

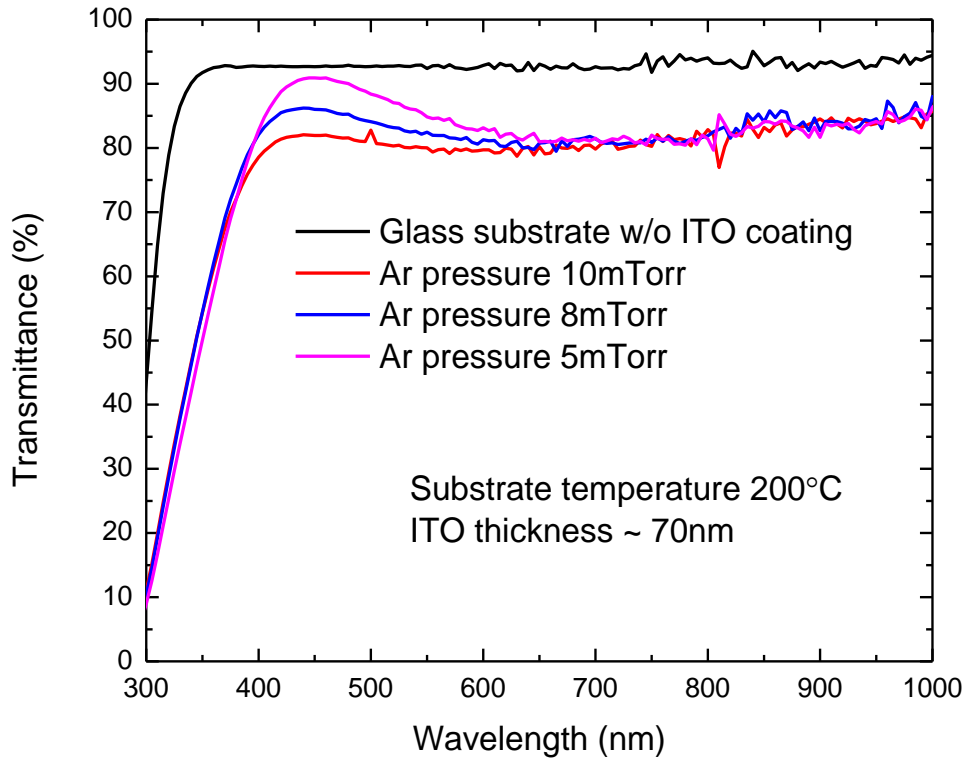


Figure 5-8. Optical transmittance spectra of ITO films as a function of Ar pressure. Substrate temperature was 200°C and film thicknesses were ~70nm.

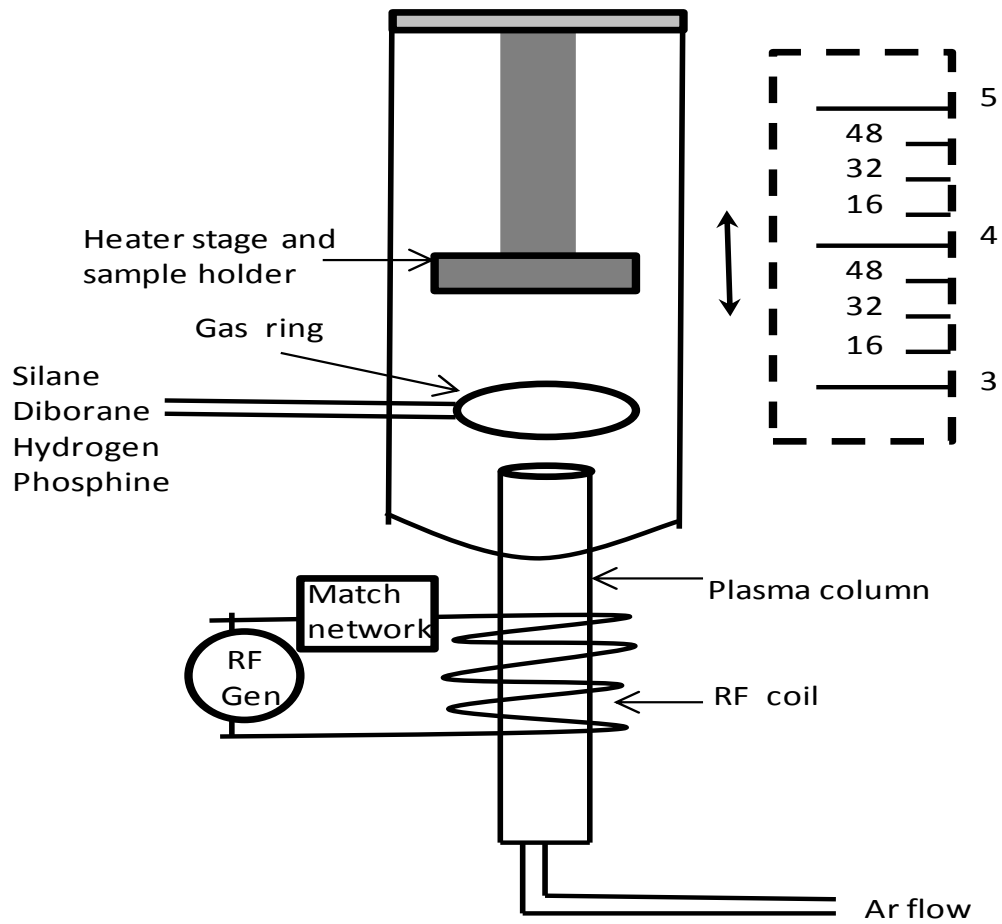


Figure 5-9. Schematic diagram of RPCVD deposition chamber. The key features are that the plasma is remote from the sample, and sample can be placed at different distances downstream from plasma source.

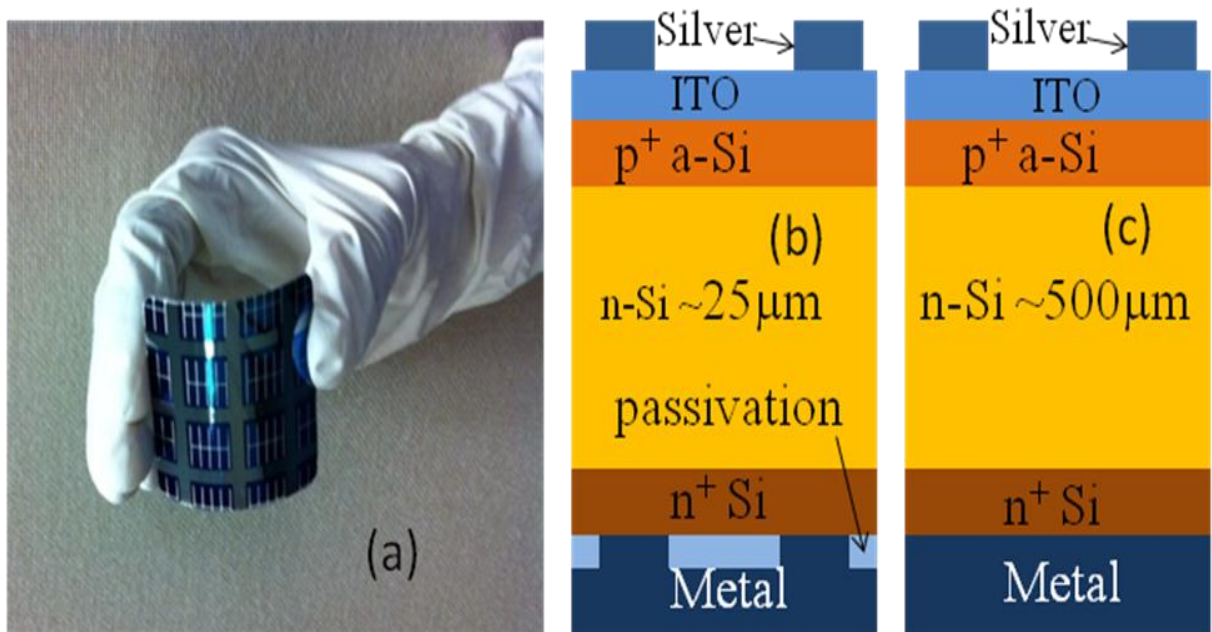


Figure 5-10. Photograph of SOM foil with fabricated HJ cells, and cross-section of fabricated single-side HJ cells. (a) Photograph of the completed 25µm-thick SOM foil with 1.1cm² heterojunction cells, (b) schematic device structure of single-side HJ cell fabricated on 25µm SOM foil without any a-Si(i) layer, and (c) schematic device structure fabricated on 500µm wafer. Photo courtesy of Leo Mathew, AstroWatt Inc., and Dabraj Sarkar.

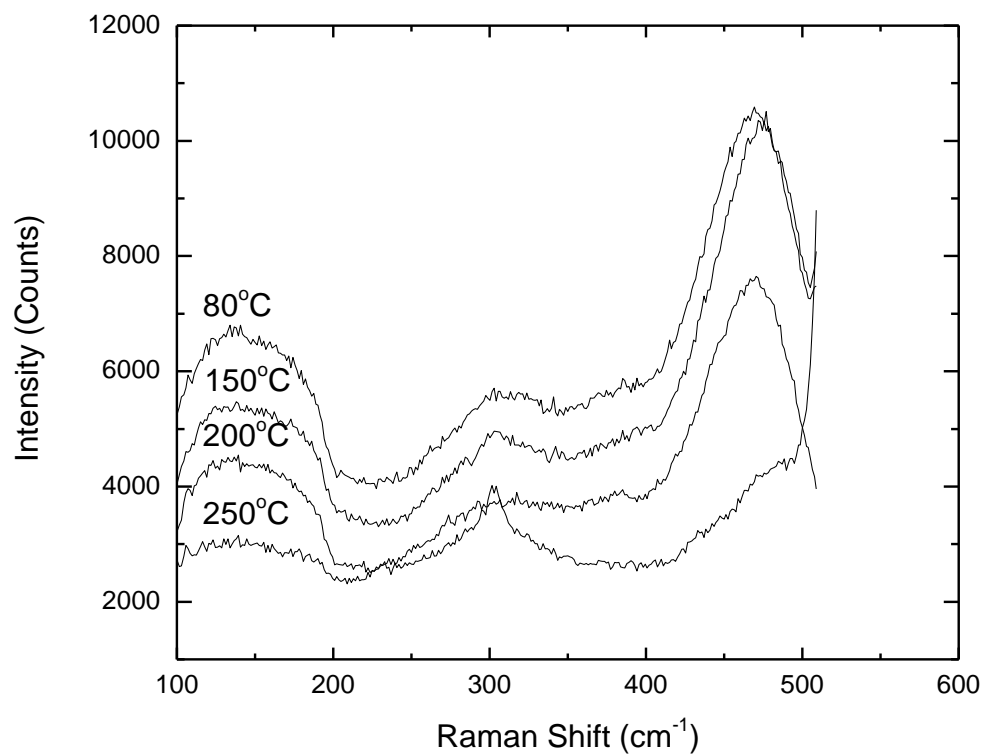


Figure 5-11. Raman spectra of a-Si:H(p⁺) films deposited at different temperatures. Deposition conditions were same as that of sample N2-4 as in Table 5-2.

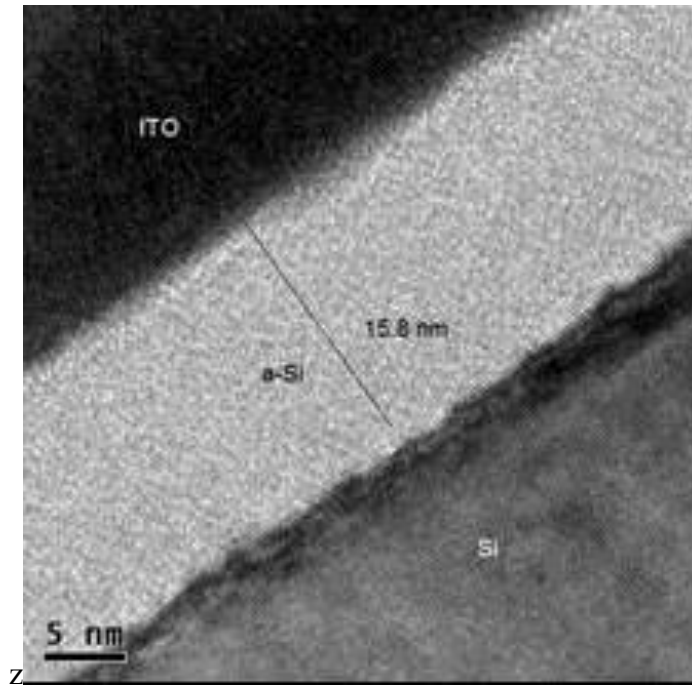


Figure 5-12. High resolution TEM cross-section of thin HJ solar cell on SOM foil. The cross-section clearly shows monocrystalline exfoliated Si with amorphous-Si and ITO layers on top. Photo courtesy of Leo Mathew, AstroWatt Inc., and Dabraaj Sarkar.

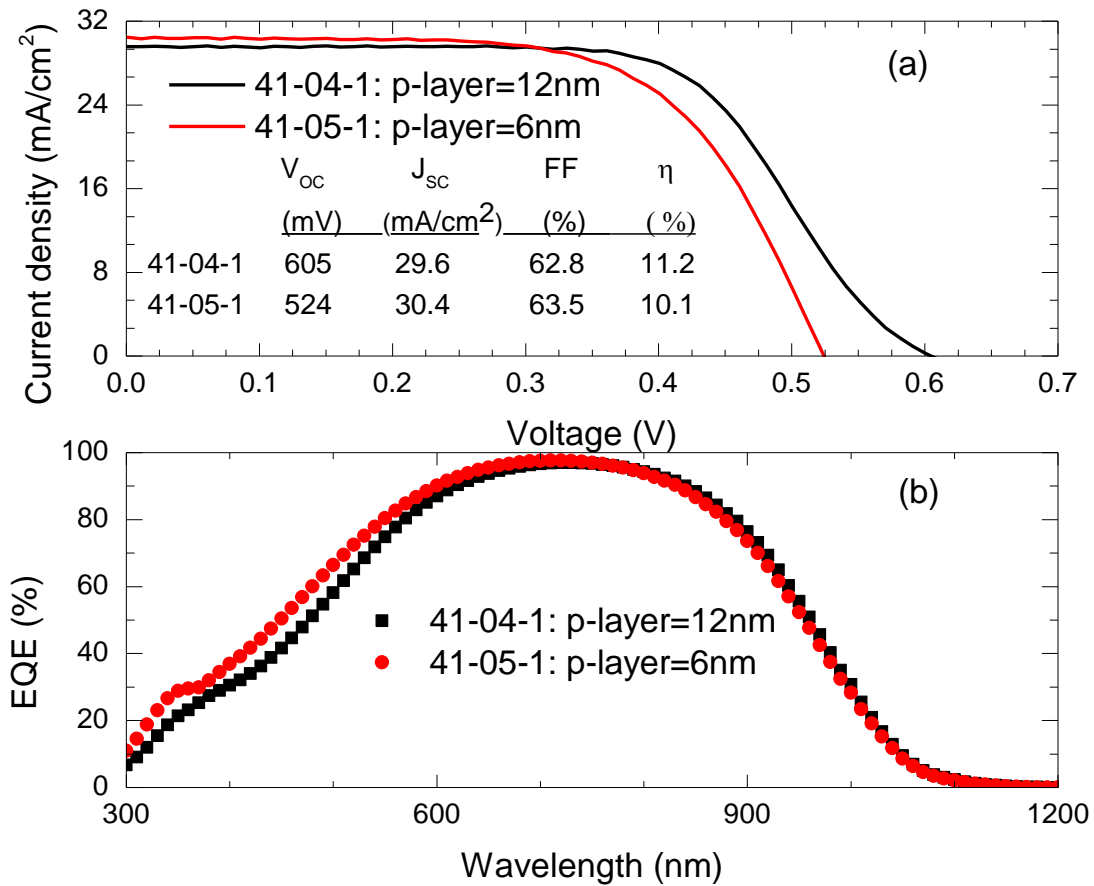


Figure 5-13. Illuminated JV and EQE characteristics of single-side HJ solar cells. (a) AM1.5G illuminated JV characteristics, and (b) EQE data of single-side heterojunction solar cells.

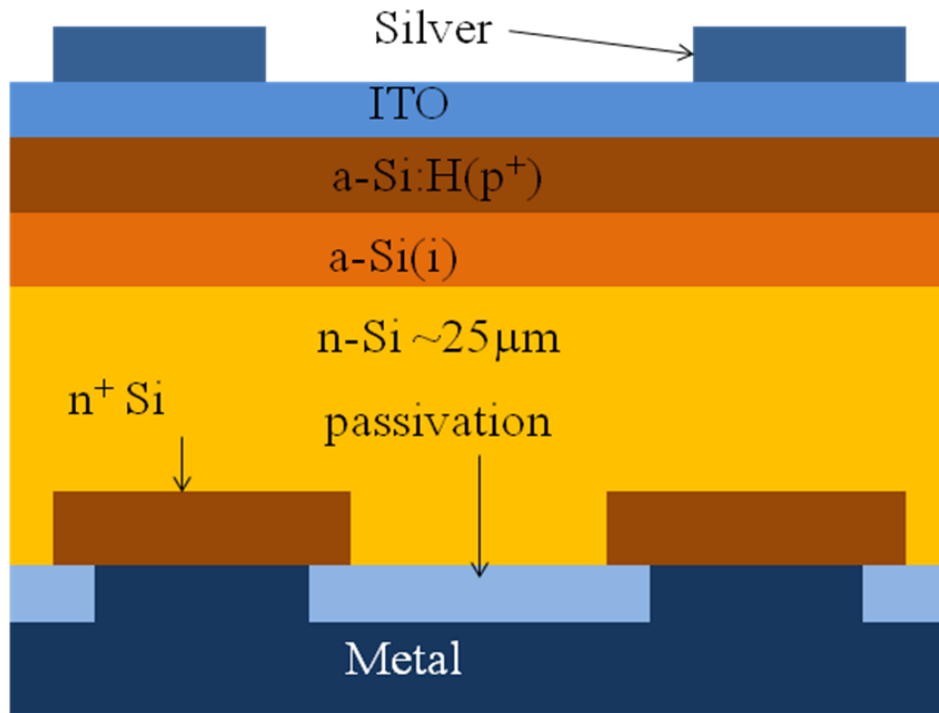


Figure 5-14. Cross-section of the proposed single-side heterojunction (SHJ) cell on a n-type SOM wafer. The back side has local BSF and local contact to reduce recombination losses (similar to PERL cell). Local BSF and local contact designs are described in Chapter 3.

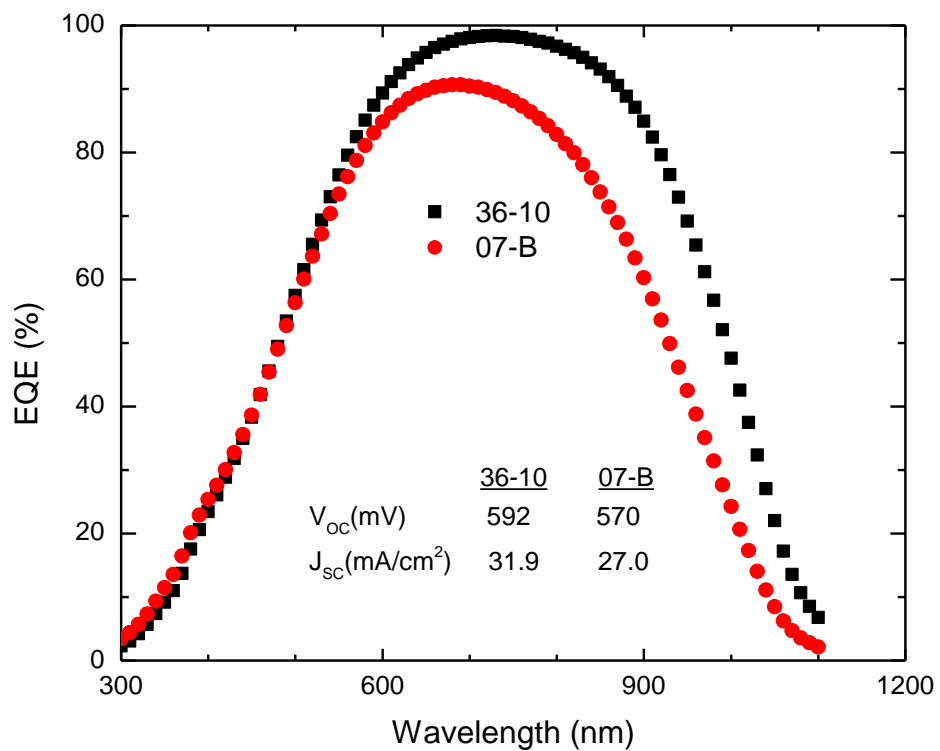


Figure 5-15. EQE data indicating carrier recombination at the back due to uniform metal contacts and no surface passivation.

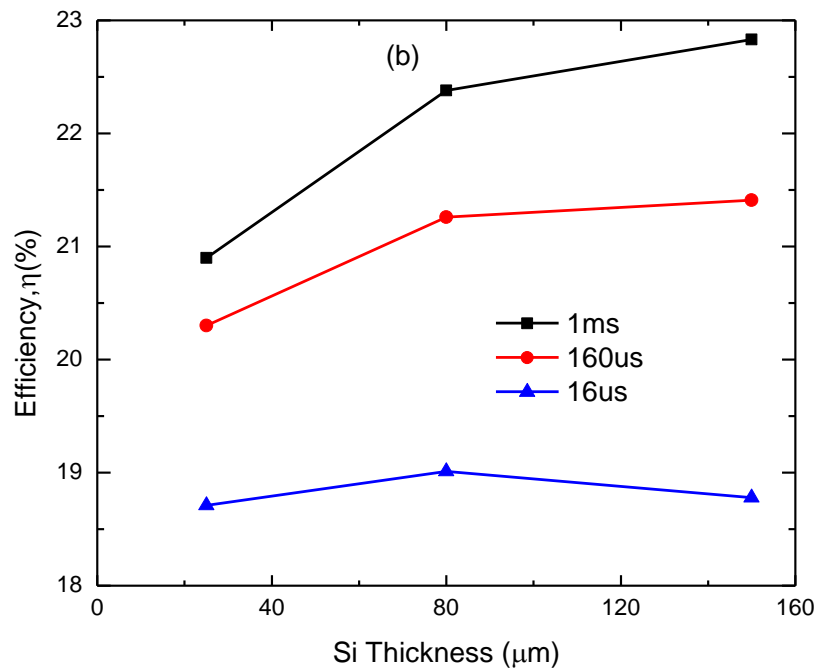
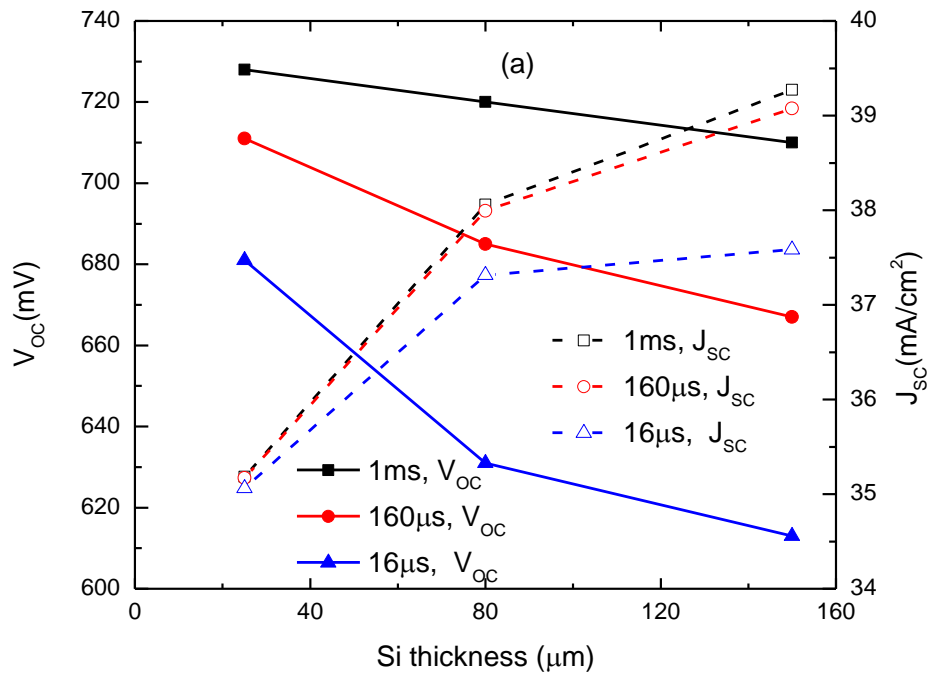


Figure 5-16. FLOODS-predicted dependence of intrinsic V_{OC} , J_{SC} , and η versus silicon thickness for varying bulk lifetime. $S_f=S_b=10\text{cm/s}$ and zero internal reflection.

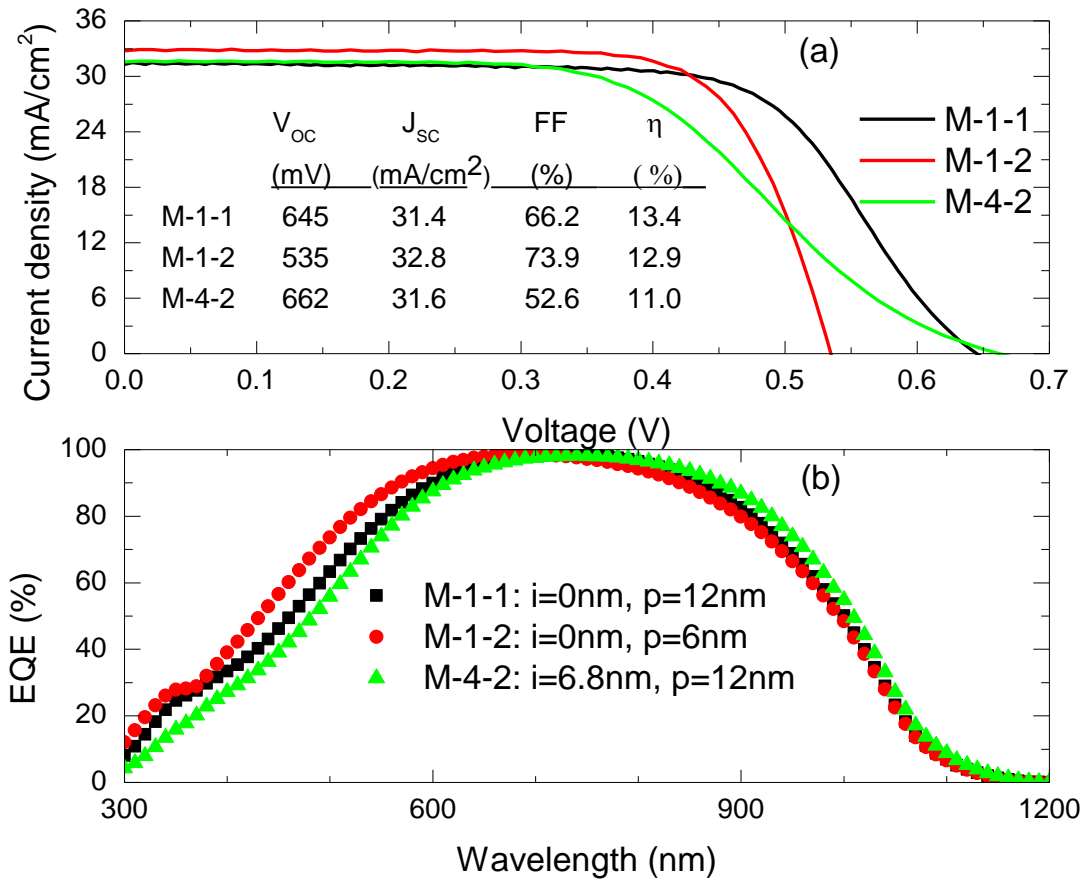


Figure 5-17. Illuminated JV and EQE characteristics of double-side HJ solar cells. (a) The AM1.5G illuminated JV characteristics, and (b) EQE data of double-side heterojunction solar cells.

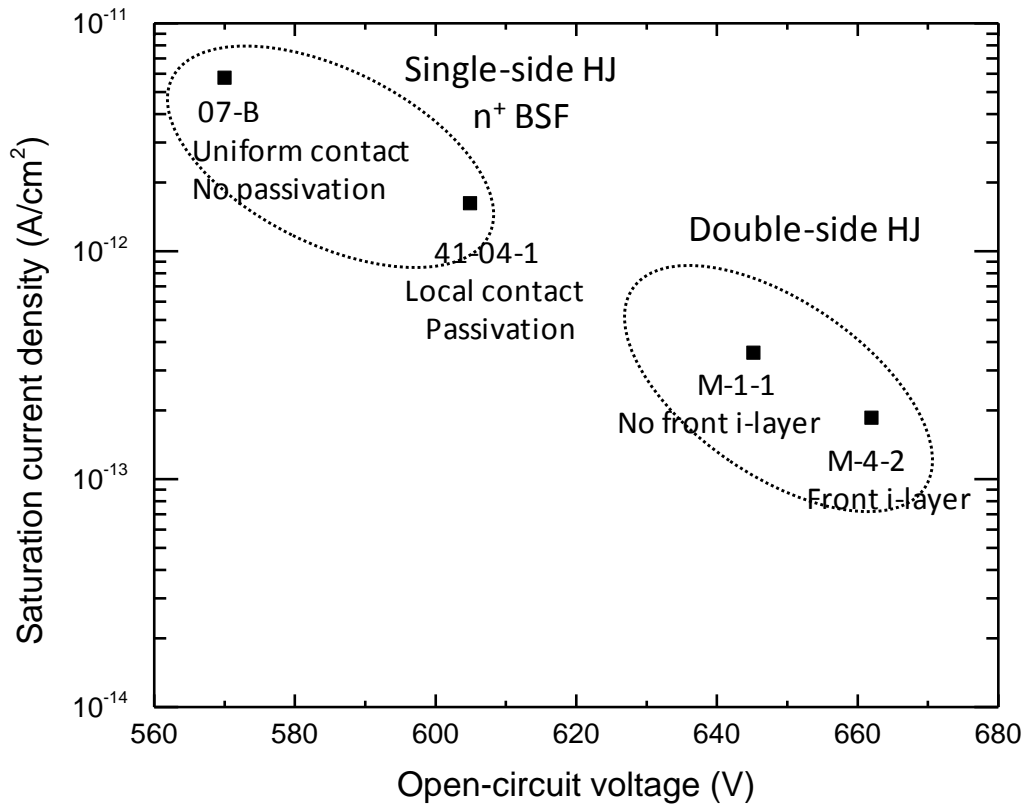


Figure 5-18. Comparison of dark saturation current densities vs. open circuit voltages for different cell structures.

CHAPTER 6 SUMMARY AND FUTURE WORK

6.1 Summary

The main goal of this work was to design and fabricate high-efficiency solar cells on exfoliated thin crystalline-Si substrates that are about $\sim 25\mu\text{m}$ thick. In order to do this, we needed to gain physical insights and identify key loss mechanisms in a thin crystalline Si solar cell by device simulation. We upgraded FLOODS for photovoltaic device simulation with necessary physical models. Exfoliated semiconductor-on-metal (SOM) substrates were produced at AstroWatt Inc., and solar cells were fabricated on these substrates at the Microelectronic Research Center at the University of Texas at Austin.

The crystalline-Si photovoltaic industry has been scaling down the Si wafer thickness in order to reduce costs and potentially attain higher efficiencies by minimizing bulk recombination. As the silicon thickness decreases, the surface passivation quality and recombination in the back-surface field region and at contacts dictate the performance of these cells. With FLOODS, we were able to comprehensively study the effect of surface recombination velocity, minority-carrier lifetime in the bulk, doping profile of back-surface field region, and contact coverage on the performance of the solar cell in the sub- $40\mu\text{m}$ thickness. We used physics-based FLOODS simulations to understand and propose efficient device structures for back-contact and heterojunction solar cells.

Thin crystalline silicon-based heterojunction solar cells require excellent passivation on the front and back side of the cell. Plasma-enhanced chemical vapor deposition (PECVD) and hot-wire chemical vapor deposition (HWCVD) are typically

used to fabricate a-Si:H/c-Si-based heterojunction solar cells. In this work, we developed remote-plasma chemical vapor deposition (RPCVD) as an alternative promising low-temperature ($\sim 200^\circ\text{C}$) technology for a-Si:H film deposition with lower plasma damage than conventional PECVD. RPCVD was shown to be a potential technology to achieve low effective surface recombination velocity (SRV). Two device architectures were fabricated on $25\ \mu\text{m}$ c-Si SOM foils: 1) a single-side heterojunction (SHJ) cell, and 2) a double-side heterojunction (DHJ) cell. An efficiency of 13.4% with highest open-circuit voltage of 662mV was measured on a device.

Based on our experimental work, it is evident that there are two ways to achieve high-efficiency thin-Si solar cells: 1) single-side HJ cells with local back junction and local back contacts, and 2) double-side HJ cells. The proposed device architectures will have front and back texture for enhanced light-trapping. Low SRV is possible with our RPCVD process as evident from very high open-circuit voltage obtained from the fabricated cells. High efficiency HJ solar cells are achievable with thin crystalline-Si substrates that are comparable to conventional thicker HJ solar cells.

6.2 Future Work

Future work should include expansion of FLOODS to include carrier-transport models across the a-Si:H/c-Si heterojunction. On the experimental side, characterization of the passivation quality of RPCVD deposited a-Si:H layers should be done by measuring effective surface recombination velocity. Quantum efficiency and hence short-circuit current density should be improved by incorporating light-trapping schemes such as surface texturing and back-surface reflectors.

6.2.1 Carrier Transport Model across HJ

The critical transport mechanism is believed to be tunneling across the heterojunction interface, which depends on the band alignment and band offset [14]. Minority-carrier lifetime is extremely short in the a-Si/c-Si heterojunction, but the injected minority-carrier concentration is suppressed significantly inside the heterojunction as shown in Sec. 5.2. The photon-absorption profile and hence the optical carrier generation rate $g(x)$ are modified in the heterojunction due to wider bandgap and different absorption coefficients of a-Si. Moreover, the transparent conductive oxide (typically Indium Tin Oxide or ITO) is a degenerately doped n-type semiconductor with bandgap of 3.7eV, and can be treated as a metallic contact or as a part of the hetero-interface [14], [47]. We propose to develop reliable engineering-based models for the carrier transport mechanism and optical absorption across the heterojunction, and implement the models in FLOODS.

6.2.2 Surface Recombination Velocity Characterization

Very high open-circuit voltage (>662mV) measured from fabricated HJ cells suggests RPCVD is a potential technology to achieve improved surface passivation by reducing the plasma related damage to the crystalline-silicon surface. We intend to characterize surface recombination velocity at the a-Si:H/c-Si interface by the quasi-steady-state photoconductivity (QSSPC) method [48]:

$$\frac{1}{\tau_{eff}(\nabla n)} = \frac{1}{\tau_{bulk}(\nabla n)} + \frac{2 \cdot S_{eff}(\nabla n)}{t_{Si}} \quad (6-1)$$

where T_{eff} is measured lifetime, T_{bulk} is bulk lifetime, and S_{eff} is measured effective surface recombination velocity.

6.2.3 Light Trapping by Surface Texturing

We intend to improve short-circuit current density by introducing surface texturing. We have optimized our RPCVD process for polished SOM foils. Our future work will include optimization of RPCVD process for textured surfaces. We have already developed a KOH based texturing process for our SOM foils.

LIST OF REFERENCES

- [1] S. Bowden, "From the valley of death to the golden decade: crystalline silicon solar cells from 10 μm to 100 μm ," *Proc. 19th Workshop Cryst. Si. Solar Cells and Modules*, Vail, CO, pp. 192-195, Aug. 2009.
- [2] R. M. Swanson, "Developments in silicon solar cells", *Proc. IEEE Electron Devices Meeting*, pp. 359-362, Dec. 2007.
- [3] L. Mathew, and D. Jawarani, "Method of forming an electronic device using a separation-enhancing species", *U.S. Patent 7749884*, Jul. 6, 2010.
- [4] R. M. Swanson, "Approaching the 29% limit efficiency of silicon solar cells," *Proc. 31st IEEE Photovoltaic Spec. Conf.*, pp. 889-894, Jan. 2005.
- [5] W. Shockley, and H. J. Queisser, "Detailed balance limit of efficiency of p-n junction solar cells," *J. Appl. Phys.*, vol. 32, pp. 510 - 519, Mar. 1961.
- [6] Sanyo Electric Co., Ltd., *News Release*, May 22, 2009.
- [7] P. J. Cousins, D. D. Smith, L. Hsin-Chiao, J. Manning, T. D. Dennis, A. Waldhauer, K. E. Wilson, G. Harley, and W. P. Mulligan, "Generation 3: improved performance at lower cost," *Proc. 35th IEEE Photovoltaic Spec. Conf.*, Honolulu, HI, pp. 275-278, Jun. 2010.
- [8] M. E. Law, and S. Cea, "Continuum-based modeling of silicon integrated circuit processing:an object-oriented approach," *Computational Materials Science*, vol. 12, pp. 289-308, Nov. 1998.
- [9] M. Stocks, A. Blakers, and A. Cuevas, "Multicrystalline silicon solar cells with low rear surface recombination," *Proc. 26th IEEE Photovoltaic Spec. Conf.*, Anaheim, CA pp. 67-70, Sep. 1997.
- [10] A. Wang, J. Zhao, and M. A. Green, "24% efficient silicon solar cells," *Appl. Phys. Lett.*, vol. 57, pp. 602-604, Aug. 1990.
- [11] M. D. Lammert, and R. J. Schwartz, "The interdigitated back contact solar cell: A silicon solar cell for use in concentrated sunlight," *IEEE Trans. Electron Devices*, vol. 24, pp. 337-342, Apr. 1977.
- [12] R. A. Sinton, and R. M. Swanson, "Simplified backside-contact solar cells," *IEEE Trans. Electron Devices*, vol. 37, pp. 348-352, Feb. 1990.
- [13] H. Sakata, Y. Tsunomura, H. Inoue, S. Taira, T. Baba, H. Kanno, T. Kinoshita, M. Taguchi, and E. Maruyama, "R&D progress of next-generation very thin HITTM solar cells," *Proc. 25th EUPVSEC*, Valencia, Spain, pp. 1102-1105, Sep. 2010.

- [14] A. Kanevce, and W. K. Metzger, "The role of amorphous silicon and tunneling in heterojunction with intrinsic thin layer (HIT) solar cells," *J. Appl. Phys.*, vol. 105, 094507-1-094507-7, May 2009.
- [15] R. A. Rao, L. Mathew, S. Saha, S. Smith, D. Sarkar, R. Garcia, R. Stout, A. Gurmu, D. Ahn, D. Xu, D. Jawarani, E. Onyegam, M. Hilali, S. Banerjee, and J. Fossum, "A novel low cost 25 μ m thin exfoliated monocrystalline si solar cell technology," *Proc. 26th EUPVSEC*, Hamburg, Germany, pp. 2439-2442, Sep. 2011.
- [16] J. G. Fossum, and M. A. Shibib, "An analytic model for minority-carrier transport in heavily doped regions of silicon devices," *IEEE Trans. Electron Devices*, vol. 28, pp. 1018-1025, Sep. 1981.
- [17] A. Cuevas, P. A. Basore, G. Giroult-Maltakowski, and C. Dubois, "Surface recombination velocity of highly doped n-type silicon," *J. Appl. Phys.*, vol. 80, pp. 3370-3375, May 1996.
- [18] S. M. Sze, and K. K. Ng, "Physics of semiconductor devices," *3rd Edition, John Wiley & Sons*, Hoboken, New Jersey, 2007.
- [19] J. G. Fossum, "Computer-aided numerical analysis of silicon solar cells," *Solid-State Electronics*, vol. 19, pp. 269-277, Apr. 1976.
- [20] J. G. Fossum, R.P. Mertens, D.S. Lee, and J.F. Nijs, "Carrier recombination and lifetime in highly doped silicon," *Solid-State Electronics*, vol. 26, pp. 569-576, Jun. 1983.
- [21] D. B. M Klaassen, "A unified mobility model for device simulation," *IEDM Tech. Dig.*, pp. 357-360, Dec. 1990.
- [22] G. Masetti, M. Severi, and S. Solmi, "Modeling of carrier mobility against carrier concentration in arsenic-, phosphorus-, and boron-doped silicon," *IEEE Trans. Electron Devices*, vol. 30, pp. 764-769, Jul. 1983.
- [23] M. P. Thekaekara, "Data on incident solar energy," *Suppl. Proc. 20th Annu. Meet. Inst. Environ. Sci.*, p. 21, Jan. 1974.
- [24] M. A. Green, "The path to 25% silicon solar cell efficiency: history of silicon cell evolution," *Prog. Photovoltaics: Res. Appl.*, vol. 17, pp. 183-189, May 2009.
- [25] J. G. Fossum, "Physical operation of back-surface-field silicon solar cells," *IEEE Trans. Electron Devices*, vol. 24, Apr. 1977.
- [26] M. Sheoran, A. Upadhyayaa, and A. Rohatgi, "Bulk lifetime and efficiency enhancement due to gettering and hydrogenation of defects during cast multicrystalline silicon solar cell fabrication," *Solid-State Electronics*, vol. 52, pp. 612-617, May 2008.

- [27] N. Stem, C.A.S. Ramos, and M. Cid, "Open-circuit voltages: theoretical and experimental optimizations of rear passivated silicon solar cells using FZ and CZ wafers," *Solid-State Electronics*, vol 54, pp. 221-225, Mar. 2010.
- [28] D. Kray, and K. R. McIntosh, "Analysis of selective phosphorous laser doping in high-efficiency solar cells," *IEEE Trans. Electron Devices*, vol. 56, pp. 1645 – 1650, Aug. 2009.
- [29] A. Das, V. Meemongkolkiat, D. Kim, S. Ramanathan, and A. Rohatgi, "20% efficient screen-printed cells with spin-on-dielectric-passivated boron back-surface field," *IEEE Trans. Electron Devices*, vol. 57, pp. 2462 - 2469 Jul. 2010.
- [30] W. P. Mulligan, D. H. Rose, M. J. Cudzinovic, D. M. De Ceuster, K. R. McIntosh, D. D. Smith, and R. M. Swanson, "Manufacture of solar cells with 21% efficiency," *Proc. 19th EUPVSEC*, Paris, France, pp. 387-390, 2004.
- [31] M. Schaper, J. Schmidt, H. Plagwitz, and R. Brendel, "20.1%-efficient crystalline silicon solar cell with amorphous silicon rear-surface passivation," *Prog. Photovoltaics: Res. Appl.*, vol. 13, pp. 381-386, Aug. 2005.
- [32] M. Lu, S. Bowden, U. Das, and R. Birkmire, "a-Si/c-Si heterojunction for interdigitated back contact solar cell," *Proc. 22nd EUPVSEC*, Milan, Italy, pp. 924-928, 2007.
- [33] V. G. Weizer, H. W. Brandhorst, J.D. Broder, R. E. Hart, and J. H. Lamneck, "Photon-degradation effects in terrestrial silicon solar cells," *J. Appl. Phys.*, vol. 50, pp. 4443-4449, Jun. 1979.
- [34] J. G. Fossum, and D. S. Lee, "A physical model for the dependence of carrier lifetime on doping density in nondegenerate silicon," *Solid-State Electron.*, vol. 25, pp. 741-747, Aug. 1982.
- [35] J. G. Fossum, and E. L. Burgess, "High-efficiency p⁺nn⁺ back-surface-field silicon solar cells," *Appl. Phys. Lett.*, vol. 33, pp. 238-240, May 1978.
- [36] Y. Taur, and T. H. Ning, "Fundamentals of modern VLSI devices," *Cambridge, U.K.: Cambridge Univ. Press*, 1998.
- [37] T. Mishima, M. Taguchi, H. Sakata, and E. Maruyama, "Development status of high-efficiency HIT solar cells", *Solar Energy Mater. & Solar Cells*, vol. 95, pp. 18-21, Jan. 2011.
- [38] B. Anthony, T. Hsu, L. Breaux, R. Qian, S. Banerjee, and A. Tasch, "Remote plasma-enhanced CVD of silicon: reaction kinetics as a function of growth parameters", *J. Electronic Materials*, vol. 19, pp. 1089-1094, May 1990.

- [39] T. Swada, N. Terada, S. Tsuge, T. Baba, T. Takahama, K. Wakisaka, S. Tsuda, and S. Nakano, "High-efficiency a-Si/c-Si heterojunction solar cell", *Proc. 24th IEEE Photovoltaic Spec. Conf.*, Waikoloa, HI, pp. 1219-1226, Dec. 1994.
- [40] M. Taguchi, A. Terakawa, E. Maruyama, and M. Tanaka, "Obtaining a higher Voc in HIT cells", *Prog. Photovoltaics: Res. Appl.*, vol. 13, pp. 481-488, Sep. 2005.
- [41] Z. C. Holman, A. Descoedres, L. Barraud, F. Z. Fernandez, J. P. Seif, D. Wolf, and C. Ballif, "Current losses at the front of silicon heterojunction solar cells", *IEEE J. Photovoltaics*, vol. 2, pp. 7-15, Jan. 2012.
- [42] J. G. Fossum, D. Sarkar, L. Mathew, R. Rao, D. Jawarani, and M. E. Law, "Back-contact solar cells in thin crystalline silicon," *Proc. 35th IEEE Photovoltaic Spec. Conf.*, Honolulu, HI, pp. 3131-3136, Jun. 2010.
- [43] J. Zhao, A. Wang, M. A. Green, and F. Ferrazza, "19.8% Efficient "Honeycomb" Textured Multicrystalline and 24.2% Monocrystalline Silicon Solar Cells", *Appl. Phys. Lett.*, vol. 73, pp. 1991-1993, Jul. 1998.
- [44] J. Zhao, A. Wang, P. P. Altermatt, S. R. Wenham, and M. A. Green, "24% efficient PERL silicon solar cell: recent improvements in high efficiency silicon cell research", *Solar Energy Mater. Solar Cells*, vol. 41-42, pp. 87-99, Jun. 1996.
- [45] A Cuevas, and D. A. Russell, "Co-optimisation of the emitter region and the metal grid of silicon solar cells", *Prog. Photovoltaics: Res. Appl.*, vol. 8, pp. 603-616, Nov. 2000.
- [46] R. Brendel, R. B. Bergmann, P. Lölgen, M. Wolf, and J. H. Werner, "Ultrathin crystalline silicon solar cells on glass substrates", *Appl. Phys. Lett.*, vol. 70, pp. 390-392, Jan. 1997.
- [47] U. Das, S. Hegedus, L. Zhang, J. Appel, J. Rand, and R. Birkmire, "Investigation of hetero-interface and junction properties in silicon heterojunction solar cells", *Proc. 35th IEEE Photovoltaic Spec. Conf.*, Honolulu, HI, pp. 1358-1362, Jun. 2010.
- [48] F. M. Schuurmans, A. Schonecker, A. R. Burgers, and W. C. Sinke, "Simplified evaluation method for light-biased effective lifetime measurements", *Appl. Phys. Lett.*, vol. 71, pp. 1795-1797, Sep. 1997.
- [49] S. Ray, R. Banerjee, N. Basu, A. K. Batabyal, and A. K. Barua, "Properties of tin doped indium oxide thin films prepared by magnetron sputtering", *J. Appl. Phys.*, vol. 54, pp. 3497-3501, Jun. 1983.
- [50] O. Tuna, Y. Selamet, G. Aygun, and L. Ozyuzer, "High quality ITO thin films grown by DC and RF sputtering without oxygen", *J. Phys. D: Appl. Phys.*, vol. 43, pp. 55402-55409, Jan. 2010.

- [51] L. Meng , and M. P. dos Santos, "Properties of indium tin oxide (ITO) films prepared by r.f. reactive magnetron sputtering at different pressures", Thin Solid Films, vol. 303, pp. 151-155, Jan. 1997.

BIOGRAPHICAL SKETCH

Dabraaj Sarkar received his B.Sc. in electrical and electronic engineering from Bangladesh University Engineering and Technology in 2003. After his baccalaureate, he worked as an engineer trainee at GE Healthcare and then as an engineer at GrameenPhone Ltd. He is currently doing his Ph.D. under Prof. Jerry G. Fossum in electrical engineering at the University of Florida. He collaborated with AstroWatt Inc. and Prof. Sanjay Banerjee in Austin, TX from June 2010–June 2012 where he developed a-Si:H/c-Si heterojunction process and indium tin oxide(ITO) based transparent conducting oxide(TCO) process for its silicon heterojunction solar cell process line. His research interests include device modeling, simulation, remote plasma CVD, fabrication and characterization of thin a-Si:H/c-Si heterojunction and back-contact solar cells.